Magnitude of the Radiative Effects of the Saharan Dust Layer

By
P. Minnis and S.K. Cox

Department of Atmospheric Science
Colorado State University
Fort Collins, Colorado

Colorado State University

Department of Atmospheric Science

Paper No. 283

MAGNITUDE OF THE RADIATIVE EFFECTS OF THE SAHARAN DUST LAYER

by

Patrick Minnis

and

Stephen K. Cox

Research Report supported by
The Global Atmospheric Research Program
National Science Foundation and the
GATE Project Office, NOAA under grants
OCD 74-21678 and ATM 77-15369.

Department of Atmospheric Science
Colorado State University
Fort Collins, Colorado
80523.

January 1978.

Atmospheric Science Paper No. 283

ABSTRACT

MAGNITUDE OF THE RADIATIVE EFFECTS OF THE SAHARAN DUST LAYER

The shortwave and longwave properties of the Saharan dust layer are studied using broadband hemispheric irradiance data and numerical radiative transfer routines. The analysed data were collected during the GARP Alantic Tropical Experiment (GATE) in the summer of 1974. The solar heating rates, fractional absorptions and reflectivities, as well as the longwave effective emissivities and cooling rates for the 550 - 950 mb layer are determined for both clear and dusty days. These parameters are compared to corresponding parameters derived with the aid of two broadband radiative transfer routines which utilize the observed temperature and moisture data. The magnitude of the dust effects are determined by differencing the measured and computed results.

It is found that the Saharan dust increases the atmospheric reflectivity in the area on the average by nearly 50% over the clear sky values. The increase in absorption, though only 9% for the average of six days may approach 20% of the total absorption for a clear atmosphere. The energy reflected by the dust is approximately twice the amount absorbed. Total extinction increases of up to 20% or 61 Wm^{-2} are found in the presence of dust. Observed heating rates are consistently higher in the dust layer than is calculated but by no more than 0.1°C hr^{-1}.

The infrared effects of the dust appear to be much less significant than the effects on the solar spectrum. Changes in effective emissivities in the presence of dust are ambiguous and rarely exceed the

uncertainties of the observations. Cooling rate comparisons reveal the same type of inconsistencies.

ACKNOWLEDGEMENTS

We would like to express our appreciation to Dr. Bruce Albrecht and Mr. David O'C. Starr for their helpful suggestions. Special thanks are due to Ms. M. Charline Polifka and Mr. Stephen Knox for their expert programming assistance and Ms. Sandy Wunch, Ms Janella Owen-Ashbaugh, and Ms. Pauline Martin for their assistance in the preparation of this report.

This research has been supported by the Global Atmospheric Research program, the National Science Foundation, and the GATE Project Office, NOAA, under Grants OCD 74-21678 and ATM 77-15369. Acknowledgement is also made to the flight facility and the computing facility of the National Center for Atmospheric Research, sponsored by the National Science Foundation.

TABLE OF CONTENTS

TABLE OF CONTENTS (Continued)

LIST OF TABLES

LIST OF FIGURES

LIST OF FIGURES (Continued)

LIST OF FIGURES (Continued)

LIST OF SYMBOLS

AA	-	aircraft angle of attack
AMS	-	airborne mission scientist
A_p	-	aircraft azimuth or true heading
A_s	-	solar azimuth
a	-	layer absorptivity
$a\uparrow$,($a\downarrow$)	-	absorptivity of layer to upward, (downward) irradiance
Ci	-	cirrus cloud
CO_2	-	carbon dioxide
Cu	-	cumulus cloud
c_p	-	specific heat of air at constant pressure, 100 Joule g^{-1} $°K^{-1}$
d	-	distance from sensor to center of areal element
dA	-	areal element
F_a	-	measured fractional absorption
F_{ad}	-	fractional absorption due to dust
F_{ag}	-	fractional absorption due to gaseous constituents
$F_{a_{LL}}$	-	level to level normalized fractional absorption
$F_{a_{SL}}$	-	single level normalized fractional absorption
F_r	-	measured layer fractional reflection
F_{rd}	-	fractional reflection due to dust
F_{rg}	-	fractional reflection due to gases
FL	-	flight level
f.o.v.	-	field of view
GMT	-	Greenwich mean time
g	-	gravitational constant, 9.8 m sec^{-2}

$H\downarrow$, $(H\uparrow)$	-	downward, (upward) shortwave irradiance
$H\downarrow'$, $(H\uparrow')$	-	downward, (upward) normalized shortwave irradiance
H_A	-	incident irradiance at a reflecting areal element
H_{DF}	-	diffuse shortwave irradiance
H_{DFR}	-	Rayleigh scattered downward solar flux
H_{DFT}	-	total Rayleigh scattered downward solar flux
H_{DR}	-	shortwave irradiance on a plane perpendicular to the direct solar beam
$H\downarrow_g$	-	calculated downward shortwave flux
H_{NET}	-	difference between downward and upward solar fluxes at a given level
H'_{NET}	-	difference between normalized downward and upward solar fluxes at a given level
H_{OB}	-	measured irradiance on the plane of the pyranometer
H_{RE}	-	layer reflected shortwave energy
H_s	-	irradiance incident on a hemispheric sensor
$H\downarrow_T$	-	zenith angle corrected solar constant
H_{TR}	-	actual irradiance on a horizontal plane
HV	-	horizontal visibility
H_2O	-	water vapor
ΔH	-	layer absorbed shortwave energy
ΔH_s	-	areal element contribution to irradiance at a hemispheric sensor
h	-	height of sensor above reflecting surface
INS	-	Inertial Navigation System
IR	-	infrared radiation
i	-	level index

JD	-	Julian day number
km	-	kilometer
$L\downarrow$, $(L\uparrow)$	-	downward, (upward) longwave irradiance
L_p	-	infrared irradiance at pressure level p
$L\uparrow_{SFC}$	-	upward longwave irradiance at the surface
$L\downarrow_T$	-	downward infrared irradiance at the top of the atmosphere
L_{NET}	-	difference between downward and upward IR irradiances at a given level
LST	-	local solar time
LW	-	longwave radiation
ΔL	-	total absorbed infrared energy in a layer
mb	-	millibar
NC	-	no comment
n	-	number of levels
O_3	-	ozone
P	-	total radiant power from a hemisphere
p	-	pressure, or percentage of radiant power from a uniform source
p_o	-	standard pressure, 1013.25 mb
Δp	-	pressure interval
R	-	aircraft roll angle
R_{ar}	-	absorptance to reflectance ratio
r	-	distance from center of field of view
S_h	-	horizontal hemispheric sensor
SDL	-	Saharan dust layer (550-950 mb)
SDO	-	Saharan dust outbreak

LIST OF SYMBOLS (Continued)

SW	-	shortwave radiation
St.Cu.	-	stratocumulus cloud
T	-	temperature
T_o	-	standard temperature, 273.16 °K
T_{SFC}	-	surface temperature
ΔT	-	change in temperature or temperature increment
t	-	solar hour angle or time
Δt	-	time increment
Wm^{-2}	-	watts per square meter
W(r)	-	radial area weighting function
x	-	ratio of direct to total irradiance
Δx	-	error in direct to total irradiance ratio
$\frac{\Delta H\downarrow}{\Delta p}$	-	slope of H vs. p curve
$\frac{\Delta T}{\Delta t}$	-	measured layer heating or cooling rate
$(\frac{\Delta T}{\Delta t})_g$	-	calculated layer heating or cooling rate
$(\frac{\Delta T}{\Delta t})_{LL}$	-	level to level normalized heating rate
$(\frac{\Delta T}{\Delta t})_{SL}$	-	single level normalized heating rate
α	-	measured albedo at lowest flight level, or pressure broadening exponent
β	-	angle between normal to a plane and the solar beam, or temperature broadening exponent
δ	-	solar declination
ε^*	-	layer effective emissivity
ε^*_g	-	calculated layer effective emissivity

$\varepsilon^{*\uparrow}$, $(\varepsilon^{*\downarrow})$	-	measured effective upward (downward) layer emissivity
$\varepsilon^{*\uparrow}_g$, $(\varepsilon^{*\downarrow}_g)$	-	computed effective upward (downward) layer emissivity
$\Delta\varepsilon^{*\uparrow}$, $(\Delta\varepsilon^{*\downarrow})$	-	change in effective upward (downward) layer emissivity due to dust
ζ	-	tilt angle of plane to horizon
θ	-	solar zenith angle, or reflecting angle
θ'	-	reflecting angle
μ	-	uncorrected optical path
μ^*	-	temperature and pressure optical path
ρ	-	layer reflectivity
$\rho\downarrow$, $(\rho\uparrow)$	-	reflectivity of a layer to a downward (upward) flux
ρ_A	-	reflectivity of an areal element
ρ_L	-	reflectivity at a given level (standard reflectivity)
σ	-	standard deviation, or Stefan Boltzmann constant, 5.67×10^{-8} Wm^{-2} $°K^{-4}$
$\tau\downarrow$, $(\tau\uparrow)$	-	transmissivity of a layer to a downward (upward) flux
ϕ	-	latitude

I.0 INTRODUCTION

It has been suggested by a number of investigators that relatively heavy loadings of non-cloud aerosols may have significant effects on the atmospheric radiation budget (Charlson and Pilat, 1969; Eschelbach and Gutenberg, 1972; Vonder Haar and Cox, 1972; Reynolds et al., 1975 and Kondratyev, Welch et al., 1976). Carlson, Prospero, and Hanson (1973) found that airborne Saharan dust off the west coast of Africa appears to be, in the mean, as important as the local cloud cover in the attenuation of solar radiation. Their data reveal an average decrease of approximately 80 Wm^{-2} at local noon in the solar flux at the surface. This diminution of transmitted shortwave radiation is attributed to aerosols originating from the Sahara Desert. Kondratyev et al., (1976) found that "the most characteristic feature ... in the presence of an aerosol layer ... is a maximum of absorption in the upper part of the layer", for the Saharan dust layer during the GARP Atlantic Tropical Experiment (GATE).

Examination of observational results reported by other investigators reveals that the effects of aerosols on the atmospheric radiative budget is not really well understood. Robinson and Drummond (1971) reported a 3 to 6% increase in fractional absorption due to dust during BOMEX, but they found no corresponding increase in upward scattering. Most of their data taken at other times indicate that the amount of particulate scattering is generally less than its corresponding absorption. On the other hand, the results of Paltridge and Platt (1973), which are based on data collected off the coast of New South Wales, Australia, suggest that the extra scatter due to aerosol at least

equals if not exceeds the total aerosol absorption. Also, most of this aerosol scatter occurs above the level of maximum absorption. They also found no significant dust effects on the infrared radiative budget.

Mani and Srinivasan (1972) have also determined that the radiative effects of continental aerosols over the Rajasthan Desert are much greater in the solar spectrum than at terrestrial wavelengths. Liou and Sasamori (1975) conclude that solar radiation is the dominant factor in the aerosol radiative effect while Stowe (1974) reports that turbidity has a minimal effect (less than 1%) on the outgoing longwave flux. Calculations performed by Fischer and Grassl (1975) show that infrared cooling rates in the tropics are changed by no more than 2% in the presence of aerosols.

Conversely, Idso (1974) contends that infrared interaction with pollutant dust causes surface layer warming. Kondratyev and colleagues (1976) imply that Saharan dust plays an important role in the infrared cooling rates, especially at the top of the dust layer. A cooling rate maximum has been calculated by Welch and Zdunkowski (1976) and Ackerman, Liou, and Levoy (1976) for the top of a polluted boundary layer. And Cox (1969) suggests that the discrepancy between the observed and calculated IR cooling rates in a clear tropical atmosphere may possibly be due to the presence of non-cloud aerosols.

In this study the effects of Saharan dust aerosols on both the infrared and shortwave radiative budgets are deduced with the aid of two broadband radiative transfer routines and broadband irradiance measurements taken during the GATE in the summer of 1974.

2.0 DESCRIPTION OF THE SAHARAN DUST LAYER

A recurring feature of the atmosphere over the tropical north Atlantic is the synoptic scale Saharan dust outbreak (SDO). At times from late spring through early autumn more than half of the Atlantic Ocean between 10°N and 25°N may be blanketed by a dense haze of mineral dust. This dust is lifted from the Saharan surface during periods of strong winds which are associated with tightened pressure gradients induced by the passage of large amplitude easterly waves across north Africa. The SDO usually follows the peak of these disturbances (Prospero et al., 1976). Once airborne, the dust is then transported in the Saharan air layer, hereafter referred to as the Saharan dust layer, (SDL), which may extend from 900 mb to 550 mb in the vertical and up to $6X10^6$ km^2 (Kondratyev et al., 1976) in the horizontal. The dust layer is well defined and may travel at least as far west as Miami, Florida as part of a large scale anticyclone. A schematic depiction of the dust flow of July 30, 1974 inferred from SMS-1 visible photographs is shown in Figure 1.

The SDL may be differentiated from the "normal" maritime tropical atmosphere by several physical characteristics. Some of these traits, described by Carlson and Prospero (1972) and by Kondratyev et al., (1976), are reviewed briefly below.

1) The SDL has a base temperature which may be from 4-7°C warmer than the same level in most tropical air masses. This results in a strong inversion at the base.
2) The potential temperature is generally higher by up to 10°C than the same layer in a "typical", tropical atmosphere.

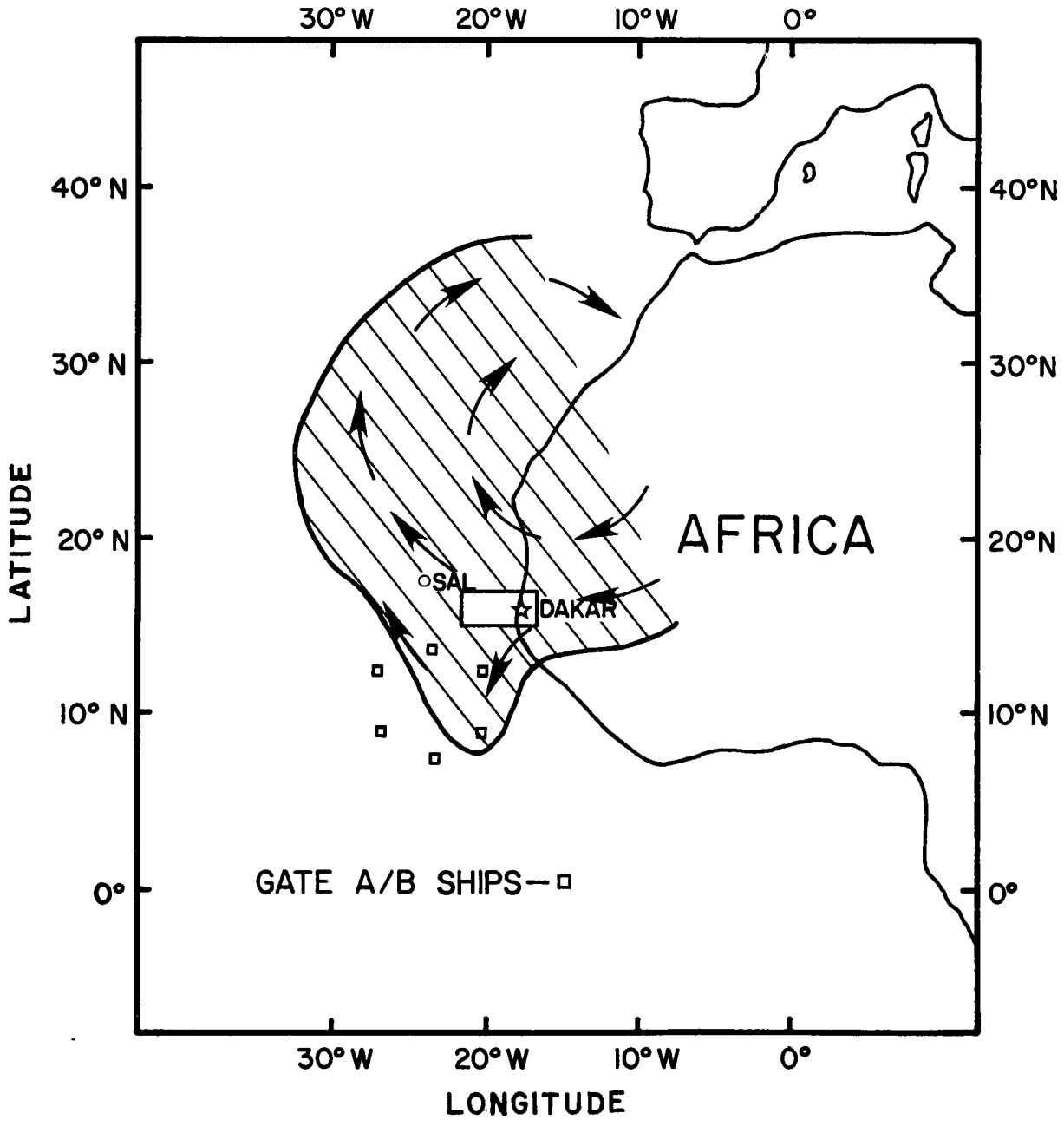

Figure 1. Approximate area of Saharan dust outbreak on July 30, 1974 is shown by the cross-hatching. An expanded view of the rectangular area around Dakar is given in Figure 3.

3) The water vapor mixing ratio within the SDL is generally lower than the "normal".

4) High concentrations, up to 2000 $\mu g\ m^{-3}$, (Carlson, 1977) of mineral dust may be present. This dust will impart a reddish brown tint to filter paper samples taken in the layer. Sometimes the layer itself may appear reddish brown.

5) Cloud development is generally suppressed and unorganized. Broken stratiform clouds are common.

6) The base of the dust layer is usually well defined due to the strong lower inversion. A distinct top coinciding with the large scale subsidence inversion is also apparent.

Examples of 1 through 3 are shown in Figure 2. These are soundings derived from data taken aboard the National Center for Atmospheric Research (NCAR) Sabreliner west of Dakar, Senegal and balloon soundings taken over Dakar. A SDO was underway over the northwest African coastal area on Julian day 211-74 and was far west of Dakar on day 217-74. An almost isothermal layer between 900 and 800 mb is apparent on day 211-74.

Of course none of the SDO's were identical nor did the dust always originate from the same surface area (Kondratyev et al., 1976), so the radiative effects of each outbreak should not be expected to be the same as those of the previous SDO. But, because there are measurements available for a number of different outbreaks during GATE, it should be possible to determine with some confidence just how large a role the Saharan dust may play in the radiative budget of the GATE A/B region.

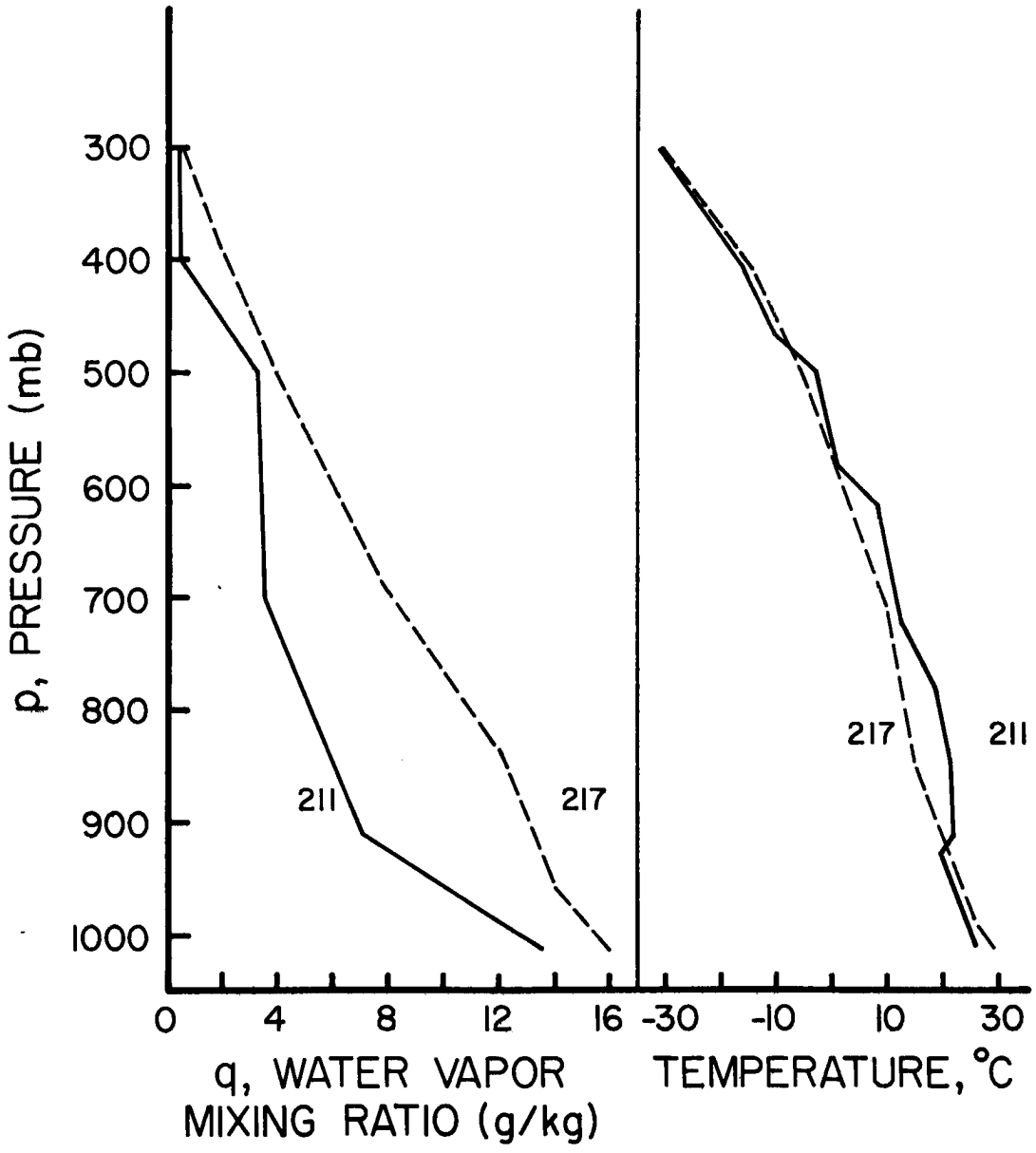

Figure 2. Vertical profiles of water vapor mixing ratio and temperature for Julian days 211 (dusty) and 217 (dust-free) in 1974 constructed from soundings taken aboard the NCAR Sabreliner and by radiosondes from Dakar, Senegal.

3.0 DATA COLLECTION AND REDUCTION

3.1 Irradiance measurement system

During GATE the NCAR Sabreliner was equipped with four broadband hemispheric radiometers - two Eppley Precision Pyranometers and two Eppley Infrared Precision Radiometers (Pyrgeometers). One pyranometer and one pyrgeometer were mounted face-up on the top skin of the fuselage parallel with the primary axes of the aircraft (Rockwood and Cox, 1976). The two other sensors were attached in a like manner, face-down, to the undersides of the wings.

The pyranometers are senistive to radiation in the spectral range of .285 - 2.8 μm while the infrared sensors respond to radiation in the 4 - 50 μm range. Irradiance measurements were taken four times per second by each radiometer. These data were then reduced to one second average readings and further corrected for temperature because of the large range of temperatures encountered during mission sorties. For complete details on the reduction and initial correction of all GATE Sabreliner radiation data see Albrecht and Cox (1976 a). Further information on the actual operating characteristics and calibration procedures of pyrgeometers may be found in Albrecht et al., (1974) and in Albrecht and Cox (1976 b).

3.2 Description of other available data

In addition to the irradiance observations, other observed parameters used in the analysis of the radiation data are listed below:

Time (GMT)	Dew Point Temperature (°C)	
Static Pressure (mb)	Angle of Attack (°)	
Ambient Temperature (°C)	True Airspeed (m/s)	True Heading (°)

All of the values for the above variables including the irradiance measurements were recorded on magnetic tape. Microfilm listings of the data, including plots of each parameter versus time, were produced from the digital magnetic tapes.

Dust and cloud conditions were established with the aid of time lapse films and the airborne mission scientists' logbooks. A 16 mm movie camera viewing the horizon through a side window of the Sabreliner exposed a frame every eight seconds. The flight scientists' notes included flight levels altitude, dustiness, location of dust layer top and base and the amount of cloudiness above and below the aircraft.

3.3 Aircraft missions

All irradiance data used in this study are taken from GATE Sabreliner missions which originated in Dakar, Senegal (14°44'N, 17°33 'W) and were flown within an area bounded by 13°30'N to 15°30'N and by 16°W to 21°06'W. This area is northeast of the GATE A/B scale array and is delineated by the rectangle in Figure 1. The locations of each flight are shown in Figure 3 and are indicated by the Julian day number of the mission. In order to minimize the possible errors due to a changing sun angle all measurements used in the analysis were taken within two hours of local noon.

Because aerosol measurements were not available on these sorties the observers' notes and time lapse films were used to categorize the degree of dustiness of the atmosphere sampled on these days. The descriptions of the dust conditions observed for each day are given in Table 1. More detailed descriptions of the flights and the sky conditions are presented in Appendix A. An example of the top of the dust

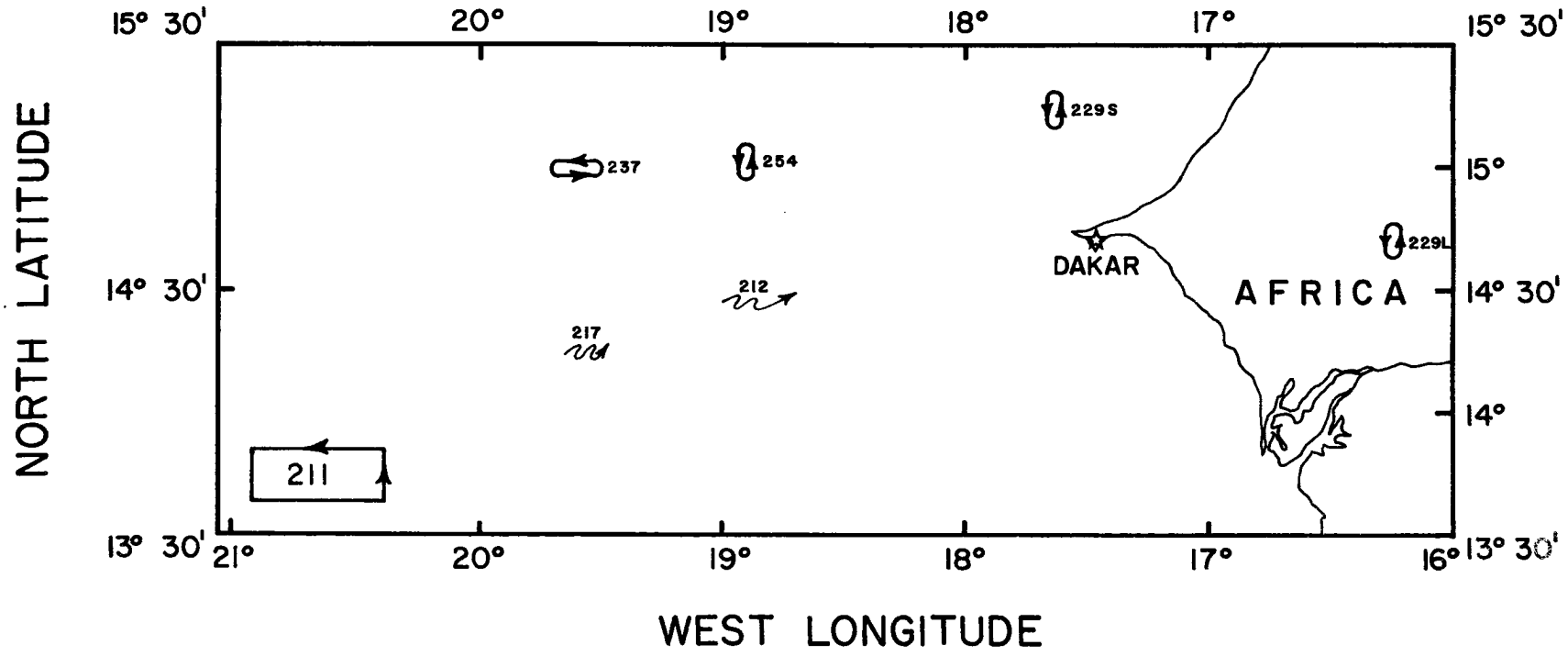

Figure 3. Flight region for Saharan dust study. Approximate flight tracks are pictured with the Julian day number.

211/July 30, 1974	Heavy dust; top ∿ 12,500 ft., base ∿ 5,500 ft.
212/July 31, 1974	Heavy dust; top ∿ 14,500 ft., base ∿ 5,500 ft.
217/August 5, 1974	Clear, no dust, some haze apparent in photographs
229/August 17, 1974	Heavy dust; top ∿ 15,500 ft., data over land and sea
237/August 25, 1974	Clear, no large amounts of dust, no haze apparent in films
254/September 11, 1974	Moderate dust, top ∿ 15,500 ft., heaviest dust in lower levels of SDL

Table 1. Flight days and dust conditions.

layer as viewed from the Sabreliner is shown in Figure 4. This photograph was taken at 20,000 feet on day 211-74.

Although the dust classifications in Table 1 are highly subjective and general, they are representative of the days described and coincide with observations and measurements reported by other GATE scientists (Kondratyev et al., 1976). Prospero, Nees, and Savoie (1976) noted that Saharan dust outbreaks reached Sal Island, Cape Verde Islands (16°45'N, 22°57'W), 600 km WNW of Dakar, on July 30, August 17, and September 11. The peak aerosol measurements recorded at Sal Island during GATE were observed one to two days following the onset of these outbreaks.

3.4 Selection of irradiance data

3.4.1 Consideration of cloud effects

Because the broken cloudiness sometimes encountered during the dust mission flights could significantly affect the irradiance measurements it was necessary to eliminate, as much as possible, those data which might be severely cloud contaminated. Sometimes these cloud effects could not be removed successfully and the entire flight leg was deleted from this study. However, when an extensive, thin cirrus cloud was present it was assumed all of the readings during the flight were affected uniformly. In this case an attempt was made to exlude only the effects due to other clouds.

Other problems which could arise are due to the fact that the Sabreliner flew alone and usually in a different pattern each flight (Appendix A). When a vertical sounding of an area is taken a single aircraft requires time to ascend and descend between levels, in addition

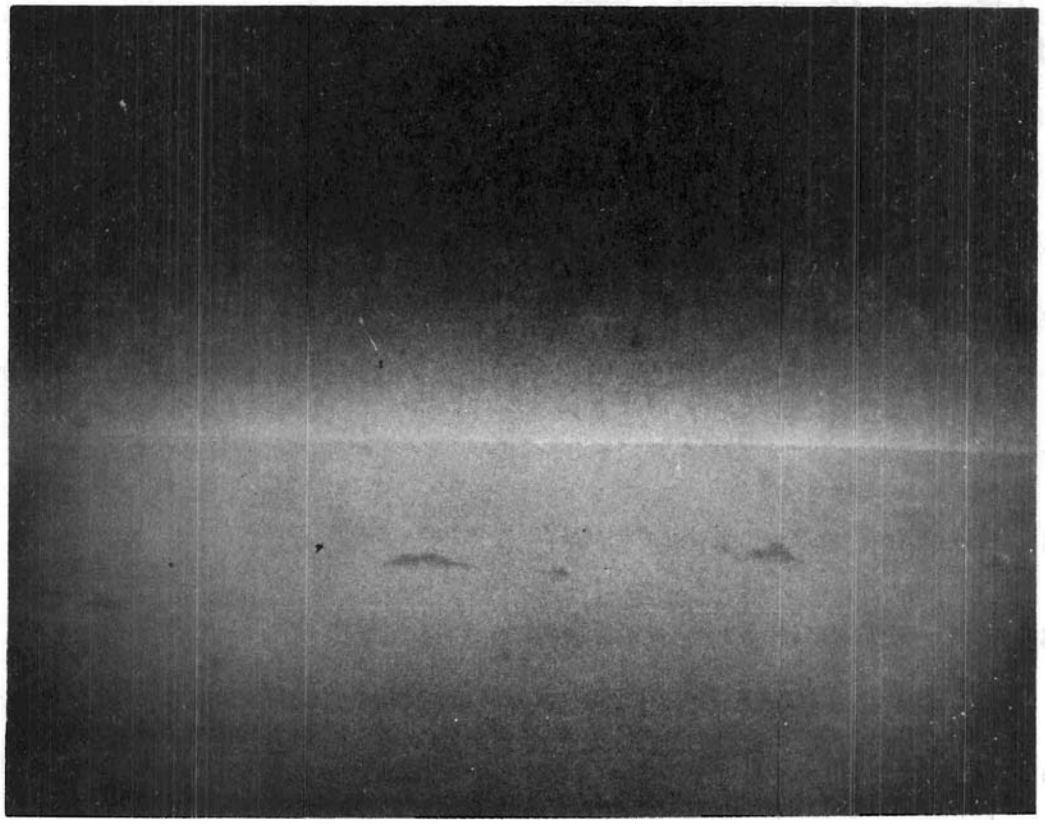

Figure 4. Photograph of the top of the Saharan dust layer as viewed from the NCAR Sabreliner at 20,000 feet on July 30, 1974. Note the distinct horizon corresponding to the top of the layer. The dark, irregular features across the lower middle part of the photograph are small clouds above the dust.

to the time needed to complete a leg. For example, during the time interval (up to a half-hour) between the beginning of flight level 1 and the end of flight level 3 the cloud field viewed by a sensor could change significantly. Also, depending on the flight pattern, an entirely different area may be viewed at each flight level. These difficulties were considered in the planning of each flight but could never be eliminated entirely. Therefore, these and other effects, which will be mentioned later were taken into account in the filtering of the data.

3.4.2 Classification of data

The first method used to screen the radiation measurements was to classify each datum point as clear or non-clear with respect to a set of criteria. This technique is based on several logical assumptions about the relationship between simultaneously measured longwave, L, and shortwave, H, fluxes.

For a clear atmosphere the incoming fluxes, H↓ and L↓, should have opposing tendencies. That is, as H↓ approaches a relative maximum value, L↓ should tend toward a minimum. For the outgoing fluxes, H↑ and L↑, the relative tendencies are just the opposite. An exception to the H↓ case may occur when the sensor passes under the edge of a cloud. In that instance the instrument may record a flux higher than the upper limit for the clear case.

When clouds are present above the sensors H↓ should approach a minimum while L↓ tends toward a maximum. These limits are reached when the sky is overcast and the clouds have an emissivity approaching unity. Clouds below should have a contrary effect on the outgoing fluxes unless

the cloud reflectivity is less than the surface albedo. This case rarely, if ever, occurs in the tropics.

There are situations, however, in which the observed H↑ reading may be lower than the clear-case minimum. This could occur when an extensive cloud, in the lower layers especially, casts a broad shadow. The magnitude of this effect depends on the height of the sensor above the reflecting surface and the size of the shadow. The problems due to clouds overhead are treated in more detail in Appendix B with a method reported by Poellet and Cox (1975). It may be seen from Appendix B that the albedo measurement in particular is especially sensitive to the cloud field.

For the initial classification of the data as clear or cloudy two test statements are required.

$$\text{If } H\downarrow \geq A \text{ and } L\downarrow \leq B \text{ then } H\downarrow, L\downarrow \text{ are clear, otherwise } H\downarrow, L\downarrow \text{ are cloudy.} \tag{1}$$

$$\text{If } H\uparrow \leq C \text{ and } L\uparrow \geq D \text{ then } H\uparrow, L\uparrow \text{ are clear, otherwise cloudy.} \tag{2}$$

To determine the limiting criteria A, B, C and D the microfilmed time series of each flux were first examined in conjunction with the flight observers' notes (Appendix A).

Relatively smooth plots (amplitude < 5 W/m^2), such as Figure 5a were generally considered clear if the observers' notes indicated that no uniform cloud field was present. For B and C the highest values of

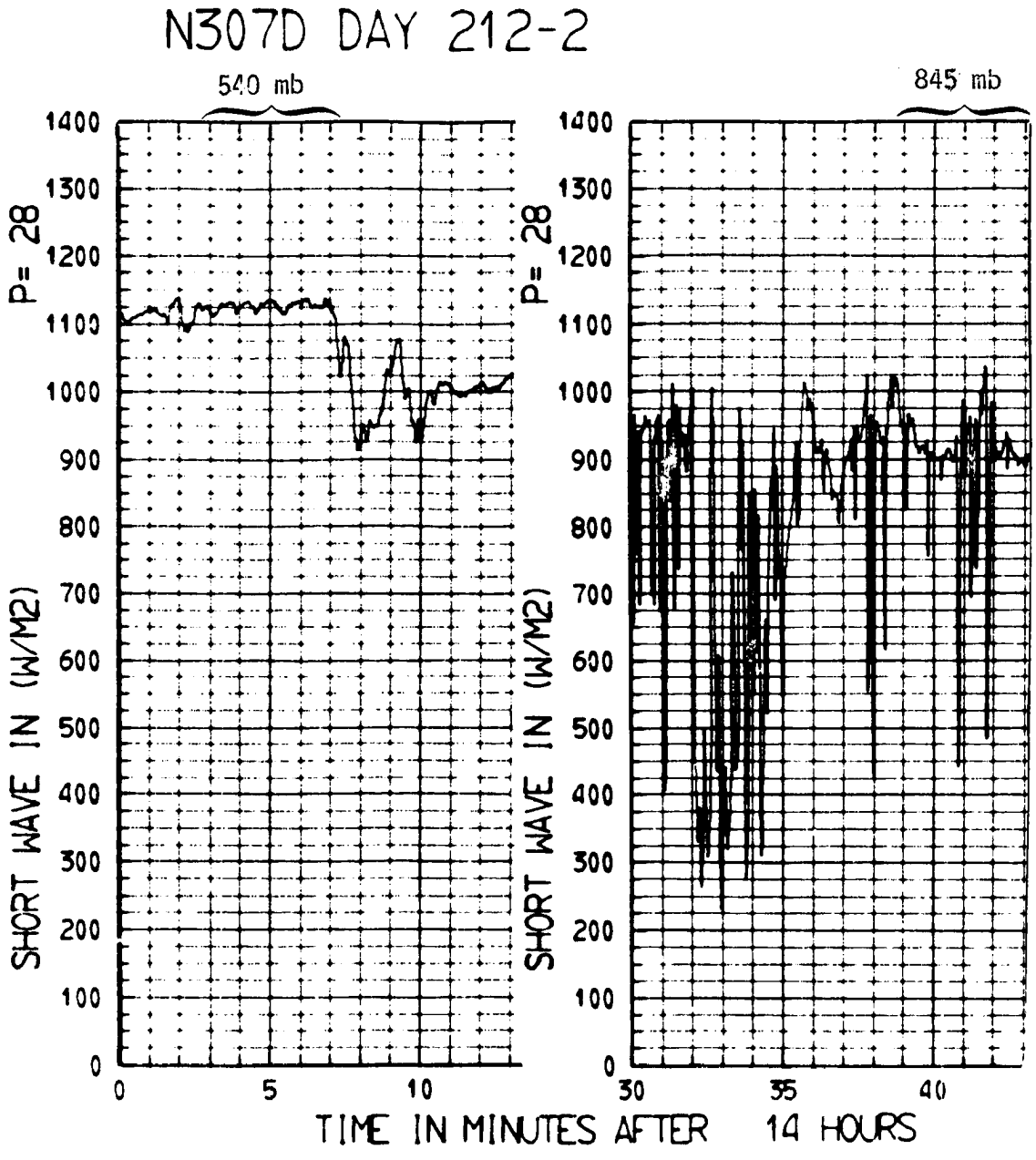

a. Clear case

b. Partly cloudy cases

Figure 5. H↓ (shortwave in) time series.

the smooth plots were used as the criteria. The lowest values were used for A and D.

For those time series which obviously did not consist of entirely clear, i.e. had highly variable (Figure 5b) readings, it was necessary to either find a smooth background level or generate histograms of the time intervals. The extreme 10% values were then chosen as the limiting values. Care was taken not to include any time segments which indicated cloud edge effects.

After selection of the test criteria the tests were performed on each datum point in a selected time segment. Averages and standard deviations for each classification and flux were derived. Geometry corrections and normalizations explained in Appendix C were performed on shortwave averages.

Next, in order to remove any more cloud effects such as those mentioned in Section 3.4.1 or Appendix B, all clear data were plotted with respect to pressure. Keeping in mind the basic assumptions mentioned earlier for the criteria test method, the plots were inspected for vertical consistency. That is, it was assured that reflectivity as well as $H\downarrow$ and $H\uparrow$ increase with increasing height.

Levels which did not follow these guidelines were removed from the analysis. It is now assumed that the remaining flight legs view essentially the same sky conditions and that these data are as uncontaminated by clouds as possible. The selected longwave irradiance data were averaged for each flight leg. The mean values for pressure, ambient temperature, dew point, angle of attack, true heading, and roll angle were determined for each flight level after testing each one second reading against a loose set of limits. Time, latitude, and longitude

were also averaged. When no INS (Inertial Navigation System) data were available the average latitude and longitude for each leg were found from the distance plots mentioned in Section 3.2.

4.0 TECHNIQUES FOR INFERRING THE RADIATIVE EFFECTS OF THE SAHARAN DUST

4.1 Differencing technique for shortwave data

For a meaningful comparison between observed and computed data it is desirable to use parameters which are based on a term common to both types of data. In an atmospheric shortwave radiation budget the one constant at any given time is the solar constant. For this study two parameters, layer fractional absorption and layer fractional reflection, based on the adjusted solar constant, $H\downarrow_T$, are used to compare the observed and computed irradiance values. Instantaneous heating rates calculated from the measured and computed fluxes will also be used to describe these dust effects.

4.1.1 Fractional absorption

Consider an atmospheric layer in Figure 6 between levels 1 and 2. The fractional absorption for this layer according to Yamamoto (1962) is

$$F_a = \frac{H_{NET_1} - H_{NET_2}}{H\downarrow_T}, \qquad (3)$$

where $H\downarrow_T$ = SC cos θ and SC is the solar constant, 1396 Wm^{-2} (Cox et al., 1976) while θ is the solar zenith angle. H_{NET_1} and H_{NET_2} represent the differences between $H\downarrow$ and $H\uparrow$ at levels 1 and 2 respectively. This absorptivity is the result of absorption of shortwave radiation by gases, clouds, and non-cloud aerosols, such as mineral dust and sea salts, in the layer. If the variation of temperature and gaseous concentrations are known in the vertical and no clouds are present then a

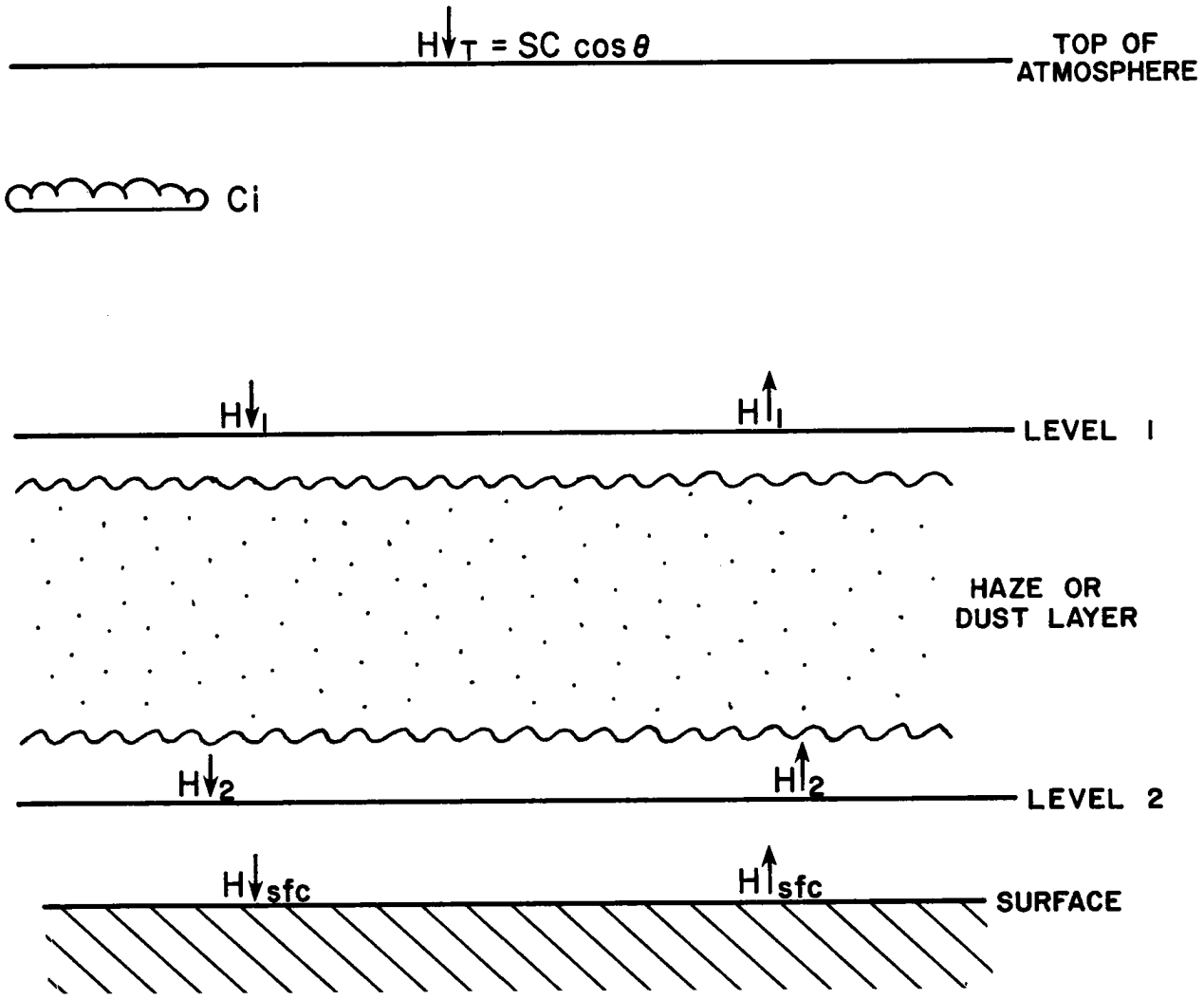

Figure 6. Schematic depiction of shortwave irradiances used in this analysis.

fractional absorption, F_{ag}, due to the gases alone may be calculated for the layer.

The difference, F_{ad}, between the measured and computed fractional absorptions is

$$F_{ad} = F_a - F_{ag}, \tag{4}$$

and is assumed to arise from the presence of aerosols in the layer. F_{ad} may result both from direct absorption by the aerosols and indirectly through increased gaseous absorption. This indirect enhancement is due to a change in path length caused by the aerosol scattering.

4.1.2 Fractional reflection

For a layer such as 1-2 in Figure 6 the upward flux, $H\uparrow_1$, at the top of the layer is the sum of that portion of $H\uparrow_1$ reflected by the layer itself, H_{RE}, and the portion of $H\uparrow_2$ which is transmitted through the layer. Or,

$$H\uparrow_1 = H_{RE} + H\uparrow_2 \tau\uparrow \tag{5}$$

where $\tau\uparrow$ is the transmissivity of the layer to a given upward flux of radiation. Rearranging (5) yields

$$H_{RE} = H\uparrow_1 - H\uparrow_2 \tau\uparrow. \tag{6}$$

To obtain the layer fractional reflection, defined as that fraction of the solar flux incident at the top of the atmosphere which is

reflected by the layer, equation 6 is divided by $H\downarrow_T$.

$$F_r = \frac{H_{RE}}{H\downarrow_T} . \tag{7}$$

However to find H_{RE}, $\tau\uparrow$ must be determined for the layer. From a statement of energy conservation,

$$\tau\uparrow = (1 - a\uparrow - \rho\uparrow), \tag{8}$$

where $a\uparrow$ is the absorptivity of the layer due to absorption of part of the incoming upward flux, and $\rho\uparrow$ is the reflectivity of the layer to $H\uparrow_2$.

The total absorptivity, a, of a layer 1-2 is defined by Reynolds et al., (1975) as

$$a = \frac{H_{NET_1} - H_{NET_2}}{H\downarrow_1} . \tag{9}$$

This absorptivity actually results from absorption by the layer of portions of both fluxes, $H\downarrow_1$ and $H\uparrow_2$, incident on the layer.

If it is assumed that the fraction of the total absorptivity due to absorption in a given direction is proportional to the fraction of the total incoming flux, $H\downarrow_1 + H\uparrow_2$, from the same direction, then the absorptivity, $a\uparrow$, of the layer to an upward flux is

$$a\uparrow = \frac{H_{2\uparrow}}{H_{1\downarrow} + H_{2\uparrow}} \; a. \tag{10}$$

The reflectivity, $\rho\downarrow$, of a layer to a downward flux, may be defined, according to Cox (1975) and equation 6 as

$$\rho\downarrow = \frac{H\uparrow_1 - H\uparrow_2 \tau\uparrow}{H\downarrow_1} . \tag{11}$$

If it is assumed that a given atmospheric layer reflects isotropically then the fraction, $\rho\uparrow$, reflected out of an upward flux and the fraction, $\rho\downarrow$, reflected out of a downward flux should be the same. Or,

$$\rho = \rho\uparrow = \rho\downarrow \tag{12}$$

where ρ is the layer reflectivity. Substituting equation 12 into (8) and (11) yields

$$\rho = \frac{H\uparrow_1 - H\uparrow_2 (1 - a\uparrow - \rho)}{H\downarrow_1} . \tag{13}$$

Rearranging (13) results in

$$\rho = \frac{H\uparrow_1 - H\uparrow_2 (1 - a\uparrow)}{H\downarrow_1 + H\uparrow_2} . \tag{14}$$

Knowing ρ from (14) and $a\uparrow$ from (10), $\tau\uparrow$ may now be found with equation 8. And finally, F_r may be calculated from equations 6 and 7.

Similar to the method described in section 4.1.1 the fractional reflection due to the dust, F_{rd}, is found by calculating F_r from the

measured fluxes, computing F_{rg}, the fractional reflection for the computed fluxes, and differencing the two, i.e.:

$$F_{rd} = F_r - F_{rg}. \tag{15}$$

Since H_{RE} is based on $H\uparrow_1$ and $H\uparrow_2$ for a given layer F_r is not additive for successive layers. However, a total fractional reflection for a number of layers together may be found using (7) if H_{RE} is computed with values for $H\uparrow_1$ at the top of the highest layer, and $H\uparrow_2$ at the bottom of the lowest layer. This value of F_{rd} will give the cumulative effects of aerosols upon the entire layer.

4.1.3 Heating rates

Another parameter useful for visualizing the radiative effects of the dust layer is the layer heating rate, $\frac{\Delta T}{\Delta t}$.

$$\left(\frac{\Delta T}{\Delta t}\right)_{1,2} = - \frac{g}{cp} \frac{H_{NET_1} - H_{NET_2}}{\Delta p_{1,2}} \tag{16}$$

where $\Delta p_{1,2}$ is the difference in pressure between levels 1 and 2. Because of the low resolution of the observations the average heating rates for the measurements are calculated for each layer between flight levels and plotted with respect to pressure. The heating rates calculated for a "clean" gaseous atmosphere, $\left(\frac{\Delta T}{\Delta t}\right)_g$, are plotted on the same graph for visual comparison (see Chapter 5.) The differences in heating rates are then examined with the use of these diagrams.

4.2 Shortwave model

The radiative transfer routine employed here to calculate clear sky heating rates, fractional absorption, and fluxes in the shortwave spectral region is IRADS02, a broadband model described by Cox et al., (1976). This program computes the amount of solar radiation absorbed by each layer of the atmosphere utilizing specified vertical structures for temperature, water vapor, carbon dioxide, and ozone. First order Rayleigh scattering of 7% is included in the computations by means of a pressure weighting scheme. The effects of a cloud layer or surface are also incorporated in this routine with the use of a value of cloud reflectivity and absorptivity or with a value of surface albedo. A more comprehensive outline of the model may be found in the reference noted above.

4.2.1 Specification of input parameters

The calculations performed in IRADS02 are valid only for a single set of boundary conditions. At the top of the atmosphere the incoming flux, $H_{\downarrow_T}$, depends on the day, the time, and the location. Values for these parameters were derived for each day, and are given in Appendix A.

Since clear sky (no aerosols) absorption and heating rates depend only on the temperature and pressure and on the concentrations of the gaseous absorbers, vertical profiles of each gas and of the temperature were specified for each day. An average tropical Atlantic summer sounding of the ozone mixing ratio used in Cox et al., (1976) was employed in all the computations. Carbon dioxide was assumed to be completely mixed at a constant concentration of .486 g kg^{-1}.

For accurate calculations it is desirable to use temperature and moisture profiles which have a resolution that is finer than those obtained by using only the mission flight level data. Therefore, a more detailed picture of the vertical structure of these variables was constructed by combining the aircraft soundings with the 1200 GMT Dakar radiosonde measurements for each day considered, and interpolating linearly to each 50 mb level.

It was found that the flight level values agreed quite well ($\pm$ 1°C) with the corresponding values from the Dakar soundings, except in the very lowest levels (> 925 mb) where land-sea differences could create the greatest discrepancies. In those instances the lower layer values were interpolated from the flight data. When inflight measurements were not available at these levels, estimates were made from the data of a similar day.

The values for lowest flight level reflectivity found from the measurements were used in the model. In this way it was ensured that the surface or cloud boundary conditions were the same for the observations and the model.

4.2.2 Model output

Values for $H\downarrow_g$ and $H\uparrow_g$ were calculated for every 50 mb level. The subscript g refers to flux values derived by IRADSO2 for a gaseous atmosphere. Heating rates, $(\frac{\Delta T}{\Delta t})_{g_{i,\,i+1}}$, were also computed and listed in °C hr^{-1} using the following version of equation 16.

$$(\frac{\Delta T}{\Delta t})_{g_{i,i+1}} = - \frac{g}{cp} \frac{\Delta H_{g_{i,\,i+1}}}{\Delta p}, \; i = 1,n \qquad (17)$$

where $$\Delta H_{g_{i,\,i+1}} = H_{NET_{g_i}} - H_{NET_{g_{i+1}}}, \qquad (18)$$

n is the number of levels, and Δp = 50 mb. A finer resolution was also calculated through an interpolation scheme.

Layer fractional absorption, $F_{ag_{i,\,i+1}}$, and layer fractional reflection values, $F_{rg_{i,\,i+1}}$, were then calculated from the flux data. It will be seen in Chapter 5 that the agreement between IRADS02 values and the fluxes measured for a clear day are quite good, especially for pressures greater than 550 mb.

4.2.3 Sensitivity of shortwave calculations to errors in temperature and moisture profiles.

The model was tested for its response to various errors in input parameters to estimate the precision of the results. Using meteorological data from day 212 it was found that IRADS02 is not highly responsive to changes in moisture measurements, a variation of less than 2% may be expected for the calculated fractional absorption or reflection values. Heating rates appear to be slightly more sensitive but only because they are based on a 100 mb layer rather than on one 400 mb thick.

The possibilities of a $\pm$ 3°C temperature bias, of a random temperature perturbation ($\sigma = \pm$ 1°C), and of an error in the measured latitude ($\pm$ .5°) affecting the model results were also explored. It was found that changes of less than 0.1% in any parameter were the result of the above errors. Therefore, it may be assumed that the model results are affected only by the moisture specifications, and that the parameters calculated from these results are reliable to within $\pm$ 2%.

The errors which may be introduced during the measurement and correction of the irradiance data are discussed in Appendix C. From this discussion it was estimated that errors of $\pm$ .005 and $\pm$ .002 are likely for measured values of fractional absorption and reflection respectively. Heating rate errors of $\pm$ .012 °C hr^{-1} were also estimated for a 140 mb layer.

4.3 Method for inference of dust effects in the infrared

The technique for inferring the infrared effects of the Saharan dust layer makes use of a broadband infrared radiative transfer routine to compute longwave irradiances for a dust-free atmosphere. Cooling rates and effective layer emissivities are calculated for both the dust-free irradiance values and the observed infrared fluxes. Similar to the shortwave method the differences between the two values for each parameter are assigned to dust effects.

Consider an atmospheric layer between levels 1 and 2 as shown in Figure 7. T_{SFC}, T_1, and T_2 are the temperatures at the surface, level 1, and level 2 respectively. $L\uparrow_{SFC}$, $L\uparrow_1$, and $L\uparrow_2$ are the upward longwave fluxes at the same levels, while $L\downarrow_T$, $L\downarrow_1$, and $L\downarrow_2$ refer to the downward infrared fluxes at the top of the atmosphere, level 1, and level 2. The effective upward $\varepsilon^*\uparrow$, and downward, $\varepsilon^*\downarrow$, emissivities for this layer, as defined by Cox (1971) are

$$\varepsilon^*\uparrow = \frac{L\uparrow_2 - L\uparrow_1}{L\uparrow_2 - \sigma T_1^4}, \tag{19}$$

and

$$\varepsilon^*\downarrow = \frac{L\downarrow_2 - L\downarrow_1}{\sigma T_2^4 - L\downarrow_1}, \tag{20}$$

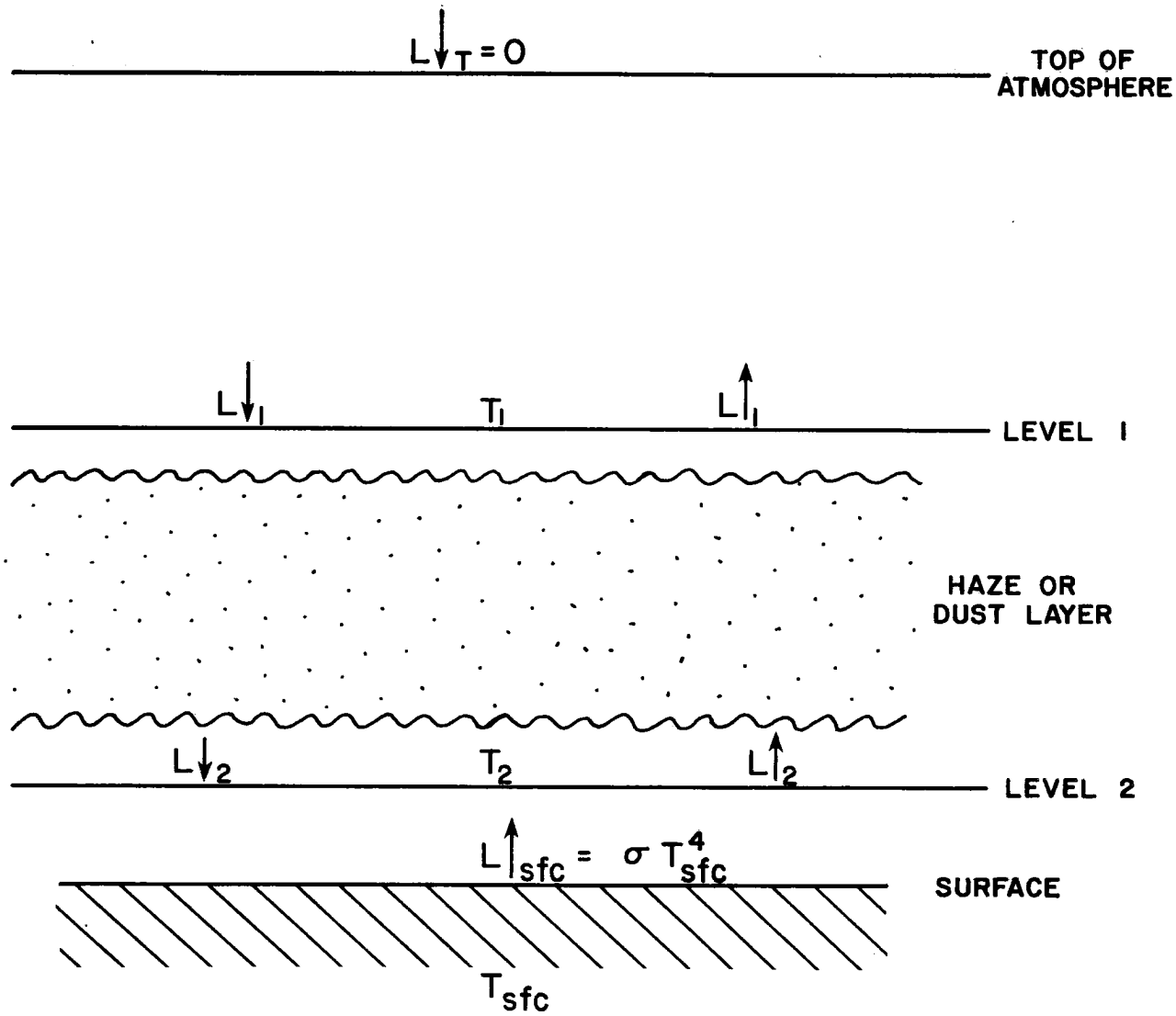

Figure 7. Schematic depiction of infrared parameters used in this study.

where σ is the Stefan-Boltzmann constant. These expressions include the effects of all components of the layer: water vapor, carbon dioxide, ozone, clouds and other radiators, such as dust.

Employing a broadband radiative transfer model one may calculate the fluxes at any given level for an atmosphere containing the same gaseous profile as the observed case but with no dust or clouds. With these derived flux values the effective emissivities due to the gaseous radiators alone, $\varepsilon^{*\uparrow}_g$ and $\varepsilon^{*\downarrow}_g$, may be determined. Now, assuming that dust is the only non-gaseous radiator in the layer for the observed fluxes, the change in effective emissivities due to the dust are

$$\Delta\varepsilon^{*\uparrow} = \varepsilon^{*\uparrow} - \varepsilon^{*\uparrow}_g, \tag{21}$$

and

$$\Delta\varepsilon^{*\downarrow} = \varepsilon^{*\downarrow} - \varepsilon^{*\downarrow}_g. \tag{22}$$

The infrared cooling rate in the layer, $(\frac{\Delta T}{\Delta t})_{1,2}$, is

$$(\frac{\Delta T}{\Delta t})_{1,2} = - \frac{g}{cp} (\frac{\Delta L}{\Delta p})_{1,2}, \tag{23}$$

where

$$\Delta L_{1,2} = L_{NET_1} - L_{NET_2} \tag{24}$$

and L_{NET_1} and L_{NET_2} represent the differences between $L\downarrow$ and $L\uparrow$ for layers 1 and 2 respectively. The change in the cooling rates due to

the dust is found by differencing the cooling rates of the computed fluxes and the cooling rates of the measured irradiances.

The changes in cooling or heating rates, however, are best seen by examination of graphs of the observed and calculated cooling rates versus pressure.

4.3.1 Infrared model

The broadband infrared radiative transfer routine used in this evaluation is IRADLON, Cox (1973), a routine which solves a finite difference form of the radiative transfer equation at ten millibar intervals. It takes into account the contributions of various atmospheric constituents with the following form:

$$L_p = L_o \left[1 - \sum_{i=1}^{N} \Delta\varepsilon_{iH_2O} - \sum_{i=1}^{N} \Delta\varepsilon_{iCO_2} - \sum_{i=1}^{N} \Delta\varepsilon_{iO_3}\right.$$

$$\left. - \sum_{i=1}^{N} \Delta\varepsilon_{i_{CLOUD}} + \sum_{i=1}^{N} \Delta\varepsilon_{i_{OVERLAP}}\right] + \sum_{i=1}^{N} L_i \left[\Delta\varepsilon_{iH_2O}\right. \qquad (25)$$

$$\left. + \Delta\varepsilon_{iCO_2} + \Delta\varepsilon_{iO_3} + \Delta\varepsilon_{i_{CLOUD}} - \Delta\varepsilon_{i_{OVERLAP}}\right]$$

where L_p is an upward (downward) flux at pressure level p and L_o is the initial upward (downward) flux at the surface (top of the atmosphere) as shown in Figure 7. The left half of the right side of equation 25 represents the transmitted term from the surface below (above).

$L_i = \sigma T_i^4$ where T_i is the average temperature in °K of the layer i. The $\Delta\varepsilon_i$ terms are the emissivity increments in the layer i from each of the subscripted increments. The subscript OVERLAP refers to the H_2O - CO_2 gaseous overlap region and the subscripts H_2O - CO_2 as cloud overlap correction.

The gaseous emissivity data used were compiled from several authors while collision broadening was taken into account by a parameterization of the following form:

$$\mu^* = \mu \left(\frac{P}{P_o}\right)^{\alpha} \left(\frac{To}{T}\right)^{\beta}, \tag{26}$$

where μ is the optical path. Cloud emissivities are confined to the layer specified in the input and values are assigned by the user. For a more complete description of this model and a similar version the reader is referred to Cox et al., (1976) and Griffith and Cox (1977).

The vertical profiles of the emitting gases and of the temperatures are the same as those used in the shortwave model (Section 4.2). It was found that the assumption $L\downarrow_T = 0$ resulted in consistently low values for $L\downarrow$ in the upper half of the atmosphere. Since calculations of $\varepsilon^*\uparrow_g$ and $\varepsilon^*\downarrow_g$ for a given layer, used in comparing observed values of $\varepsilon^*\uparrow$ and $\varepsilon^*\downarrow$, require that $L\uparrow_{2g} = L\uparrow_2$ and that $L\downarrow_{1g} = L\downarrow_1$, respectively, it was necessary to make an adjustment in the calculations. The emissivities of the atmosphere outside of the SDL were determined by the model and used to compute the initial upper and lower boundary irradiances, $L\uparrow_{2g}$ and $L\downarrow_{1g}$, which were necessary to establish the equalities at the dust layer boundaries.

After these flux values were calculated and plotted, $\varepsilon^{*}\uparrow_g$ and $\varepsilon^{*}\downarrow_g$ were computed for the desired layers. Heating rates were also determined at every 20 mb interval and plotted for comparison with the observations.

4.3.2 Infrared model sensitivity

The IRADLON model was tested for its sensitivity to changes in input parameters in a manner similar to that used for IRADSO2. The moisture data were uniformly decreased and increased between 400 and 1012 mb for day 212 by increments of 10%. The observed moisture profile was then held constant while a temperature bias of 3°C was introduced into the temperature profile to determine the effect of an instrument offset. A test for sensitivity to random errors in temperature was also performed using random perturbations of temperature with a standard deviation, σ, equal to 1°C.

Effective emissivities for the 550-950 mb layer were calculated from the irradiances derived by the model for each test situation. These results were then compared to the emissivities computed for the observed profiles for day 212. The differences are summarized in Table II. It may be seen from these data that the calculation is as responsive to random temperature perturbations as it is to a 10% decrease in moisture for $\varepsilon^{*}\downarrow$. However, for the $\varepsilon^{*}\uparrow$ case, neither the temperature bias nor the random temperature errors produce as much response by the model as does a 10% decrease in water vapor. Compared to IRADSO2, at least with respect to the layer parameters, the infrared routine is much more dependent on an accurate specification of the vertical structures of temperature and water vapor mixing ratio, as would be expected.

% of measured H_2O vapor in the 400-1012 mb layer	$\varepsilon^{*\downarrow}_g$ = .8942		$\varepsilon^{*\uparrow}_g$ = .6912	
	$\Delta\varepsilon^{*\downarrow}$	$\%\varepsilon^{*\downarrow}_g$	$\Delta\varepsilon^{*\uparrow}$	$\%\varepsilon^{*\uparrow}_g$
50	.193	21.5	.099	14.0
60	.151	16.8	.085	11.9
70	.120	13.4	.071	9.9
80	.070	7.8	.050	7.1
90	.036	4.0	.030	4.3
120	.063	7.0	-.031	4.5
(Mean) 78.	.105	11.7	.061	8.8
$\frac{\Delta T}{\text{Error in each temperature measurement}} \pm 3°C$	.019	2.1	.009	1.3
Random ($\sigma = \pm 1°C$)	.035	3.9	.015	2.3

TABLE II. Changes in IRADLON derived effective emissivites for the 550-950 mb layer due to changes in observed moisture and temperature profiles.

Using observed data with an expected accuracy of $\pm$ 10% for absolute humidity and $\pm$ 1°C for temperatures, errors of 8% in $\varepsilon^{*}{}_{\downarrow g}$ and 7% in $\varepsilon^{*}{}_{\uparrow g}$ are likely in computed emissivity values.

Cooling rates were also calculated for the 850-950 mb and 550-650 mb layers from the sensitivity test's irradiances. It was found that errors of up to 8% in 100 mb heating rates may be expected for an error of 10% in the 400-1012 mb moisture data. On the average random temperature errors ($\sigma = \pm$ 1°C) produce uncertainties of 7% in the 100 mb heating rates. Bias errors of $\pm$ 3°C result in errors of only 4%. From both random temperature errors and an inaccuracy of $\pm$ 10% in the humidity input, an error of approximately 10% of $\pm$ .01°C/hr 100 mb may result.

4.3.3 Irradiance measurement errors

Although most of the errors in the infrared irradiance measurements have been minimized during the data reduction procedures, the flux observations chosen for averaging still depend on some subjective decisions. The effects of a possible bias error in the instrument must be considered. In order to estimate the effects of errors in selection criteria, random perturbations were imposed on the irradiance measurements based on the typically largest standard deviation for a given flight. For $L\uparrow$ the standard deviation of these perturbations was selected as 2.5 Wm^{-2} and for $L\downarrow$, σ = 5.2 Wm^{-2}.

It was found that on the average for day 229L $\varepsilon^{*}\downarrow$ may vary by 2.1% or $\pm$ .016, and $\varepsilon^{*}\uparrow$ may change by only 1.4% under the randomly perturbed conditions. On the other hand $\varepsilon^{*}\uparrow$ varied by 3.1% in the mean and $\varepsilon^{*}\downarrow$

changed by only 1.6% when the flux profiles were subjected to uniform bias errors of $\pm$ 5 Wm^{-2}.

Heating rate errors resulting from randomly perturbed fluxes averaged .017°C hr^{-1} for the three layers below 531 mb. This corresponds to an average error of 6 Wm^{-2} in ΔL for each layer which is slightly larger than might be expected from the measurements. The bias error would have no effect since it is uniform and cooling rates are based on a difference of four fluxes.

Another source of error which may affect the calculations of effective emissivities from observed fluxes arises from the use of a temperature which is interpolated from measurements which are accurate to only $\pm$ 1°C. It was found that if the upper (lower) level temperature is in error by $\pm$ 1°C then $\varepsilon^{*}\uparrow$ ($\varepsilon^{*}\downarrow$) will be inaccurate by 2.5%. For average uncertainties of $\pm$ 2°C these parameters will vary by 5%. Given these sources of error a reasonable estimate of the total uncertainty in ε^{*} which is likely to occur is $\pm$ 5% of the values calculated from the observed irradiances.

Considering both the measurement errors and the sensitivity of the model, a discrepancy of 10% between ε^{*} and ε^{*}_{g} values for a clear day is possible.

5.0 RADIATIVE CHARACTERISTICS OF THE SAHARAN DUST LAYER

The analytical methods of the previous chapter are applied to the data described in Chapter 3 to derive shortwave and longwave parameters for both clear sky calculated fluxes and observed irradiances. The derived values of these parameters for the atmospheric layer (SDL) between 550-950 mb are presented and discussed below.

5.1 Dust-free cases

Although estimates of the errors involved in this analysis are discussed in Chapter 4 and Appendix C, a simpler, and possibly more reliable method for estimating the noise level, makes use of data taken on dust-free days. By computing the differences between the model derived and observation based parameters an indication of the precision, not only of the models and measurements but also of the observers' notes, may be obtained. Data from days 217 and 237 are used to verify the expected precision of the differencing technique.

5.1.1 Shortwave parameters

Instantaneous normalized solar flux data for day 237 are depicted in Figure 8 together with the IRADSO2 derived flux profiles. From the graph it is apparent that the agreement between measured and computed flux values is quite good below 500 mb for H↓ and throughout the atmosphere for H↑. Close agreement below 500 mb may also be seen in the right half of Figure 9 for the heating rates of the same day. The discrepancies above this level may arise from several sources. The input moisture data may be inaccurate in the upper levels, the measurements at 240 mb may be in error (but not by 40 Wm^{-2}), or the model may

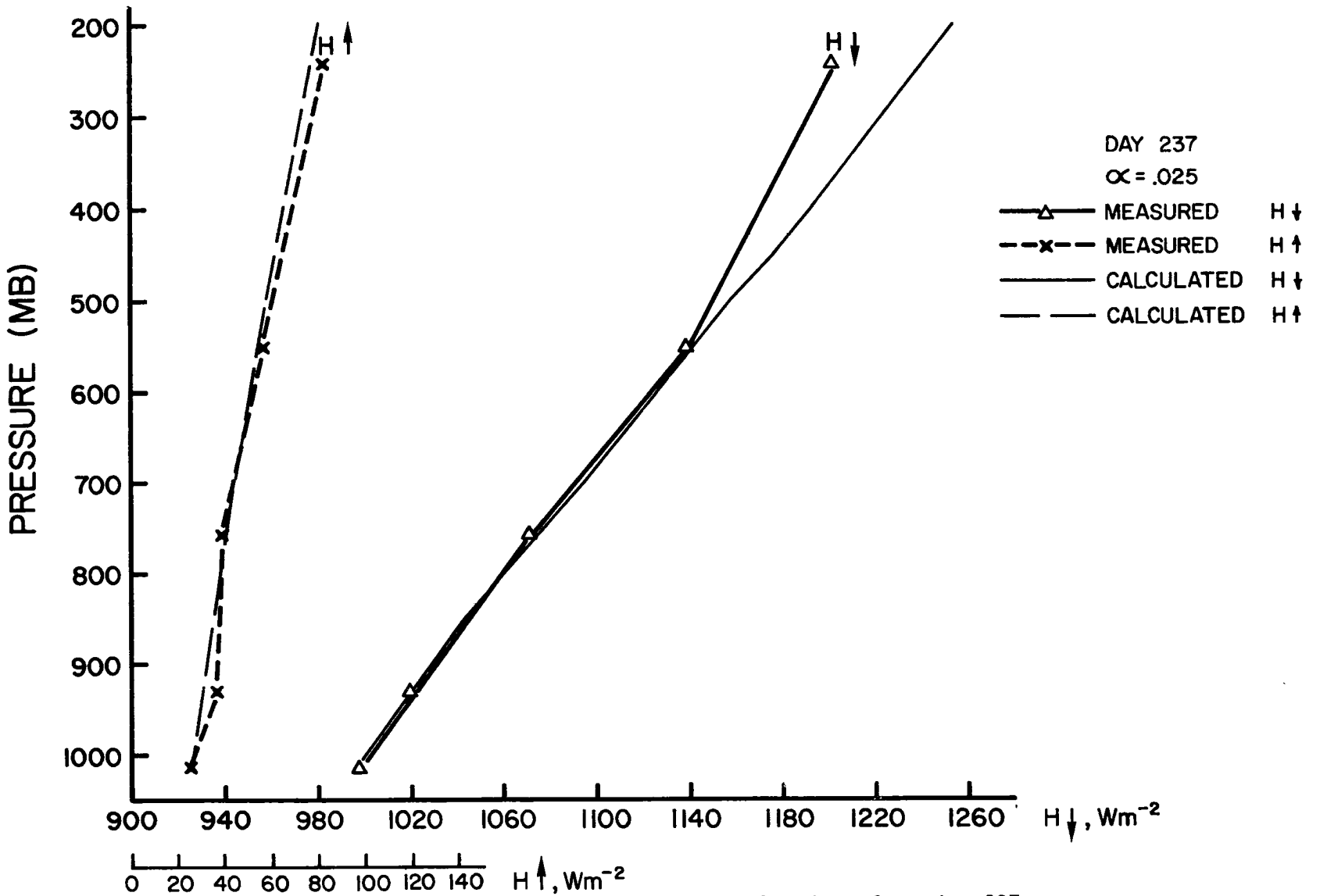

Figure 8. Measured and computed shortwave irradiances for dust-free day 237.

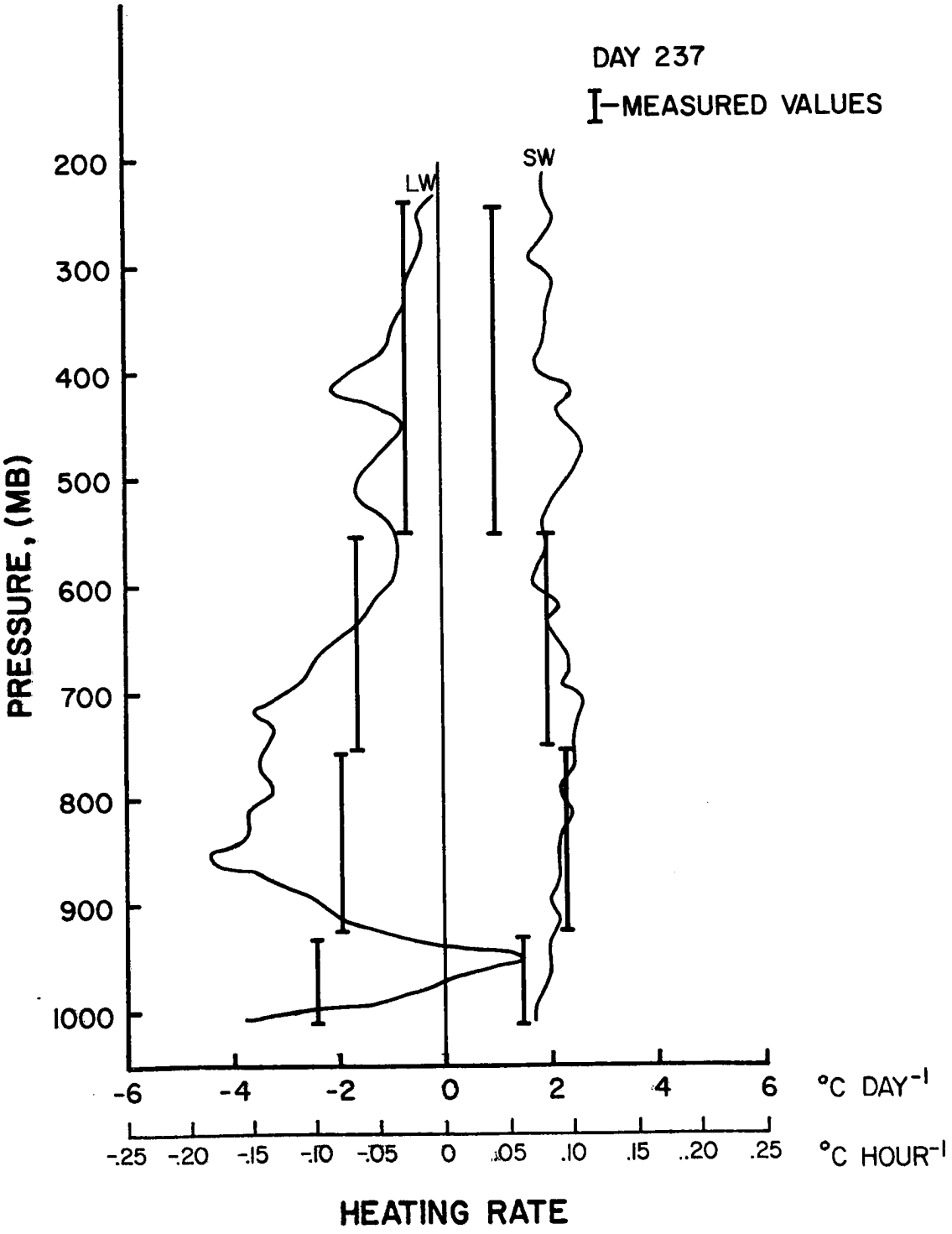

Figure 9. Measured and computed heating rates for both longwave (LW) and shortwave (SW) absorption on dust-free day 237.

not calculate enough absorption in the stratosphere. This difference in the upper levels is apparent for all of the calculation - measurement comparisons above 400 mb. However, for the total atmosphere the fractional absorption and reflection are nearly the same for both the measured and calculated data.

The irradiance data for day 217 also reveal the same type of vertical structure; however, there is an offset of a few watts per square meter between the observed and computed H↓ values. The agreement for H↑, though, is quite good.

From the flux data for these two days it was found that the average fractional absorption and reflection coincided well with the calculated parameters. An average difference of only .0006 or 0.8% was found between the observed and calculated values of fractional absorption for the SDL which is considerably less than the estimate of .005 error in F_a given in 4.2.3. For fractional reflection this difference is approximately .0018, slightly less than the error estimate. In absolute terms, however, the difference in reflected energy, ΔH_{RE}, is only 2.4 Wm^{-2}, almost within the resolution of the instrument. Furthermore, with respect to the total energy reflected by the atmosphere this error in F_r is only 3.1%, nearly the same as that estimated in 4.2.3.

The heating rates for these same cases agree quite well. On day 237 the heating rates agree to within $\pm$ .007°C hr^{-1} between 550 and 950 mb on the average. However, on day 217 the average discrepancy in the SDL is $\pm$ .03°C hr^{-1} for a layer of 133 mb which corresponds to an error of 10 Wm^{-2} in ΔH. For the entire layer these errors cancel out indicating that there is a measurement or selection error at some middle level in this flight. Further examination of the flux data for

day 217 revealed that the $H\uparrow$ value observed at 845 mb was contaminated by the presence of clouds below. Overall for both days the average difference in heating rates is approximately .019°C hr^{-1} for a 130 mb layer. This value is nearly 60% higher than previously estimated in Section 4.2.3.

Error estimates derived in the above mode for only two data sets provide no statistically reliable indication of the actual uncertainties expected in this analysis. However, the agreement between the shortwave parameters, being within the earlier estimates of possible errors, indicates that the two days described as "clean" are indeed dust-free, assuming that the dust produces some measurable effect. Also this comparison between calculated and observed data for the "clean" days gives an indication of the magnitude of the noise level for this analysis.

Employing the estimates from this section and those from Chapter 4 new approximations may be made for the size of expected errors in these parameters. Any differences between the calculated and observed parameters which exceed these error limits are considered to be dust-caused effects. For the 550-950 mb layer the expected departures from the IRADS02 derived fractional absorption and reflection are no more than 3% and 5%, respectively, of the total shortwave energy absorbed and reflected by the atmosphere. At a resolution of 100 mb the expected errors in fractional absorption and reflection are $\pm$ .002 and $\pm$ .0015 respectively, based on the standard deviations for all four 100 mb layers for days 217 and 237 which are depicted in Figures 10 and 11. Also, for a 100 mb layer the expected precision of the heating rate calculations is estimated to be $\pm$ .015°C hr^{-1} or $\pm$ 4 Wm^{-2} in ΔH.

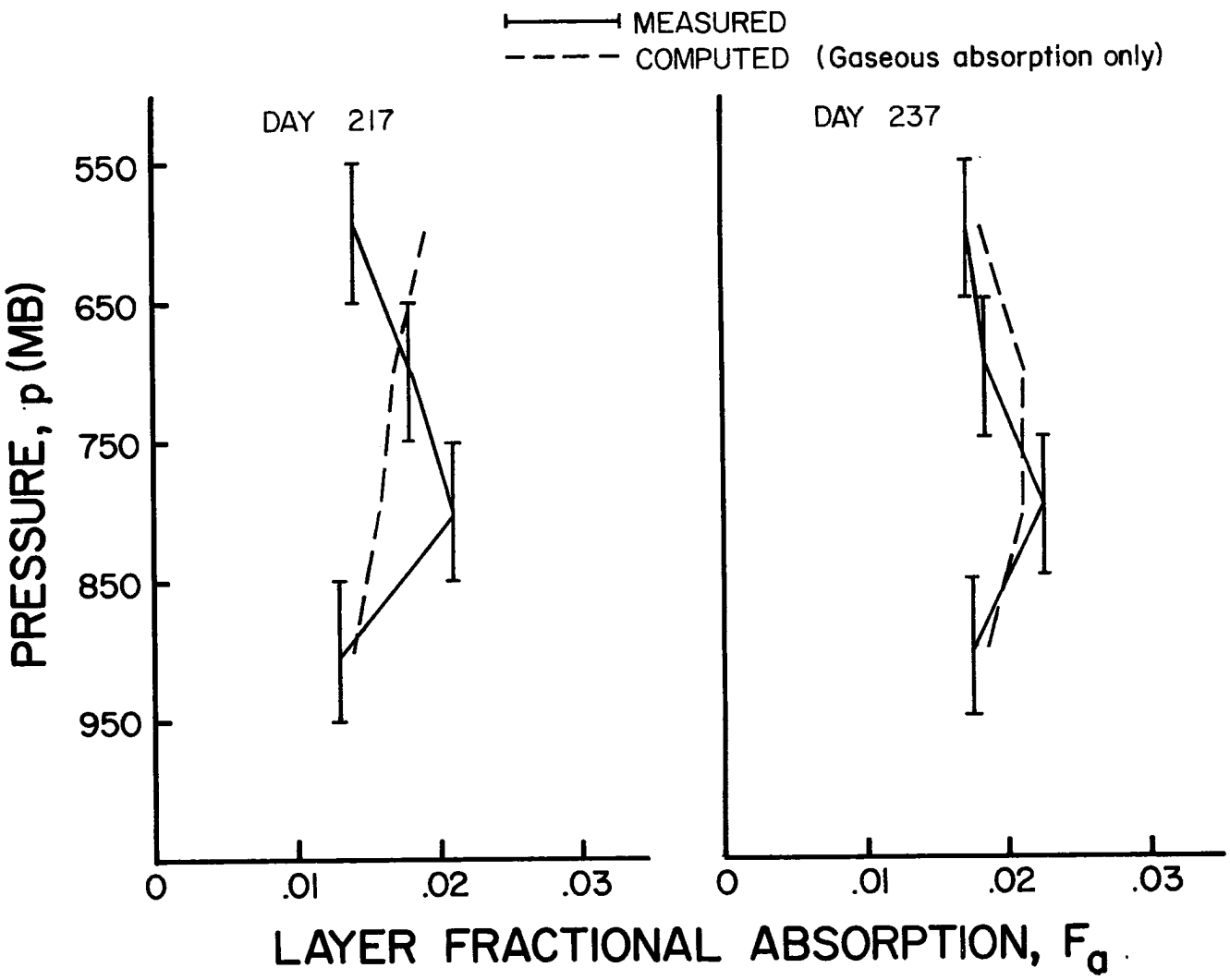

Figure 10. Fractional absorption values for 100 mb layers for dust-free days for measured data and for model-derived data for H_2O, CO_2 and O_3 absorption only.

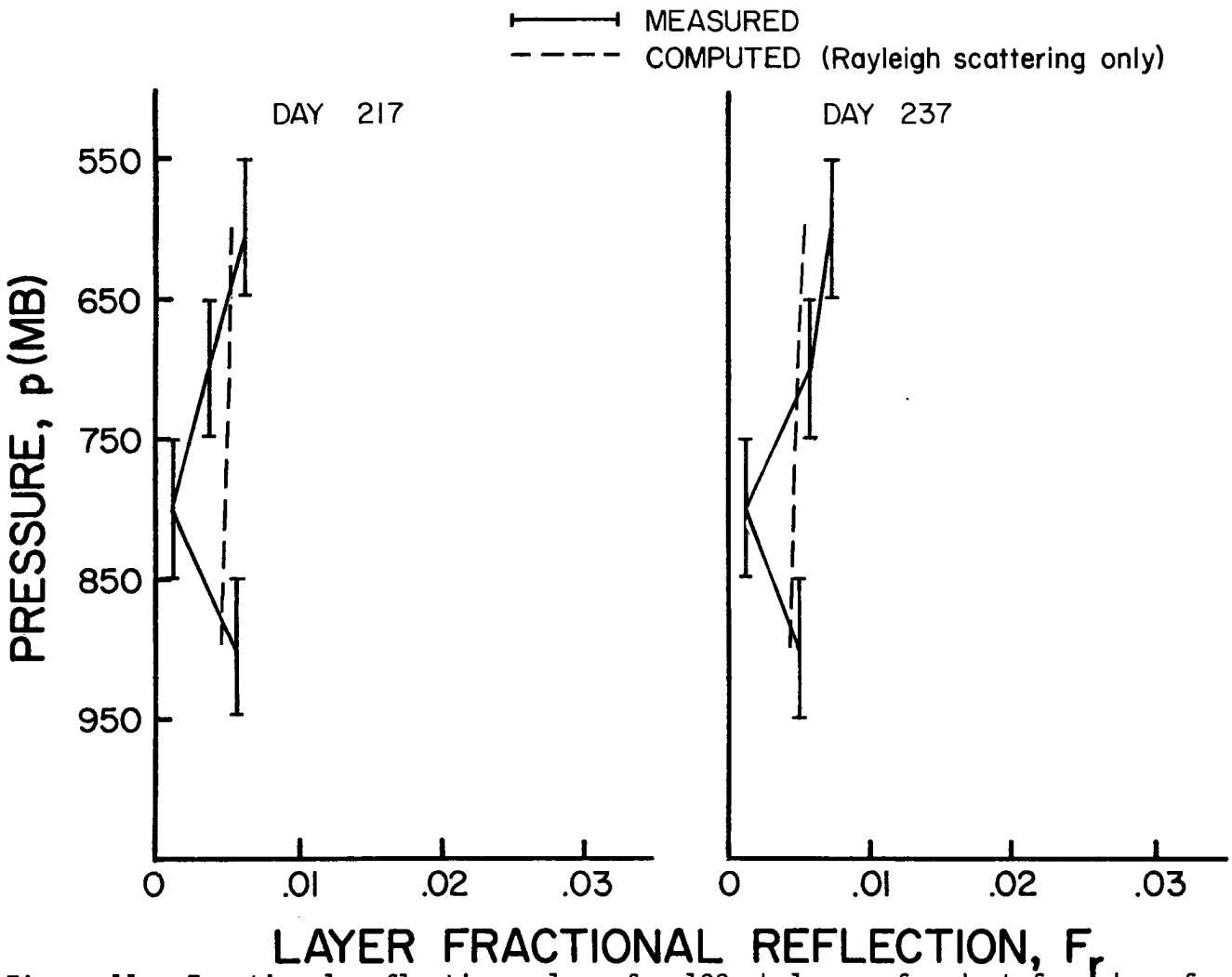

Figure 11. Fractional reflection values for 100 mb layers for dust-free days for measured data and for model-derived data for Rayleigh scattering only.

5.1.2 Infrared parameters

To calculate cooling rates for comparison with observed cooling rates the IRADLON values for L↓ (L↑) at the highest (lowest) flight levels must be equivalenced with the measured values in the same manner used for the emissivity comparisons. The flux profiles for day 237 which result from this equalization are displayed with the measured irradiances in Figure 12. The corresponding cooling rate comparisons are shown in the left half of Figure 9. There appears to be fairly close agreement above 750 mb, but below this level the comparability of the cooling rates decrease due to the larger differences in the downward fluxes. Above 750 mb the average difference in heating rates for a 200 mb layer is approximately 10^{-3}°C hr^{-1}, while below it exceeds .04°C hr^{-1}. For the total atmosphere this difference is .02°C hr^{-1}, only slightly greater than the previously estimated expected error.

The SDL emissivities computed from the observed and calculated flux data for day 237 show nearly the same differences that were assessed earlier. $\Delta\varepsilon^{*}\downarrow$ is approximately 10% of $\varepsilon^{*}\downarrow_{g}$, while $\Delta\varepsilon^{*}\uparrow$ is almost 9% of $\varepsilon^{*}\uparrow_{g}$. These values are equal to or less than the estimates given in 4.3.2 for total error between a calculated and observed clear sky case.

However, a new approximation of the expected errors in cooling rates must be made in light of the errors calculated in this section. Thus, any divergence between the observed and computed cooling rates which exceeds 0.02°C hr^{-1} per 100 mb may be attributed to the effects of dust. Unfortunately, no IR data are available for day 217, therefore no further verification of the magnitude of the uncertainties may

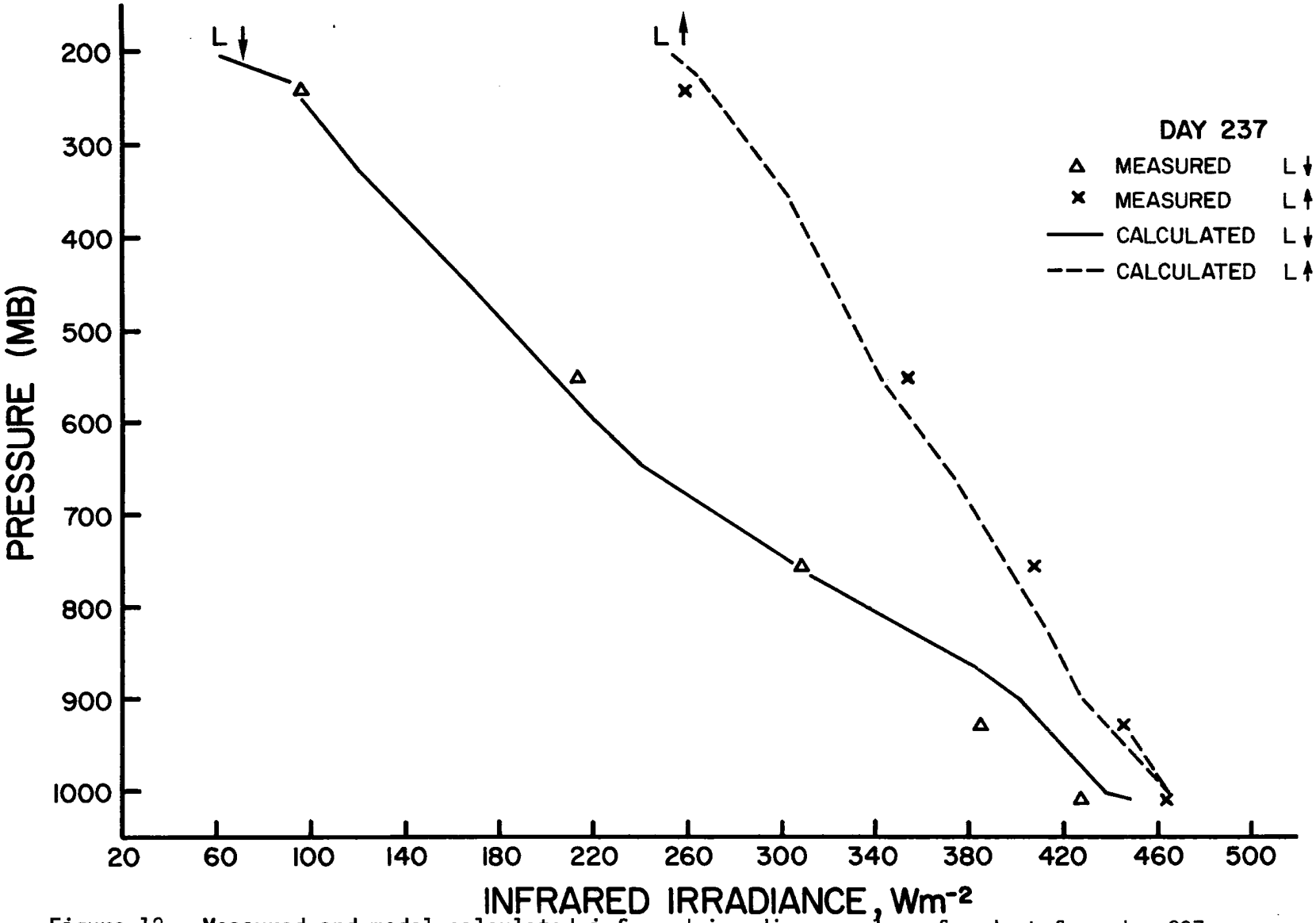

Figure 12. Measured and model-calculated infrared irradiance values for dust-free day 237.

be made. But the precisions noted above do provide an indication of the noise level in the longwave analysis.

5.2 Dust cases

Irradiance data taken on days described as moderately or extremely dusty are treated in the same manner as the dust-free cases to determine the magnitude of the effects of the Saharan dust on radiative parameters and fluxes.

5.2.1 Shortwave flux profiles

Normalized solar flux data and IRADSO2 computed irradiance profiles are displayed in Figures 13-16 for days 211, 229L, 229S, and 254. The earth-atmosphere albedo, α, which was found at the lowest flight level and used in the computations is given in these figures for each day. It may be seen that the measured and observed profiles almost converge between 500-600 mb for each case. It was decided that 550 mb would be considered as the top of the dust layers for comparison purposes since the calculated and measured profiles are nearly equal at this level.

The slope of $H\downarrow$ vs. p may be used to infer the approximate location of the most optically active dust. By comparing the slope, $\frac{\Delta H\downarrow}{\Delta p}$, for each diagram with the observers' notes (Appendix A) a correlation between $\frac{\Delta H\downarrow}{\Delta p}$ and the observer's description of the dust layer is found.

For example, on day 211 a heavy dust layer is described as existing approximately between 6,000 and 13,000 feet with low horizontal visibility at 10,000 feet. In Figure 13 the slope of the measured $H\downarrow$ curve is greatest between 700 and 850 mb. Above 700 mb $\frac{\Delta H\downarrow}{\Delta p}$ is greater than the calculated value but below 850 the values are nearly equal corresponding to a layer with no visible dust. On day 254 (Figure 16) the

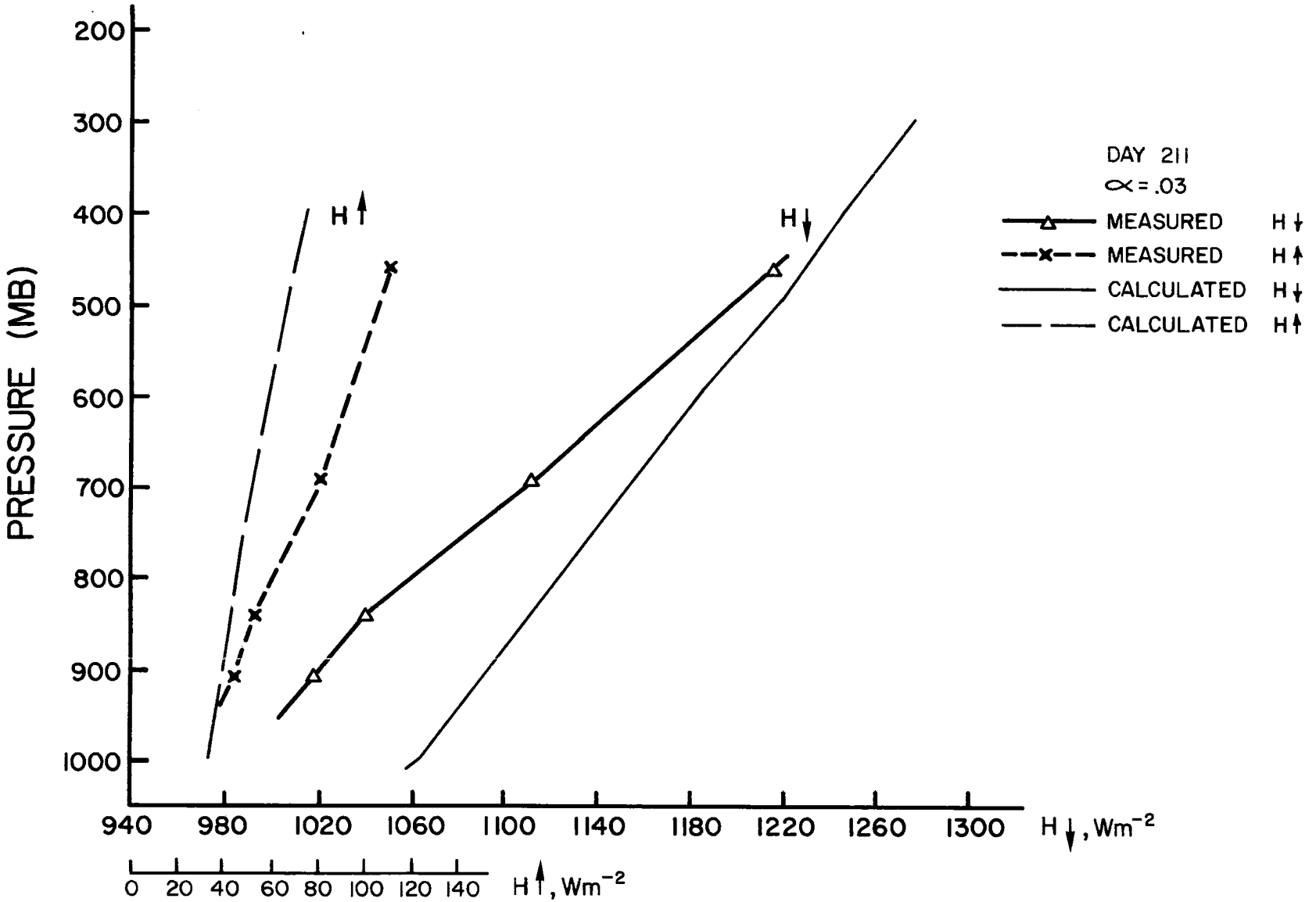

Figure 13. Measured and model-computed shortwave irradiance profiles for dusty day 211.

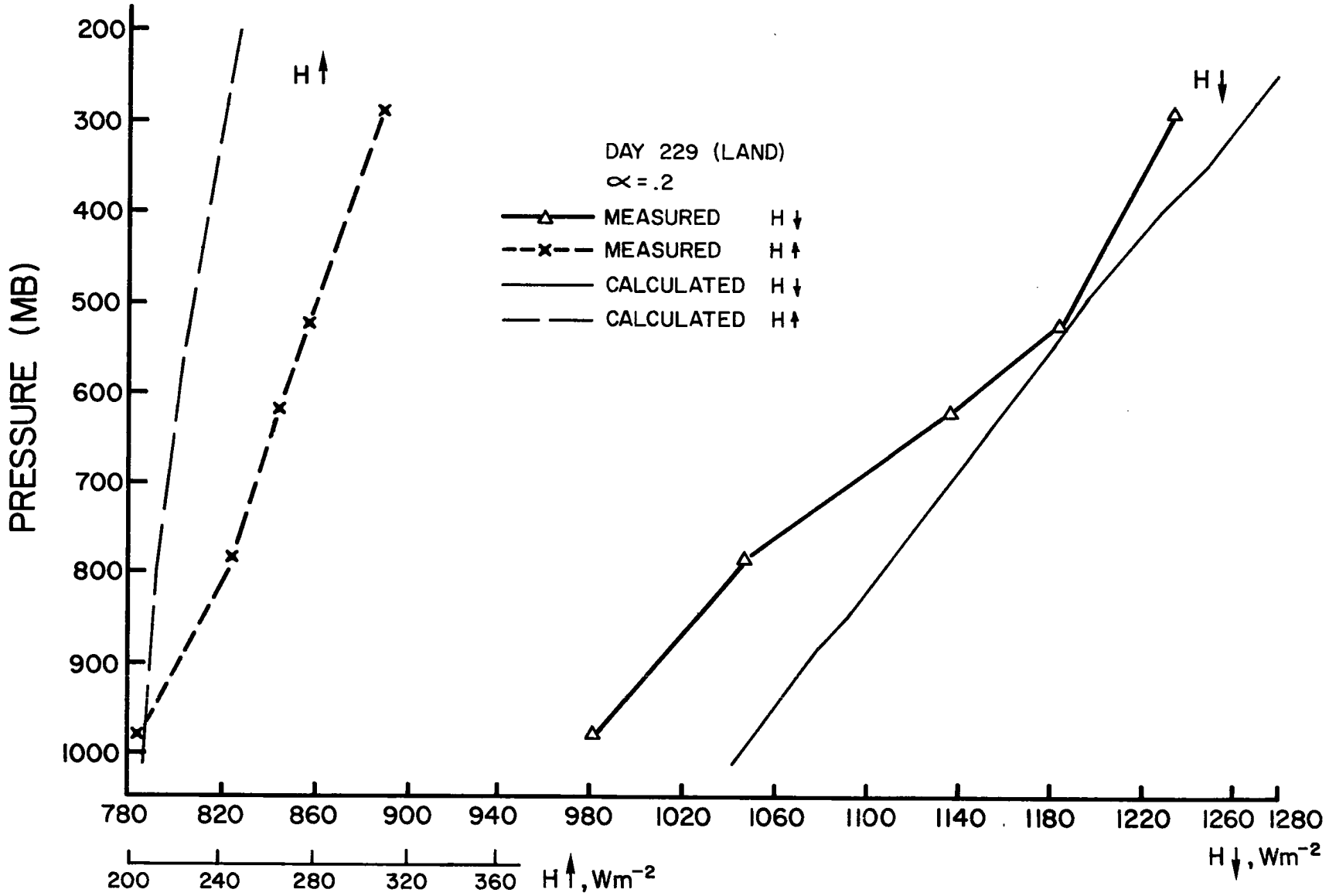

Figure 14. Measured and model-computed shortwave irradiance profiles for dusty day 229 over land.

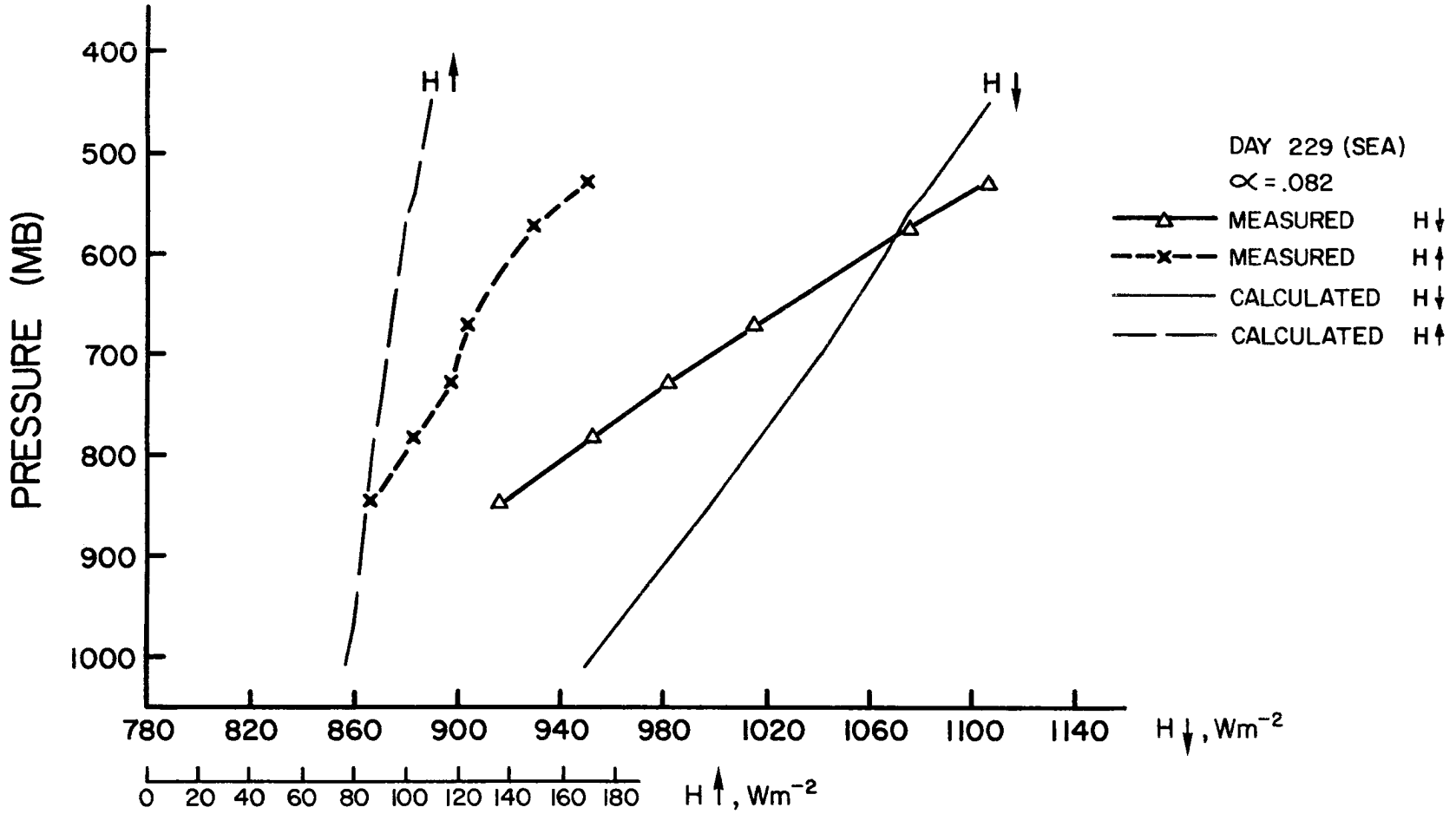

Figure 15. Measured and model-computed shortwave irradiance profiles for dusty day 229 over the Atlantic Ocean.

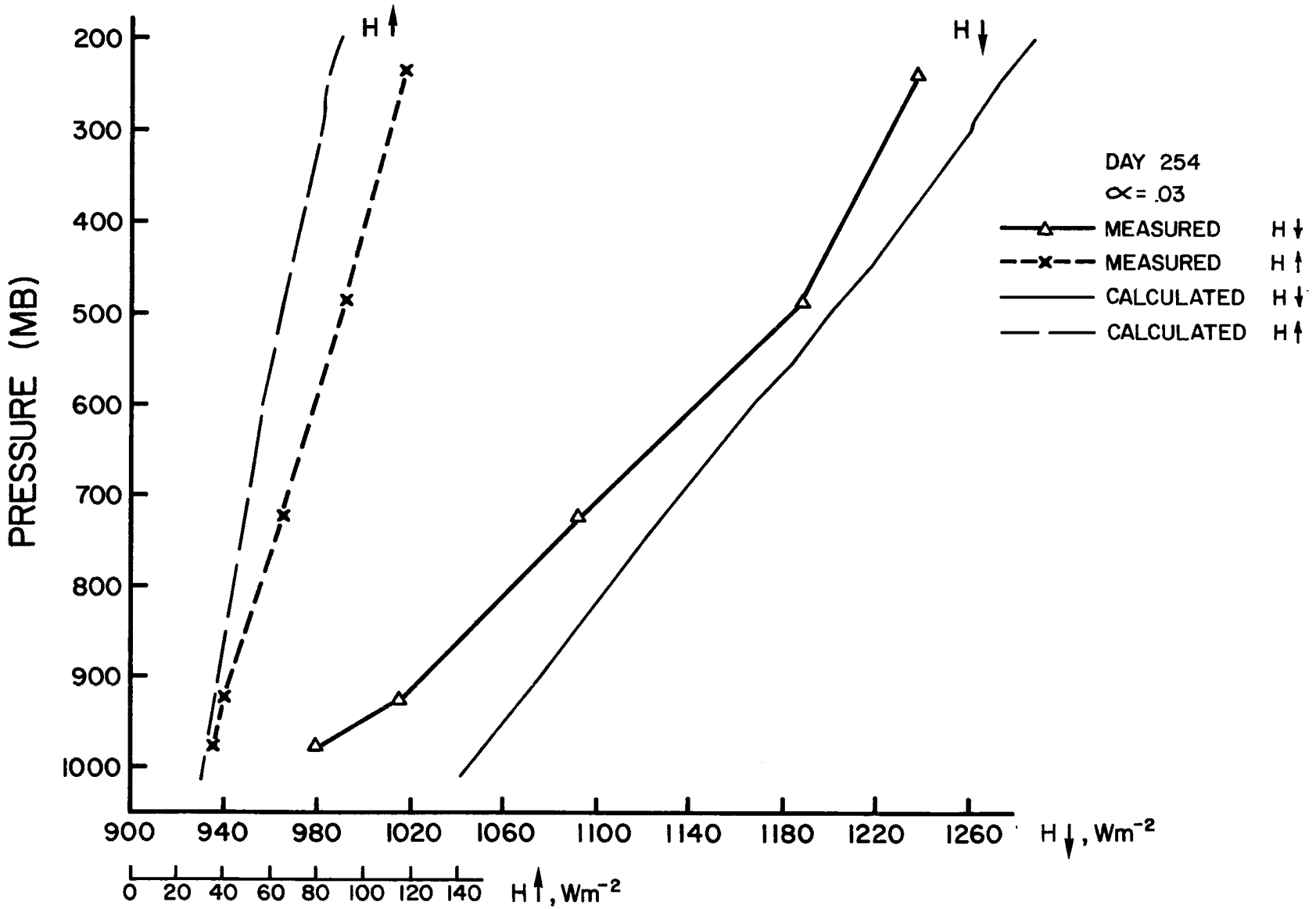

Figure 16. Measured and model-computed shortwave irradiance profiles for moderately dusty day 254.

value of $\frac{\Delta H\downarrow}{\Delta p}$ gradually increases with increasing pressure with the greatest value being located between 925 and 985 mb. The dust is described as being confined to the lower layers with a top at 15,000 feet. Similar correlations may be made for the other days used in this analysis. An analagous correspondence between $\frac{\Delta H\uparrow}{\Delta p}$ and the observers' notes is not detectable. Although actual concentrations are never measured to verify the observations, $\frac{\Delta H\downarrow}{\Delta p}$ may still be used to indicate at a glance the approximate location of the most optically active dust concentrations.

5.2.2 Fractional absorption and reflection

Values for fractional absorption and reflection for the 550-950 mb layer, F_{ad} and F_{rd}, which are due to the presence of dust are listed in Table III for all data sets employed in this analysis. The ratios of absorptance to reflectance, dust absorptivity to total calculated absorptivity, and dust reflectivity to total calculated reflectivity as well as percent increase in extinction are also presented in this table.

From column 3 it may be seen that the absorptance to reflectance ratio, R_{ar}, is less than 100% for all of the dust days considered.

Of the four flights described as extremely dusty only one showed an increase in absorption which exceeded the increase for day 254, a "moderately" dusty day. However, all four days with heavy dust showed increases in reflection which surpassed the dust reflectivity on day 254. For all five "dust" flights the average increase in total atmospheric absorption which results from the presence of aerosols is .016 or 9%. The average gain in reflectivity, though, is roughly twice this amount. The portion of the solar beam which is reflected by dust only

Julian Day #	F_{ad}	F_{rd}	Dust absorptance to reflectance ratio	% increase in total atmospheric absorption	% increase in total atmospheric reflection	% increase in total atmospheric extinction	Total Dust Extinction Wm^{-2}
211	.011	.027	40.7	7.0	46.6	17.8	51.3
212	.011	.019	57.9	6.3	32.6	12.6	39.3
217	-.001	-.003	33.3	-0.6	5.6	1.7	5.4
*229S	.034	.050	68.0	18.9	89.9	21.6	103.8
229L	.008	.043	18.6	4.3	83.0	35.6	68.6
237	-.001	.001	-100.	-0.2	0.7	0.0	0.0
254	.015	.016	93.7	8.8	27.4	13.5	40.9

*Figures here are for the layer from 850-550 mb only.

Table III. Shortwave radiative parameters for 950-550 mb layer for various days during the GATE.

for these five days is 3.1% in the mean. This converts to an average increase in reflectivity of 56% over the purely gaseous atmosphere. In terms of the partitioning of solar energy the Saharan dust is more effective in scattering than in absorbing.

On the average the airborne Saharan dust raises the total atmospheric extinction by 20% or 61 Wm^{-2}. This translates to an average decrease of 6% in the energy reaching the surface. However, this depletion of available radiative energy at the surface may range from 4 to 10% according to Table III. The smallest increase in absorption is found over land on flight 229L, while the greatest enhancement of absorption takes place on the same day over the sea on flight 229S. This smaller increase in absorptivity due to the dust over land may result, in part, from the effects of a higher albedo. Because the amount of energy absorbed in a layer depends on the total amount of energy available to the atmospheric layer or on the path length of the radiation, more energy should be absorbed in a given layer over the surface with the higher albedo. This concept may be verified using irradiance data from flights 229S and 229L. As a result of the higher surface albedo 10% more energy - relative to the adjusted solar constants - is available for absorption in the 550-850 mb layer on 229L. From the model calculations performed for these two flights for dust-free conditions (dashed curves, Figure 17), it is found that the fractional absorption in the same layer is exactly 10% (.005) higher on 229L, although the moisture profiles for the two flights do not differ significantly.

Conversely, it may be seen in Figure 17 that the total dust-caused increase (solid lines) in fractional absorption in the 550-850 mb layer is .005 greater on 229S than on 229L. Figure 17 shows that

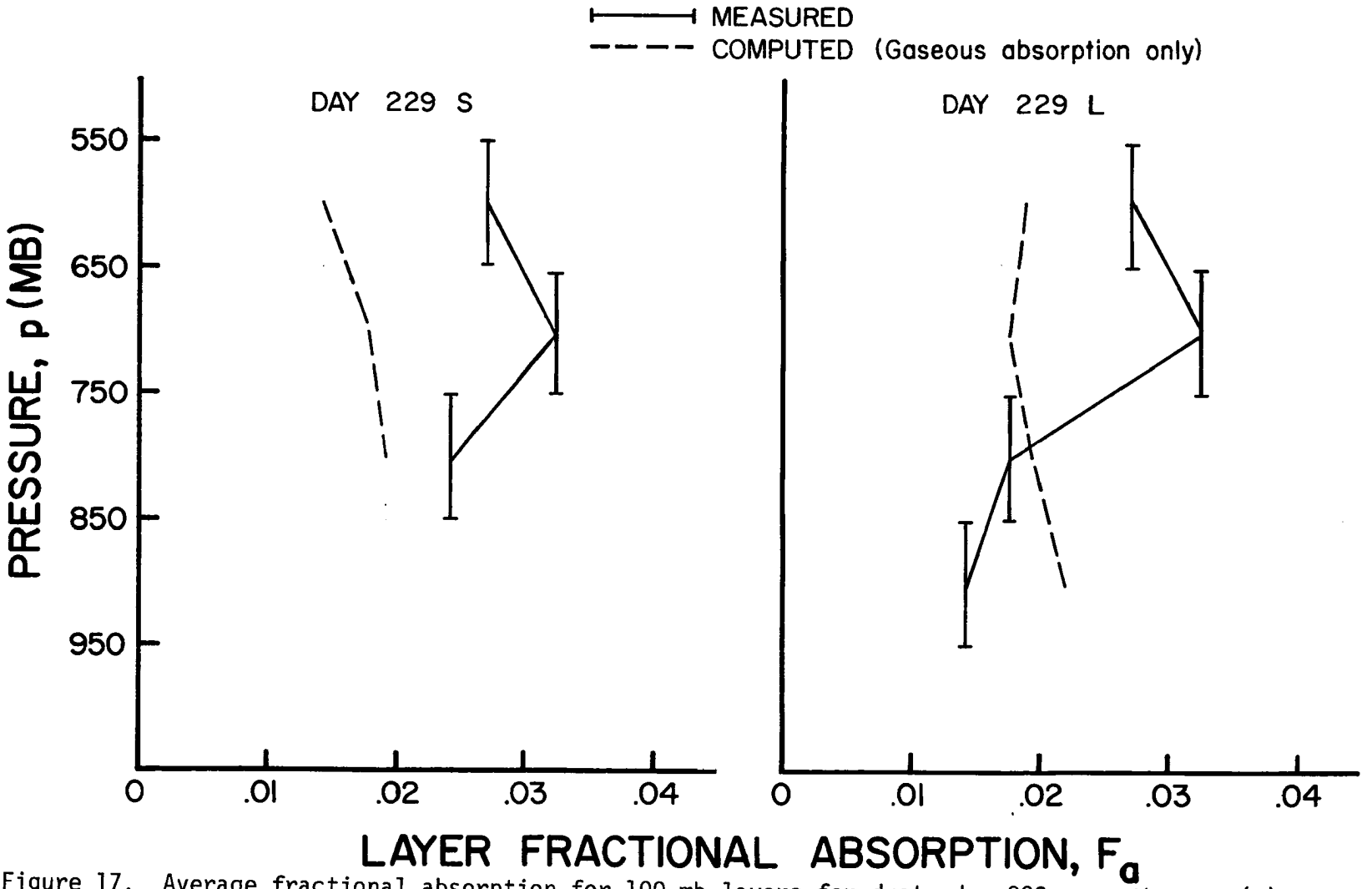

Figure 17. Average fractional absorption for 100 mb layers for dusty day 229 over the sea (S) and over land (L).

the absorptivity due to the dust is nearly equal for both flights in the upper half of the SDL. But in the lower half the inequality becomes evident. This tendency toward increased absorptivity in the upper layers of the SDL and toward decreased absorptivity in the lower layers seen in Figure 17 is also apparent in Figure 18.

This difference between dust effects over land and sea may be explained if it is assumed that the centers of the gaseous absorption bands become nearly saturated over the surface with the higher albedo, then any further enhancement of gaseous absorption resulting from increased path lengths become increasingly difficult to achieve since the absorptivities are so much lower in the band wings than in the centers. So the increase in gaseous absorption which could be realized by adding scattering dust to the atmosphere over a surface of this type would be much less than the gaseous absorption gained over a surface which did not cause saturation at the centers of the absorbing bands. These differences in dust absorptivity over land and sea may also result from differences in dust concentrations over the two surfaces.

The 100 mb resolution of the SDL reflectivity reveals a different structure for the scattering effects of the dust, however. From Figures 19 and 20 it is obvious that the dust increases shortwave scattering throughout the layer. On several days, 211, 212, and 229L, the largest increases in reflectivity occur in the lower half of the SDL while the greatest increases in absorptivity occur above this highly reflective layer. However, some of the extra reflectivity in these layers may result from trade cumuli embedded in the layer.

In general the Saharan dust layer does tend to decrease the irradiance stream reaching the surface by 6% over that expected from

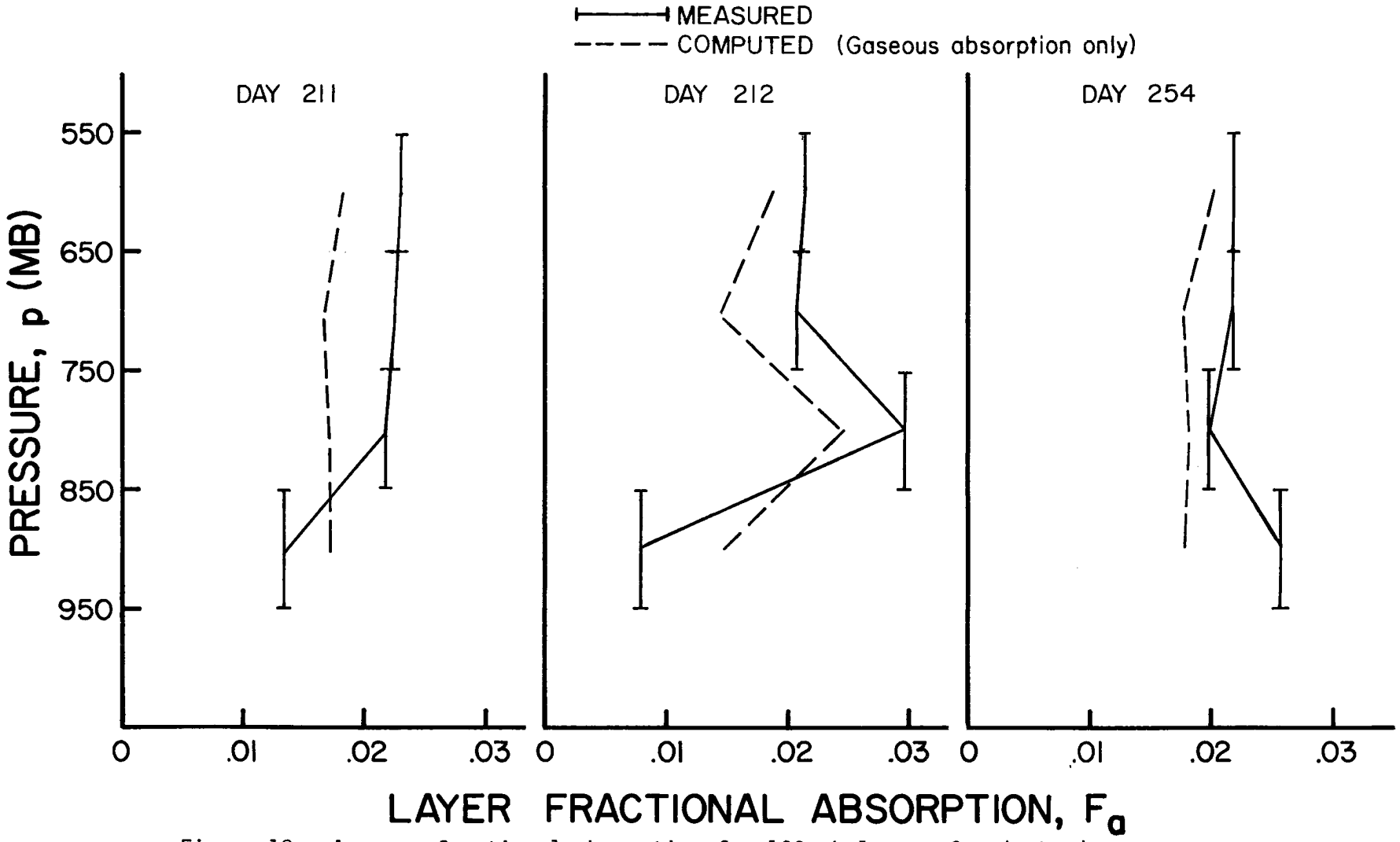

Figure 18. Average fractional absorption for 100 mb layers for dusty days.

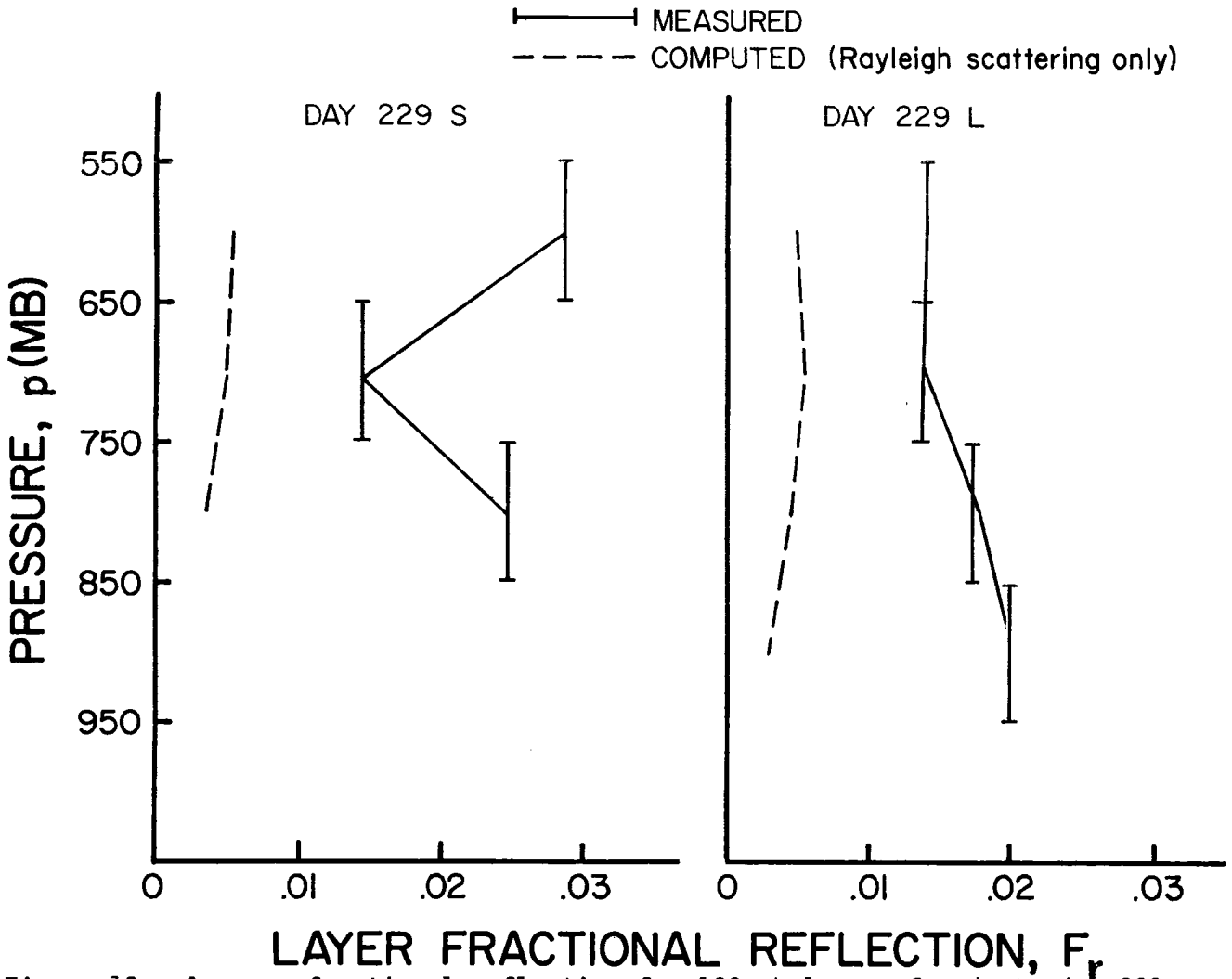

Figure 19. Average fractional reflection for 100 mb layers for dusty day 229 over the sea (S) and over land (L).

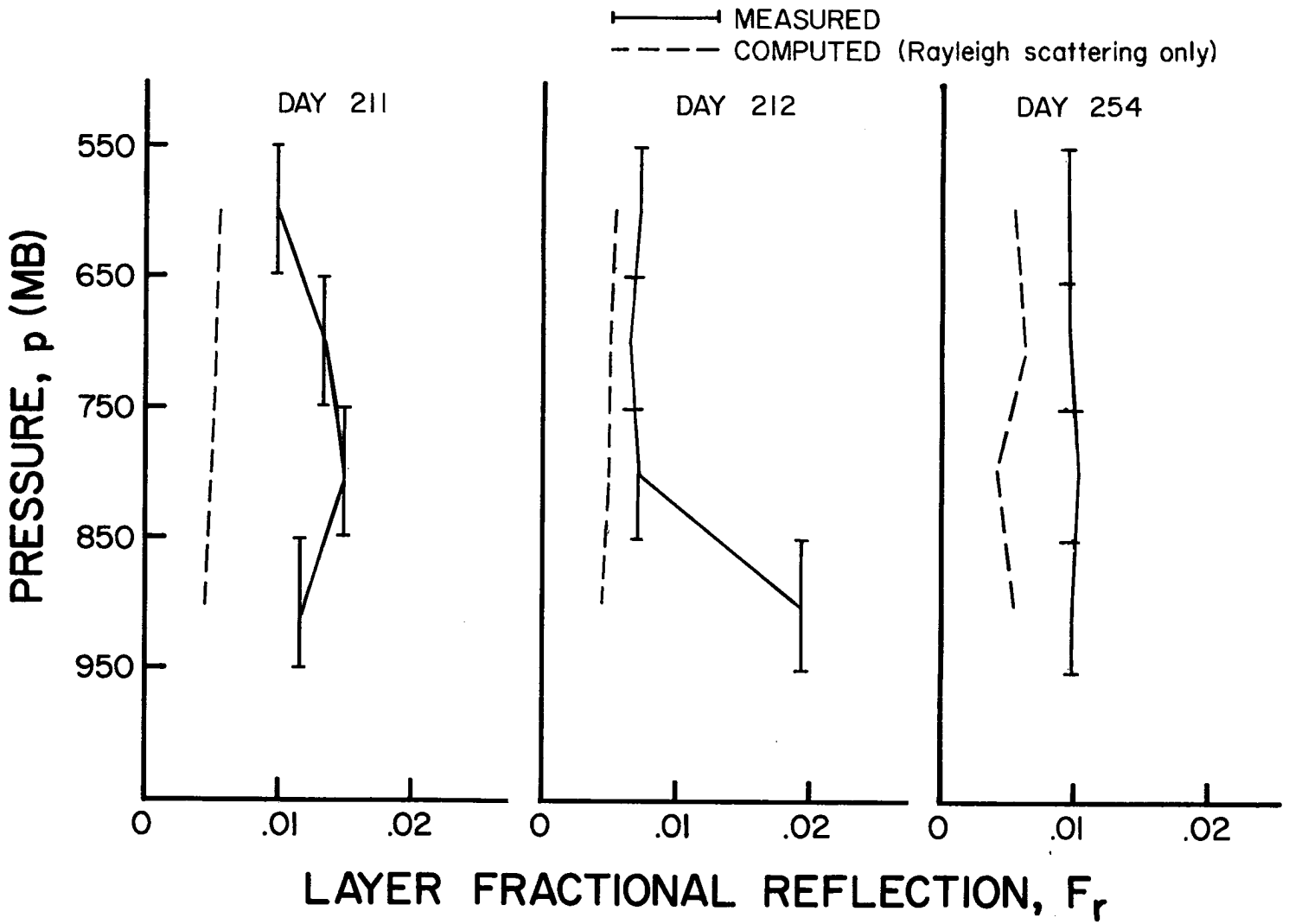

Figure 20. Average fractional reflection for 100 mb layers for dusty days.

calculations of a completely gaseous atmosphere. One third of this extinguished flux is absorbed by the atmospheric components while the remaining two thirds are reflected back to the upper atmosphere. The dust, when present in the midsection of the troposphere, increases the heating rates in the middle levels while decreasing the values for the same parameters in lower layers of the troposphere. Absorptivity caused by dust, though never greater than 20% of the total absorption for a dust-free atmosphere, becomes significant when its distribution is considered.

5.2.3 Solar heating rates

The instantaneous heating rates found for day 211 are shown in Figure 21. The average heating rate for this day between 463 and 700 mb exceeds the computed value for the same layer by almost .03°C hr^{-1}. In the layer below, the measured value is greater by .02°C hr^{-1} while between 845 and 910 mb there is no difference. Based on the 4 Wm^{-2} estimate of flux error the dust appears to have the effect of increasing the heating rate by at least .025°C hr^{-1} in the top of the SDL and by at least .01°C hr^{-1} in the middle levels. There seems to be no increase in heating in the bottom of the dust layer.

The heating rates for day 212 shown in Figure 22 reveal the same lack of apparent dust effect in the lower part of the SDL. In fact a decrease of .02°C hr^{-1} from the computed heating rate is found in this area. The top of the dust layer also reveals no dust effects while an increase of .06°C hr^{-1} over 100 mb is found in the midsection of the aerosol layer. These differences in heating rates between days 211

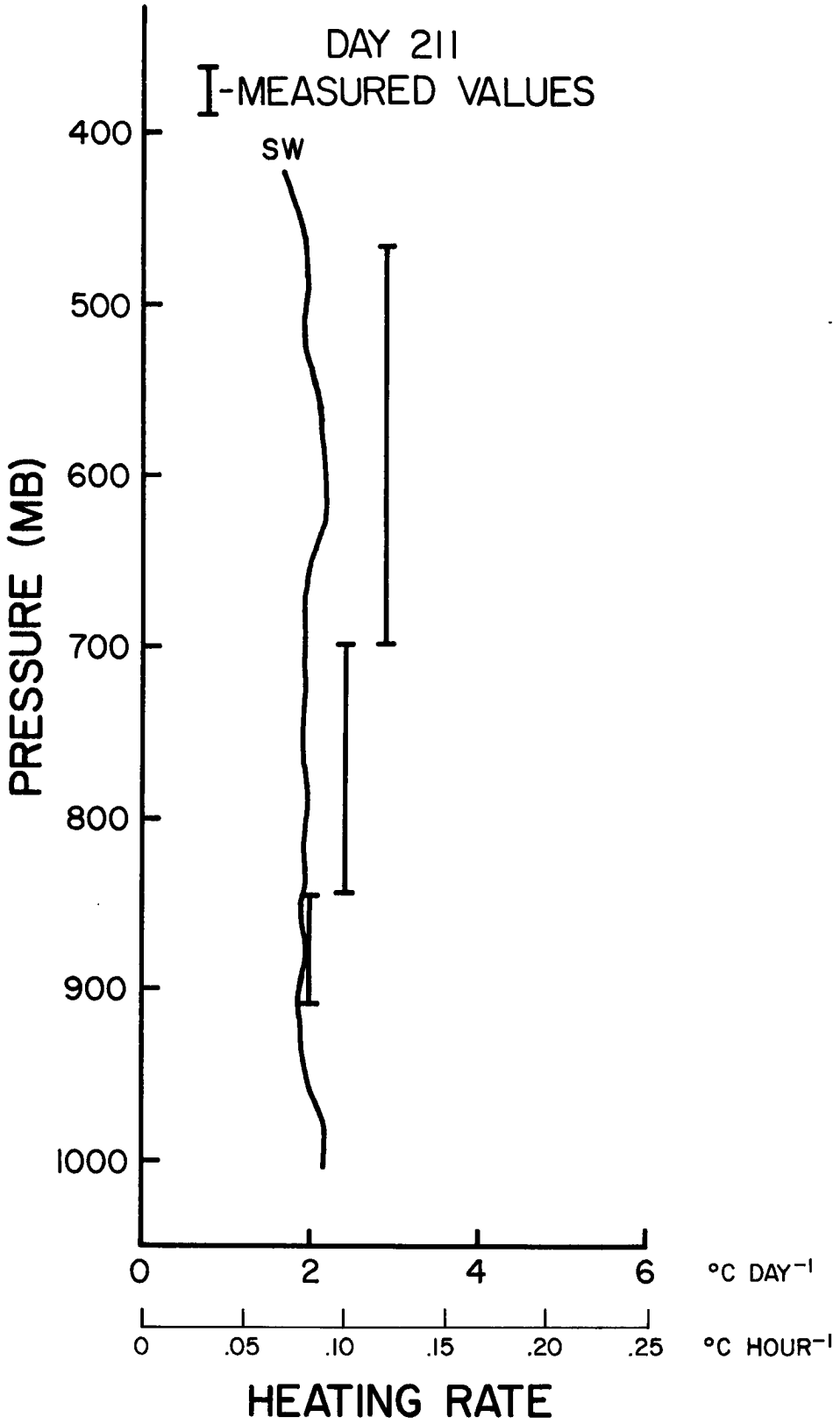

Figure 21. Model-calculated and observed heating rates for dusty day 211.

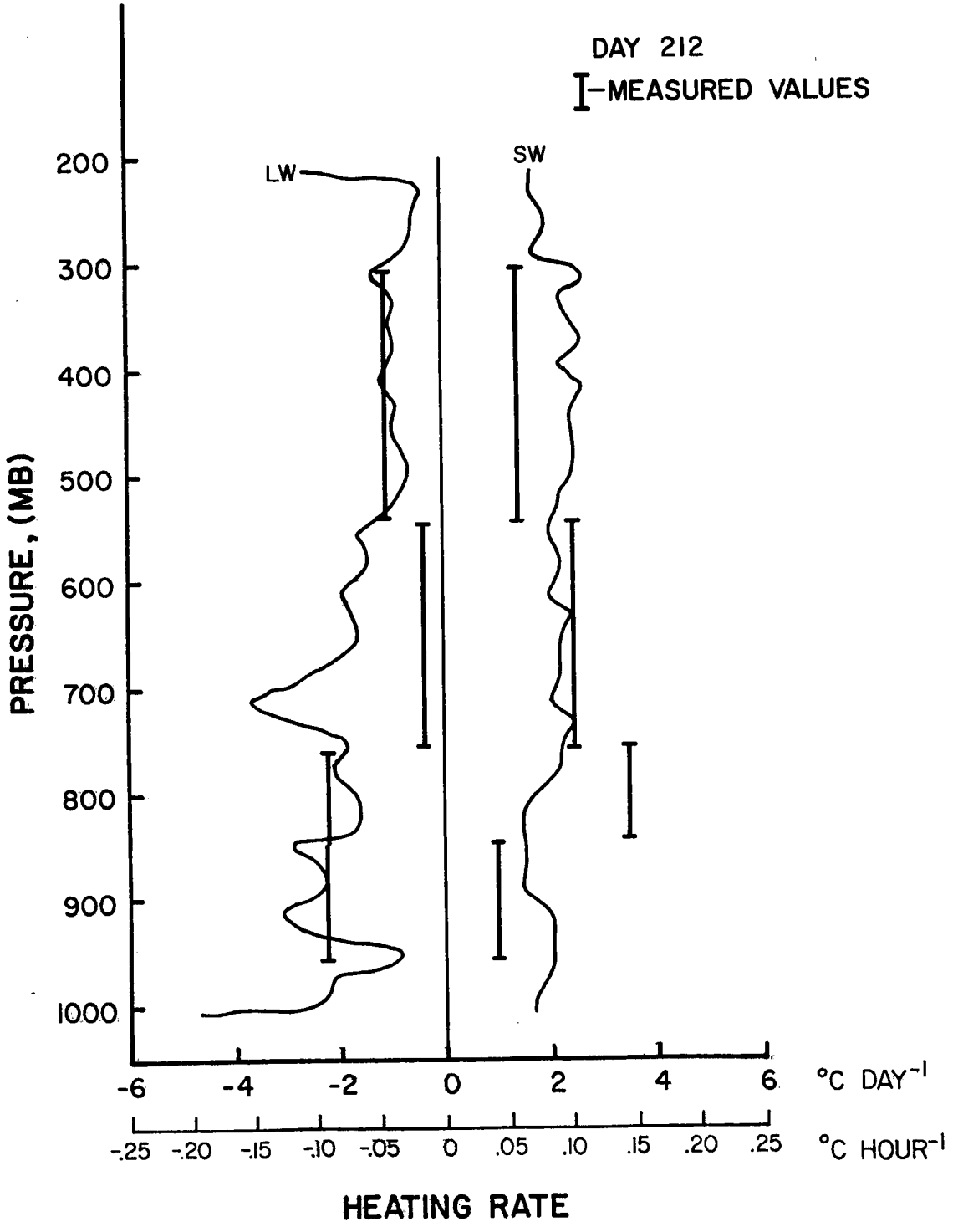

Figure 22. Measured and model-computed heating rates for absorption in both the longwave (LW) and shortwave (SW) spectral regions for dusty day 212.

and 212 probably result from changes in the structure of the Saharan dust layer.

Heating rate data for 229L and 229S, depicted in Figures 23 and 24 respectively, show most clearly and consistently the effects of the dust on heating rates. Maximum heating occurs between 600 and 800 mb for both flight data sets. The heating rates at the top of the SDL although slightly less than the maxima are still significantly greater than the computed values. The profile in Figure 23 reveals the same decrease in heating rate in the lower layer that was seen in Figure 22. From both Figures 23 and 24 it may be seen that an increase of at least .06°C hr^{-1} for a 100 mb layer may be expected in the presence of dust. Another effect of the dust is the reshaping of the heating profile. The maximum heating rates evidently correspond to the layers containing the most visible dust if the observers' notes are consulted.

The increases in heating rates due to dust do not appear to be as significant on day 254 (Fig. 25) as on other days. But this day is described as being moderately dusty. There is a consistent difference in the heating rates between the computed and measured values below 500 mb but the presence of the dust does not increase the heating rates by more than .015°C hr^{-1} in the upper and middle layers of the SDL. However, in the lower layers which contain the largest dust concentrations (Appendix A) the heating rate over a 50 mb layer exceeds the expected value for a clear sky by more than .10°C hr^{-1}. Some of this apparent increase may be the result of cloud contaminated flux data but it is likely that some is the result of dust interaction. Again there is good correlation between the maximum heating rate and the layer reported as containing the most visible dust.

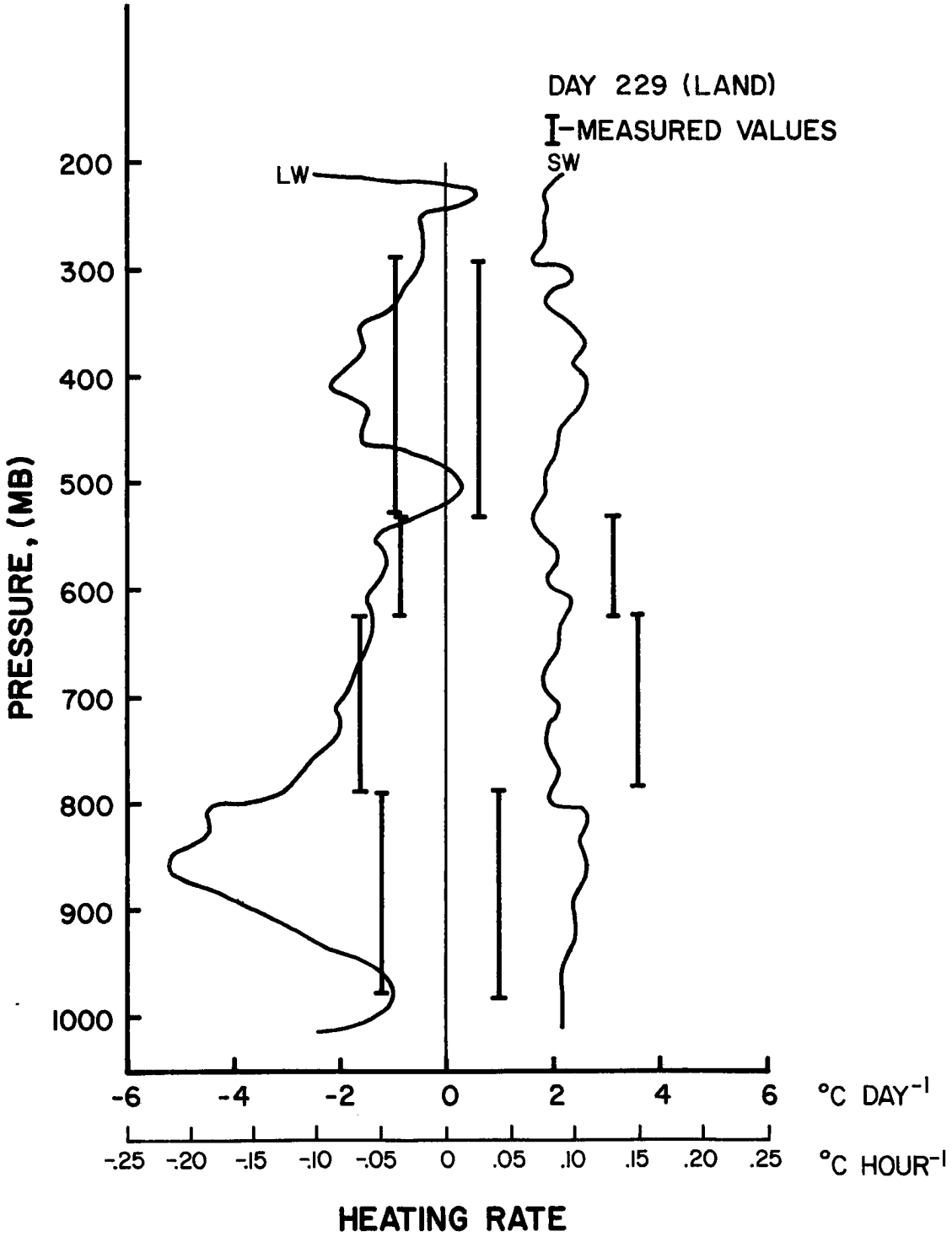

Figure 23. Measured and model-computed heating rates for absorption in both the longwave (LW) and shortwave (SW) spectral regions for dusty day 229 over land.

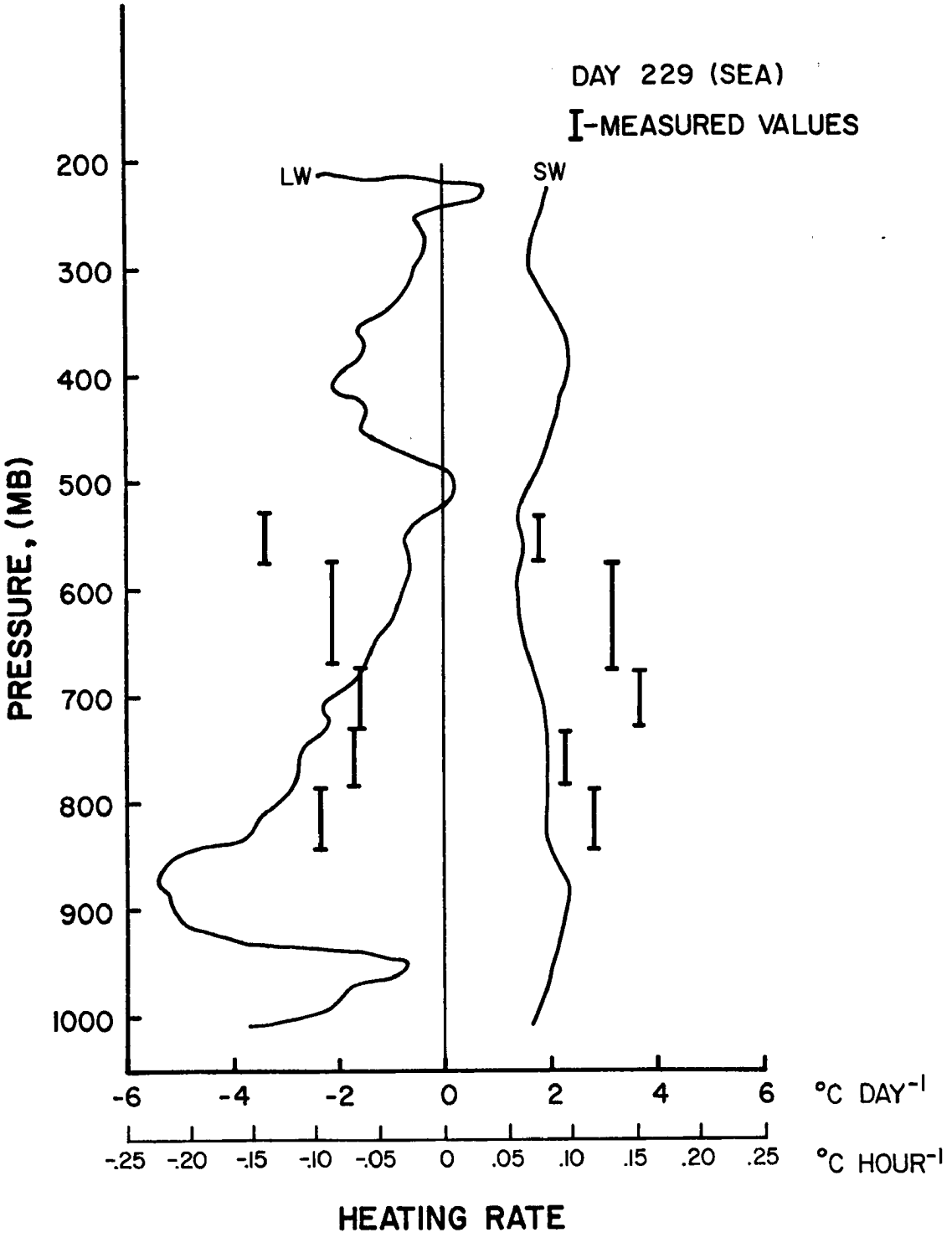

Figure 24. Measured and model-computed heating rates for absorption in both the longwave (LW) and shortwave (SW) spectral regions for dusty day 229 over the sea.

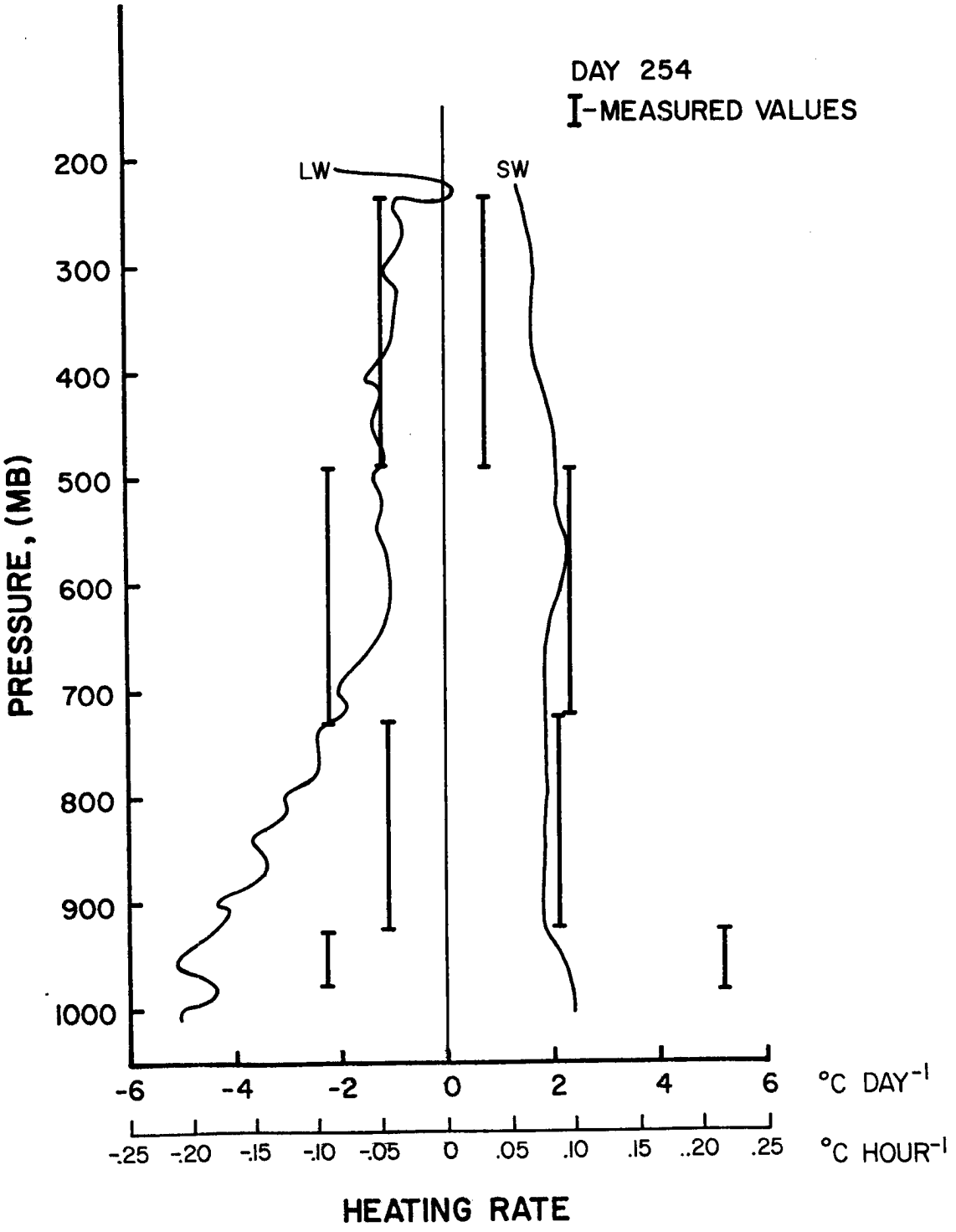

Figure 25. Measured and model-computed heating rates for absorption in the longwave (LW) and shortwave (SW) spectral regions for moderately dusty day 254.

5.2.4 Longwave flux profiles

Figures 26 and 27 depict the infrared irradiance profiles for two dusty days, 229L and 254, respectively. It appears that the agreement between the model and the measurements is good in the upper levels for $L\downarrow$ on day 229L but this conformity ends at the lowest level. This is also evident in Figure 12 for flight 237. These large differences, $> 20\ Wm^{-2}$, are partially a result of the inability of the model to correctly depict fluxes in the vicinity of a temperature inversion with only low resolution temperature and moisture data for input. On day 254 there is still some discrepancy in values of $L\downarrow$ at lower levels but the most significant difference is an increase of more than $40\ Wm^{-2}$ at 725 mb. This may indicate the presence of a cloud overhead. However, clouds are not the explanation for the large divergence between $L\downarrow$ and $L\downarrow_g$ in the lower layers on the other days. The normal response of $L\downarrow$ to a cloud above would be an increase in its value.

It appears that in general the model tends to underestimate $L\uparrow$ in the lower layers and to overestimate $L\uparrow$ in the upper layers for both dusty and dust-free days. The overall agreement for $L\uparrow$ and $L\uparrow_g$ is on the average as good as that for $L\downarrow$ and $L\downarrow_g$, but the values for $\Delta L\uparrow$ never exceed $20\ Wm^{-2}$.

5.2.5 Effective emissivities

Effective emissivities for both the upward and downward directions were calculated for days 229S, 229L, and 254 according to the methods described in section 4.3. The results are presented in Table IV with the parameters found for day 237.

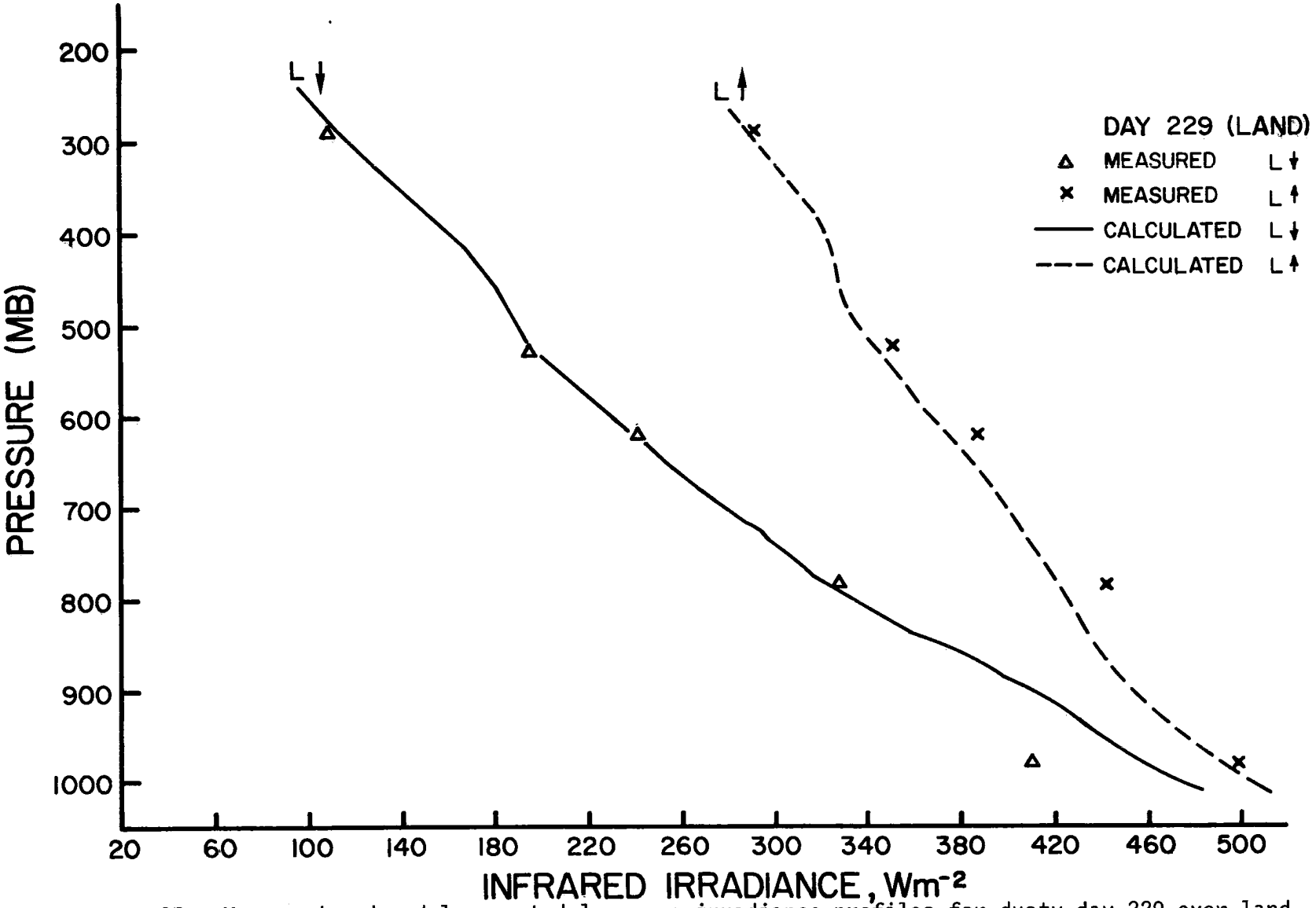

Figure 26. Measured and model-computed longwave irradiance profiles for dusty day 229 over land.

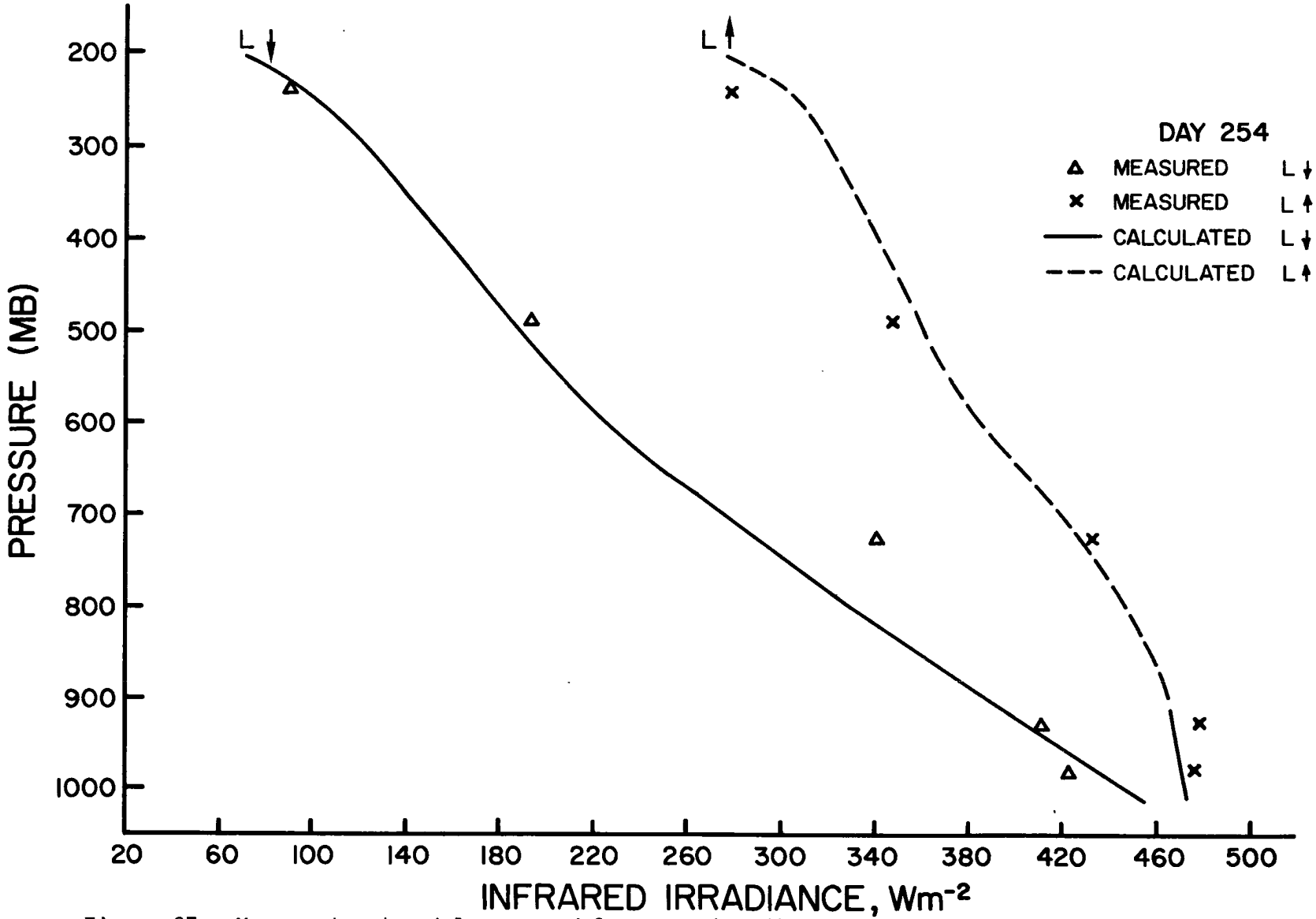

Figure 27. Measured and model-computed longwave irradiance profiles for moderately dusty day 254.

Julian Day #	$\varepsilon^{*\uparrow}$	$\varepsilon^{*\uparrow}_g$	$\Delta\varepsilon^{*\uparrow}$	$\varepsilon^{*\downarrow}$	$\varepsilon^{*\downarrow}_g$	$\Delta\varepsilon^{*\downarrow}$
229S	.657	.597	.060	.668	.653	.015
229L	.704	.744	-.040	.772	.921	-.149
237	.663	.726	-.063	.869	.967	-.098
254	.789	.808	-.019	.663	.644	.019

Table IV. Effective emissivities for the 550 - 950 mb layer calculated from measured and computed flux data. The differences between the two types are also listed.

Using the error estimates derived in section 5.1.2 it becomes evident that there is no important or consistent change in the layer emissivity resulting from the presence of dust. The average value of $\Delta\varepsilon^{*\uparrow}$ is only 5.6% of $\varepsilon^{*\uparrow}_g$ for all three dusty days and not all of the individual values are of the same sign.

Likewise, the average value of $\Delta\varepsilon^{*\downarrow}$ for the three days is 8.3% of $\varepsilon^{*\downarrow}_g$. Only one value of $\Delta\varepsilon^{*\downarrow}$, on day 229L, exceeds the previously established noise level of 10%. However, its sign is the opposite of those values of $\Delta\varepsilon^{*\downarrow}$ for the other two days.

In light of the inconsistent and insignificant differences found for the calculated and observed parameters it is reasonable to conclude that the aerosols in the Saharan dust layer are not significant contributors to the infrared radiation budget at the 10% level on the days studied. There may be some interaction between the dust and longwave radiation but its magnitude is not great enough to be resolved by the methods of this analysis.

5.2.6 Longwave cooling rates

The cooling rates for the three dusty days are displayed in the left halves of Figures 23, 24, and 25. In Figure 23 the effects of the 40 Wm^{-2} discrepancy in L↓ for flight 229L at 985 mb are revealed in a difference of at least .10°C hr^{-1} between the computed and measured cooling rates for the lowest layer. There is close agreement between the model and the observations above this level suggesting that the dust effect on the longwave heating rate is negligible.

On the other hand the measured cooling rates represented in Figure 24 show an average increase of .07°C hr^{-1} over the computed values at the top of the SDL, while in the mid-levels there is a decrease of .04°C hr^{-1}. A smaller increase in cooling rates at the top of the SDL is revealed in Figure 25 for day 254. At the bottom of the dust layer there is apparently some suppression of longwave cooling for this same day. Data for day 212 in Figure 22 show no difference in cooling rates in the lowest layers but it does reveal some decrease in cooling at the top of the Saharan dust layer.

Because the cooling rate profiles analyzed here show no consistent, significant differences between the measured and the observed values, except for some possible suppression of cooling in the lower layers, it is difficult to discern any real dust effect. If there were any measurable dust-caused change in the cooling rates it is reasonable to assume that it would be manifested in an increase in cooling at the top of the dust layer. However, data from only one flight clearly shows an increased radiative cooling, while data from the remaining flights reveal the opposite or no change at all. There is some evidence which

indicates that cooling may be suppressed in the lower half of the SDL but this too, is inconclusive based upon the limitations of the data.

6.0 CONCLUSIONS

The broadband radiative effects of Saharan dust aerosols in terms of several bulk parameters have been determined for five data sets taken in the summer of 1974 in a region northeast of the GATE A/B scale array. The differences between the radiative parameters derived from aircraft irradiance measurements and those same parameters derived from calculated dust-free irradiances have been defined as effects caused by the presence of the Saharan dust in the atmosphere.

It was found that the dust in the Saharan air layer may cause increases in fractional absorption from 4% to 19% and in atmospheric reflectivity from 25 to 90%. The maximum aerosol absorption generally occurs above the maximum particulate reflection. The increases in total extinction resulting from the presence of dust in the layer averages 20% (61 Wm^{-2}) of the expected clear sky value.

A significant effect of the presence of dust is a redistribution of the tropospheric heating rates. In general, the maximum absorption or heating occurs in the top levels of the dust layer. In the lower levels the heating rates generally decrease with decreasing height, so that in the lowest layers the clear sky heating rates exceed the measured values. From the results of this analysis it is evident that the primary radiative effects of Saharan dust occur in the shortwave spectral region which agrees with the findings of other researchers (Mani and Srinivasan, 1972; Paltridge and Platt, 1973; Liou and Sasamori, 1975). Although no effects of dust on layer emissivities could be resolved at the 10% level, there appears to be some suppression

of the infrared cooling rates in the Saharan air layer as a result of the presence of dust.

It is apparent from satellite photographs that the irradiance measurements used in this analysis were taken in locations which did not contain the highest concentrations of dust. So these results represent neither the maximum nor the minimum effects which may result from dust in the Saharan air layer. Nor do these results preclude any significant dust effect in the infrared spectrum. However, these data do tend to confirm the conclusion that Saharan dust outbreaks may be an important factor in the solar radiation budget of the GATE area.

REFERENCES

Ackerman, T.P., K. Liou, and C.B. Levoy, 1976. Infrared Radiative Transfer in Polluted Atmospheres. Journal of Applied Meteorology, 15, pp. 28-35.

Albrecht, B., M. Poellet, and S. K. Cox, 1974. Pyrgeometer Measurements from Aircraft. Review of Scientific Instruments, 45, pp. 33-38.

_____, and S. K. Cox, 1976 a. Radiation Data Reduction Procedures for Sabreliner, C-130, and DC-6 Aircraft during the GARP Atlantic Tropical Experiment. Colorado State University Atmospheric Science Paper No. 244, Ft. Collins, Colorado.

_____, and S. K. Cox, 1976 b. Pyrgeometer Data Reduction and Calibration Procedures. Colorado State University Atmospheric Science Paper No. 251, Fort Collins, Colorado.

Carlson, T. N., and J. M. Prospero, 1972. The Large-Scale Movement of Saharan Air Outbreaks over the Northern Equatorial Atlantic. Journal of Applied Meteorology, 11, pp. 283-297.

_____, J. M. Prospero, and K. J. Hanson, 1973. Attenuation of Solar Radiation by Windborne Dust off the West Coast of Africa. NOAA Technical Memorandum ERL WMPO-7.

_____, 1975. A Compilation of Solar Radiation Measurements Made on Sal, Cape Verde during GATE. U.S. NOAA GATE Office, Rockville, Maryland, NSF Grant GATE-6319.

_____, 1977. Personal Communication.

Charlson, R. J., and M. J. Pilat, 1969. Climate: The Influence of Aerosols. Journal of Applied Meteorology, 8, pp. 1001-1002.

Cox, S. K., 1969. Observational Evidence of Anomalous Infrared Cooling in a Clear Tropical Atmosphere. Journal of Atmospheric Sciences, 26, pp. 1347-1349.

_____, 1971. Observations of Cloud Infrared Effective Emissivity. Journal of Atmospheric Sciences, 33, pp. 287-289.

_____, 1973. Infrared Heating Caclulations with a Water Vapour Pressure Broadened Continuum. Quarterly Journal of the Royal Meteorological Society, 99, pp. 669-679.

_____, 1975. Relating Broadband Shortwave Irradiance Measurements to Radiation Properties of the Atmosphere. 2nd Conference on Atmospheric Radiation. Arlington, Virginia. Collection of Abstracts. pp. 235-240.

REFERENCES (Continued)

Cox, S. K., and H. Kraus, 1975. GATE Radiation Subprogram Field Phase Report. Colorado State University GATE Report, Fort Collins, Colorado.

_____, M. C. Polifka, K. Griffith, A. Rockwood, and D. Starr, 1976. Radiative Transfer Computational Routines for Atmospheric Science Applications. Colorado State University Atmospheric Science Research Report, Fort Collins, Colorado.

Eschelbach, G., and J. Gutenberg, 1972. The Influence of the Aerosol Particles on the Energy Balance of the Atmosphere in the Visible Range of the Solar Spectrum. Proceedings Intl. Radiation Symposium, Sendai, Japan.

Fischer, K and H. Grassl, 1975. Absorption by Airborne and Deposited Particles in the 8-13 Micrometer Range. Tellus, 5.

Griffith, K. T. and S. K. Cox, 1977. Infrared Radiative Properties of Tropical Cirrus Clouds Inferred from Broadband Measurements. Colorado State University Atmospheric Science Paper No. 269, Fort Collins, Colorado.

Idso, S. B., 1974. Thermal Blanketing: A Case for Aerosol-Induced Climatic Interaction. Science, 186, October 4, pp. 50-51.

Kondratyev, Y. A. and Associates, 1976. Aerosol in the GATE Area and Its Radiative Properties. Colorado State University Atmospheric Science Paper No. 247, Fort Collins, Colorado.

_____, R. M. Welch, and Associates, 1976. Comparison between the Measured and Calculated Spectral Characteristics of Shortwave Radiation in the Free Atmosphere over the Desert. Colorado State University Atmospheric Science Paper No. 261, Fort Collins, Colorado.

Liou, K and T. Sasamori, 1975. The Transfer of Solar Radiation in Aerosol Atmospheres. Journal of Atmospheric Sciences, 32, pp. 2166-2177.

Mani, A. and V. Srinivasan, 1972. Airborne Radiometer Measurements of the Effect of Clouds and Particulates on the Terrestial Radiation Flux. Proceedings International Radiation Symposium, Sendai, Japan.

Paltridge, G. W., and C. M. R. Platt, 1973. Absorption and Scatter of Radiation by an Aerosol Layer in the Free Atmosphere. Journal of Atmospheric Sciences, 30, pp. 734-737.

REFERENCES (Continued)

Paltridge, G. W., and C. M. R. Platt, 1976. Radiative Processes in Meteorology and Climatology. Developments in Atmospheric Science 5, Elsevier Scientific Publishing Co., Amsterdam, Oxford, New York.

Poellet, M. R., and S. K. Cox, 1975. Computer Simulation of Irradiance Measurements from Aircraft. Colorado State University Atmospheric Science Paper No. 233, Fort Collins, Colorado.

Prospero, J. M., R. T. Nees, and D. Savoie, 1976. Atmospheric Aerosol Measurements During GATE. University of Miami Technical Report TR76-5.

Reynolds, D. W., T. H. Vonder Haar, and S. K. Cox, 1975. The Effect of Solar Radiation Absorption in the Tropical Troposphere. Journal of Applied Meteorology, 14, pp. 433-444.

Robinson, N., 1966. Solar Radiation. Elsevier Publishing Co., Amsterdam, London, and New York.

Robinson, G. D., and A. J. Drummond, 1971. Some Recent Aircraft Measurements of the Absorption and Scattering of Solar Radiation by Atmospheric Aerosol. Proceedings, International Conference on Weather Modification, Canberra, Australia.

Rockwood, A. A., and S. K. Cox, 1976. Satellite Inferred Surface Albedo over Northwestern Africa. Colorado State University Atmospheric Science Paper No. 262, Fort Collins, Colorado.

Sellers, W. D., 1965. Physical Climatology. The University of Chicago Press, Chicago and London.

Stowe, L., 1974. Effects of Particulate Matter on the Radiance of Terrestial Infrared Radiation: RESULTS. Journal of Atmospheric Sciences, 31, pp. 755-767.

Vonder Haar, T. H. and S. K. Cox, 1972. Simultaneous Measurements of Solar Radiation from Aircraft and Satellites during BOMEX. Preprints Conf. Atmospheric Radiation, Fort Collins, Colorado, Amer. Meteor. Soc., pp. 128-133.

Welch, R. M. and W. Zdunkowski, 1976. A Radiation Model of the Polluted Atmospheric Boundary Layer. Journal of Atmospheric Sciences, 33, pp. 2170-2184.

Yamamoto, G., 1962. Direct Absorption of Solar Radiation by Atmospheric Water Vapor, Carbon Dioxide, and Molecular Oxygen. Journal of Atmospheric Sciences, 19, 182.

APPENDIX A

Sabreliner Flight Descriptions

A.1 Flight data

All descriptions in this section are derived from the notes taken by the airborne mission scientists (AMS) and from Cox and Kraus (1975), unless noted otherwise. Times, unless specifically mentioned, are given in GMT; start times correspond to the beginning of the first leg and end times denote the end of the final leg of the flight. The times are followed by the aircraft position and by the time in local solar time (LST) in parentheses. These data are used in the comparative calculations. Next, the name of the AMS is noted. Then down systems or those which did not produce reliable data are given.

Weather conditions for each flight are then described. A general description for each day is mentioned first. Then sky conditions as seen from each flight level (FL) are described. Those flight levels which were deleted from the analysis (Section 3) are indicated with an asterisk. The descriptions in parentheses are made by the author after examinations of the flight films and photographs. Flight patterns follow from terminology described in Section A.2.

Day 211, July 30, 1974

Mission Data: 12:42:15 - 14:03:48; 13.7°N, 20.72°W; (12:02:15 LST); B.A. Albrecht; IR readings are suspicious, I/C with Soviet IL-18.

Weather Conditions: 3/8 - 5/8 suppressed trade Cu at 1.6 - 2.4K', dust layers from 1.3 - 5.9K' and 6.2 - 18.4K'

FL ($x10^3$ft)

20 - clear above, very heavy dust layer and broken trade Cu below

10 - dust layer top 12-13K', low horiz. visibility (HV)

5 - broken Cu below, under dust layer; improved HV

3 - cloud tops at 2K' $\leq$ 30%; dust above

Pattern - box (used in intercomparison)

Day 212 (2), July 31, 1974

Mission Data: 13:51:34 - 15:41:30; 14.47°N, 18.82°W; (12:59:13 LST), B.A. Albrecht; INS down; IR readings suspicious.

Weather Conditions: Dust surface to 19K', heaviest 5 - 15K', difficult to observe clouds due to dust.

FL ($x10^3$ft)

30 - 90% light Ci above

16.5 - dust below, light Ci above

8 - in dust layer, patches of trd. Cu below $\sim$ 20%

5 - below dust layer, HV decreased, trd. Cu decreased

1.7 - at cloud base

.05* - (20% trd. Cu above, calm seas)

1.7* - NC

5* - relatively few Cu below, none above, in haze

8* - 10% Cu below, Ci patches above, clear directly above

16* - 10% Cu below, some Ci at start

30* - NC

Pattern - Serpentine; linear step ascent

Day 217, August 5, 1974

Mission Data: 12:24:10 - 13:36:11; 14.31°N, 19.56°W; (11:35:16 LST), B.A. Albrecht, IR system down

Weather Conditions: Calm seas, clear, little dust

FL ($x10^3$ft)

33 - clear above and below, patches of trd. Cu dust somewhat suppressed, (no dust visible)

16.5 - clear above and below, excellent vis., no dust

10 - clear above and below (Ci on horizon)

5,2,1* .065 - clear above and below excellent HV

Pattern - Serpentine

Day 229, August 17, 1974

Mission Data: Over land, 13:24:00 - 14:32:40; 14.77°N, 16.24°W; (12:37:43 LST); S.K. Cox; INS down

Over sea, 14:46:45 - 15:49:00; 15.43°N, 17.66°W; (13:43:07 LST); S.K. Cox; INS down

Weather Conditions: dust

FL ($x10^3$ft) Over Land

31 - some Ci overhead

21* - NC

17 - very near top of dust

15*, 13, 11*, 7 - NC

3.3* - at top of St. Cu deck, enter a few clouds

1 - pretty clear overhead

.05* - relatively clear overhead

Over Sea

17 - clearly on top of dust

15, 13* - NC

11 - .6 St. Cu below (after awhile)

9,7,5 - NC

3.6* - undercast with a few breaks, above clouds, below dust

.1* - clouds overhead, (calm seas)

Pattern - N-S racetrack

Day 237, August 25, 1974

Mission Data: 11:14:30 - 12:39:20; 14.95°N, 19.6°W; (10:50:50 LST); B.A. Albrecht; (IR↑ readings biased)

Weather Conditions: Suppressed convection; clear above, some Ci, no dust

FL ($x10^3$ft)

39 - light Ci above, clear later; no large amounts of dust

35* - (light Ci above, some trd., Cu below)

30* - some Ci above, few clouds below

25* - some Cu below, clear above

20* - some Ci above, mostly clear below

16 - clear above, some Cu below for awhile

12* - precipitating Ci above, clear below

8 - clear above, light Cu below, very clear, no dust

5* - some precipitating Ci above

2.5 - clear above and below

1* - few trd. Cu above

.05 - clear above

Pattern - E-W racetrack

Day 254, September 11, 1974

Mission Data: 11:35:00 - 13:20:00; 14.95°N, 18.86°W; (11:05:04 LST);
B.A. Albrecht, INS down

Weather Conditions: Suppressed convection, .1 trade Cu, light to moderate dust

Fl ($x10^3$ft)

35 - clear above, some trd. Cu below

25* - .1 trd. Cu below, clear above

19 - above dust, .1 trd. Cu below, clear above

17* - near top of dust layer, clear above, Cu below

15 - slightly below top of dust

13* - moderate to light dust

9 - broken Cu below with some dust

5 - clear and dust below

2.5 - some trd. Cu below

1 - some trd. Cu above

.05* - NC

1* - no clouds above, dust above seems confined to lower layers

2.5* - no clouds above

1* - number of Cu increasing significantly

Pattern - N-S racetrack

A.2 Flight patterns

Examples of the various patterns mentioned in A.1 are given in this section in Figures A1-A4. Possible effects on radiation

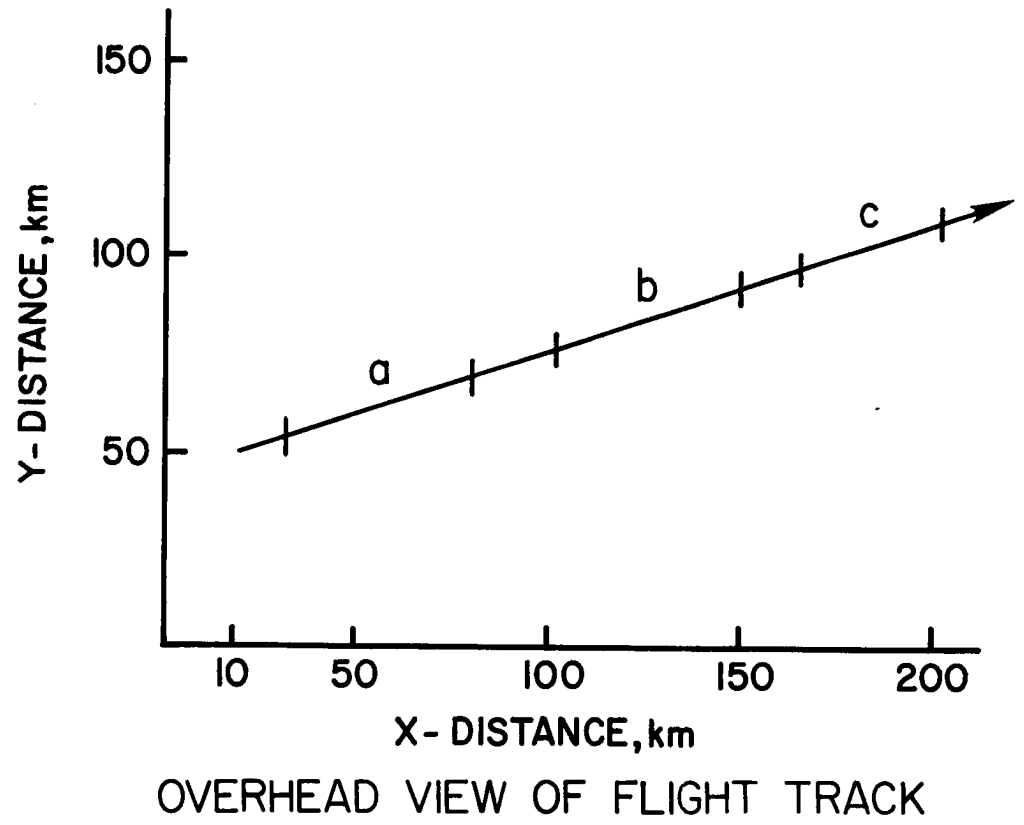

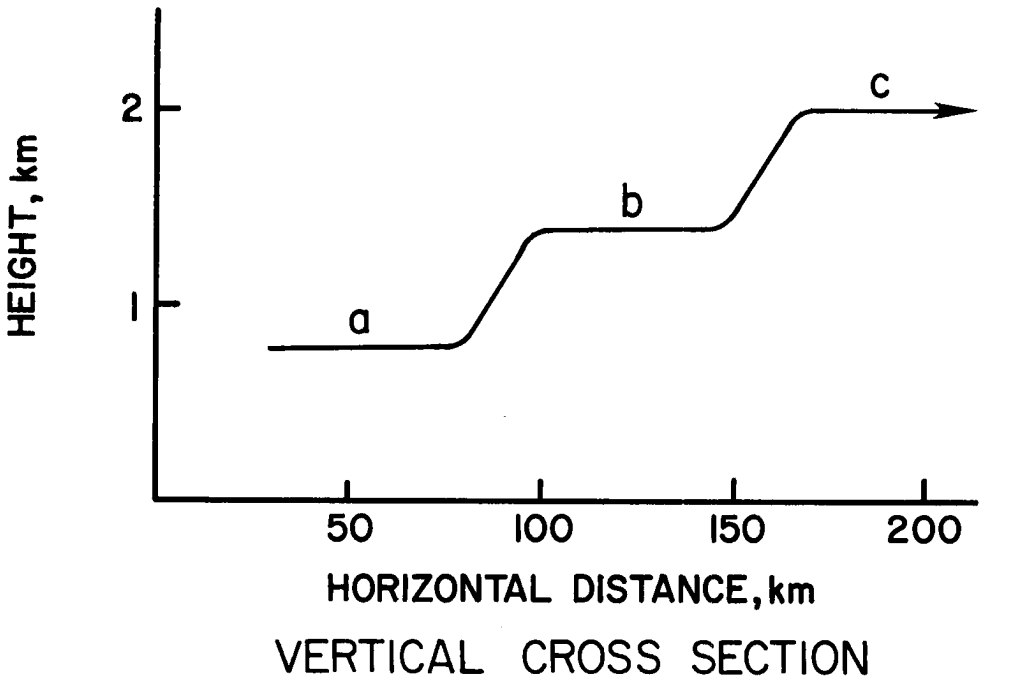

Figure A1. Schematic depiction of linear step ascent flight pattern.

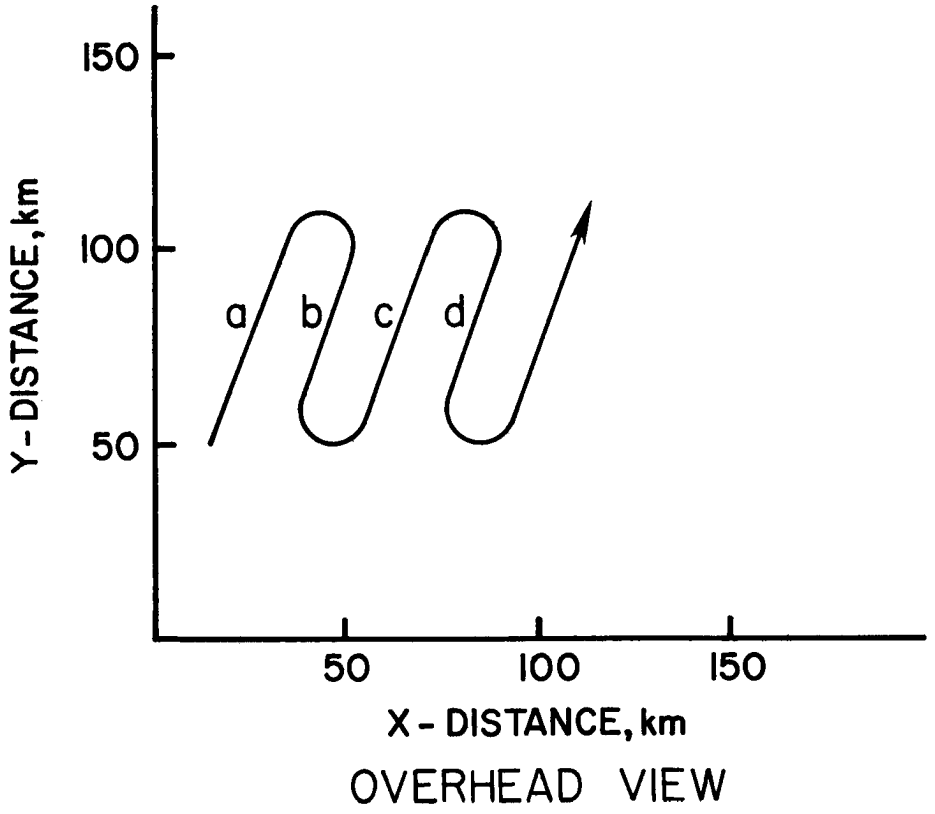

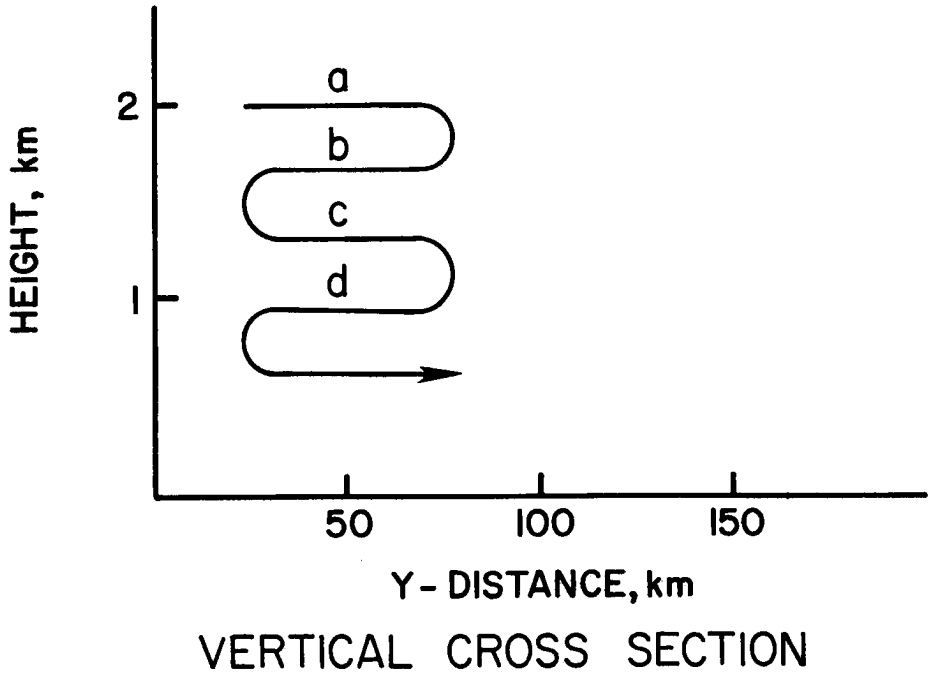

Figure A2. Schematic depiction of serpentine flight pattern.

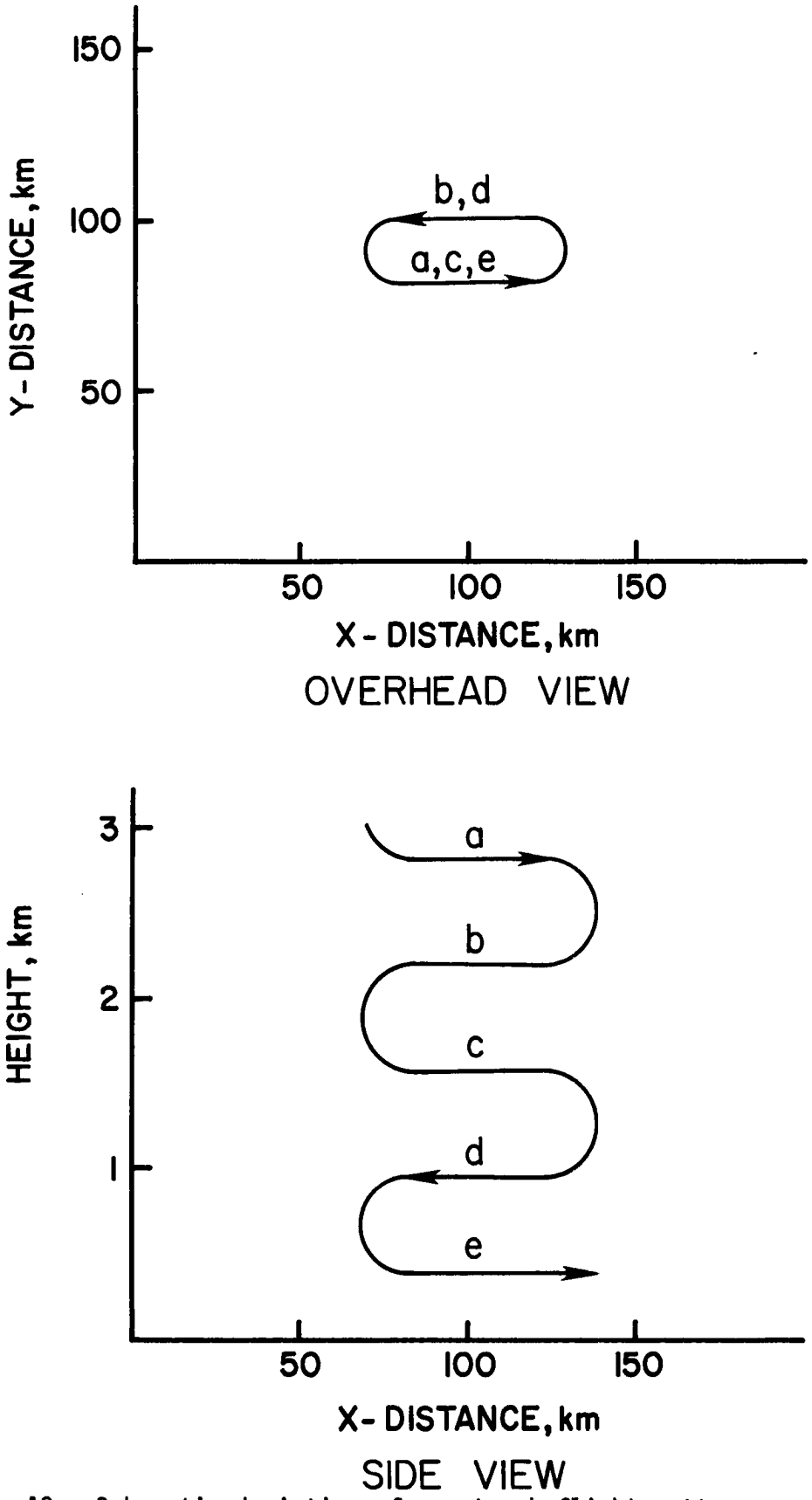

Figure A3. Schematic depiction of racetrack flight pattern.

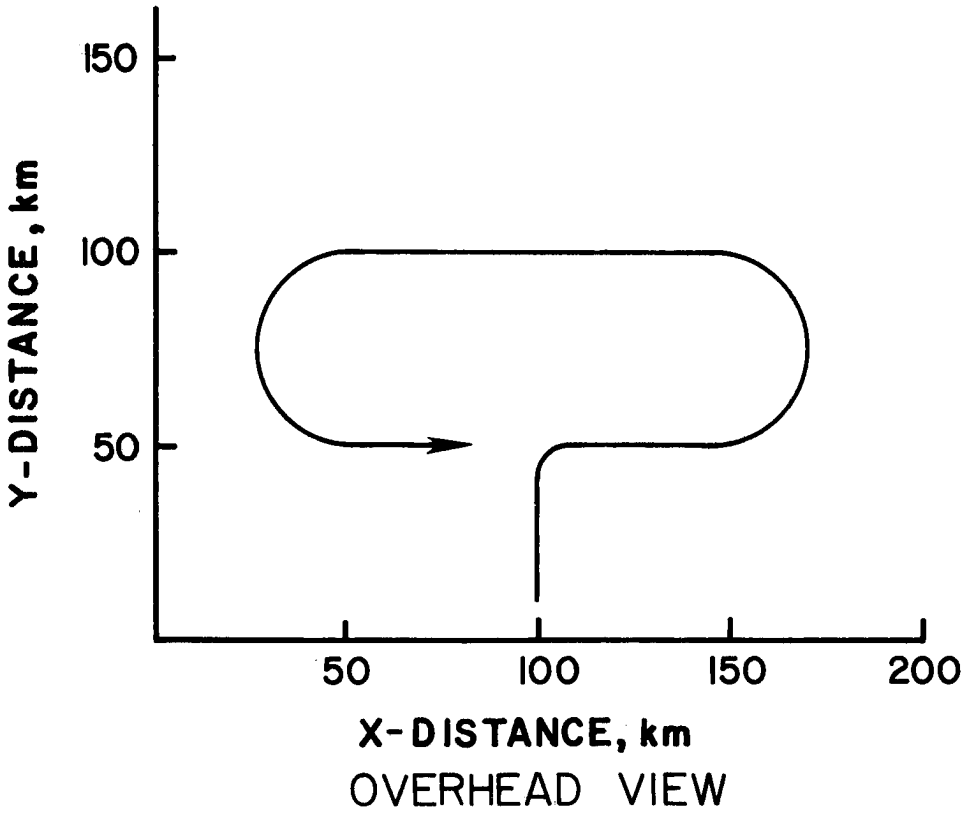

Figure A4. Schematic depiction of box flight pattern.

measurements due to the use of these patterns are noted in Section 3.4.1. Dimensions given in these figures are only approximate values. The letters refer to flight levels.

APPENDIX B

NOTES ON IRRADIANCE FIELDS VIEWED BY HEMISPHERIC SENSORS

Most of the equations and theory presented in this appendix have been adapted from Poellot and Cox (1975). The material discussed here is reported to acquaint the reader with some of the geometry involved in sensing with a small, hemispheric radiometer and the possible magnitude of some of the problems inherent in the attempt to screen out cloud effects from aircraft irradiance measurements. Only the case of a downward facing sensor viewing a shadow field is presented here but the same ideas may be applied to other types of sensing orientation and viewing fields. A complete treatment of this subject is reported in the reference noted above.

Poellot and Cox state "that the radiant power from an infinite plane uniform source passing through a hemisphere of unit radius at an angle θ is proportional to $\sin\theta \cos\theta \, d\theta$. The total power contributed at all angles from 0 to θ' is",

$$P \sim \int_0^{\theta'} \sin\theta \cos\theta \, d\theta \qquad (1)$$

where θ' is the angle taken from the normal to the flat plate of the hemispheric sensor, S_h. The field of view (f.o.v.) is 2π stereradians, which translates to a $\theta'_{max} = \pi/2$.

For a given θ' the fraction, p, of the power contained within the solid angle subtended between 0 and θ' from a given source is:

$$p = \frac{\int_0^{\theta'} \sin\theta \cos\theta \, d\theta}{\int_0^{\pi/2} \sin\theta \cos\theta \, d\theta} . \qquad (2)$$

For example, the 75% power field of view corresponds to a $\theta' = 60°$. It is shown in Poellot and Cox that the contribution to the irradiance at S_h from an area element dA is

$$\Delta H_s = \frac{\rho_A H_A \, dA \cos^2\theta}{\pi d^2} \qquad (3)$$

where ρ_A is the reflectivity of the given areal element dA, H_A is the incident irradiance at the reflecting areal element and d is the distance from S_h to the center for dA. This is depicted in Figure B.1.

Thus, for a non-uniform isotropic plane reflecting surface the power passing through the plane of the sensor for a f.o.v. described by θ' is area weighted by the function

$$w(r) = \frac{dA \cos^2\theta r}{\pi d_r^2} \qquad (4)$$

where r is the distance from the center of the f.o.v. as shown in Fig. B.1. Since

$$\theta' = \tan^{-1}\left(\frac{r}{h}\right) \qquad (5a)$$

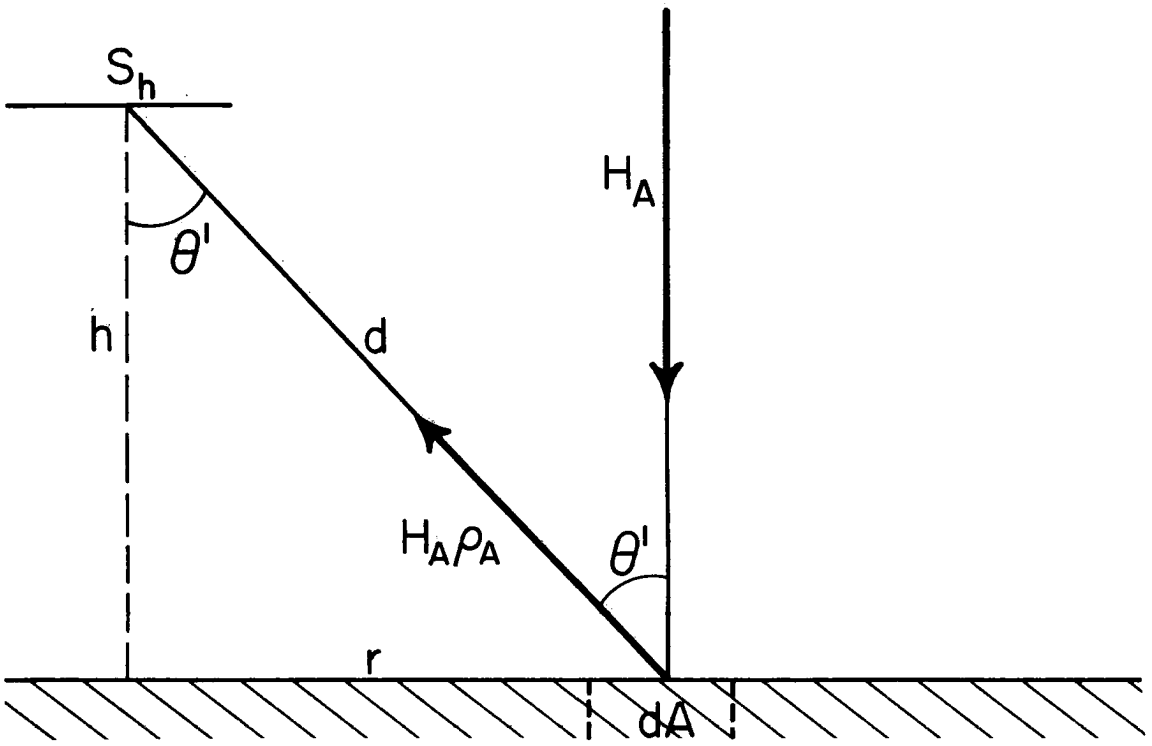

Figure B.1. Schematic representation of the geometry of the reflected irradiance field viewed by a downward-facing hemispheric sensor.

where h is the height of the sensor above the surface and the weight of a given area depends only on r and h. Referring to Fig. B.1 then, the total irradiance incident on the plate of the sensor, S_h, is

$$H_s = \sum_{r=0}^{r=r_{max}} \rho_A H_A * w(r). \qquad (6)$$

To illustrate this averaging effect of the sensor one may consider an extreme case depicted in Figure B.2. A downward facing shortwave sensor is on an aircraft located at 760 m at the center of large circular cloud. The instrument views a circular shadow on the smooth ocean, $\rho = .03$, which encompasses all angles of the f.o.v. out to 60° or the 75% power f.o.v. for a uniform source. The area outside this shadow is essentially clear, and 1000 Wm^{-2} reach the surface there. Under the cloud only 50 Wm^{-2} reach the surface. From equation (6) it is apparent that the sensor measures a total of $\sim$ 8.6 Wm^{-2}, or 7.5 Wm^{-2} from the clear area and 1.6 Wm^{-2} from the cloud shadowed region. So the minimum H↑ value for a clear area, 30 Wm^{-2}, is much higher than the observed. This corresponds to clouds with a horizontal diameter of about 2.6 km an idealized, extreme case for the sky conditions observed in this analysis.

As the sensor is moved farther away from the shadow center, of course, the expected clear sky minimum of 30 Wm^{-2} would be gradually approached. Also, when the cloud and/or the sensor are lowered the effect of diminishing H↑ would be enhanced. So the height of the cloud and sensor are as important as the size of the cloud.

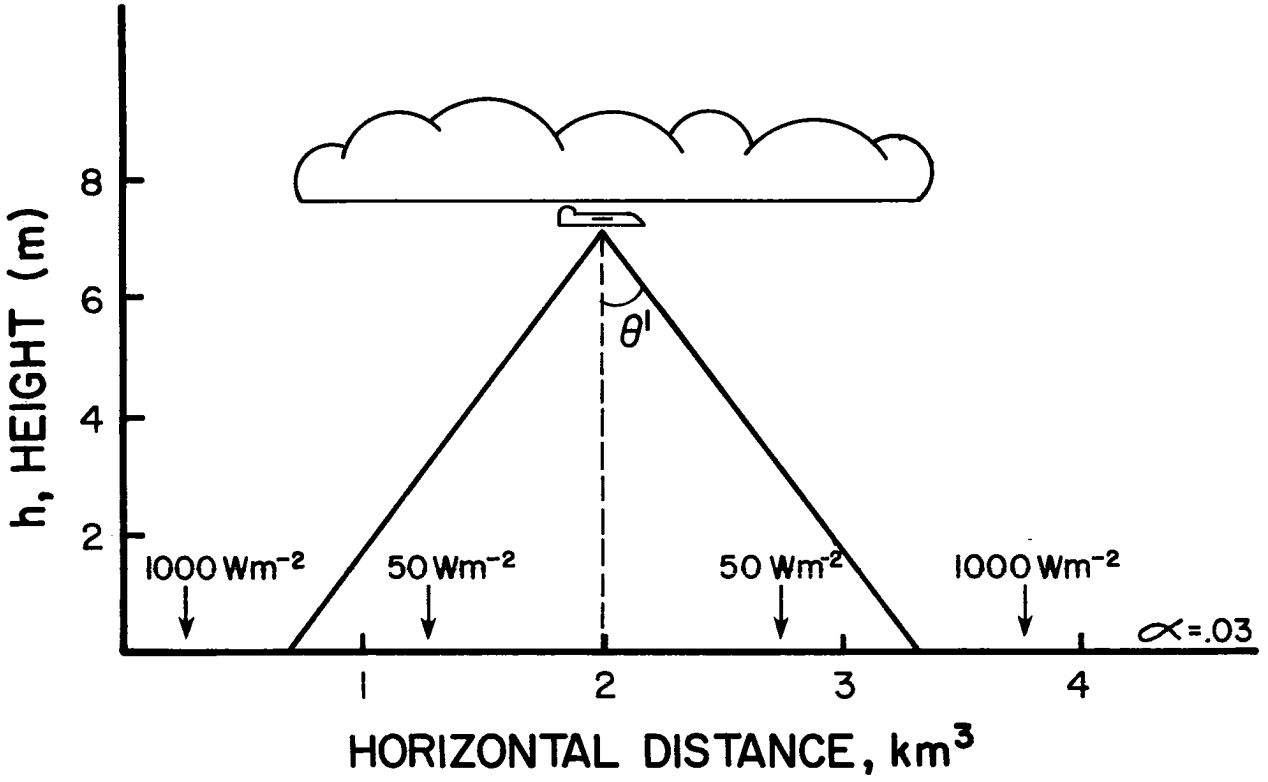

Figure B.2. Schematic representation of reflected irradiance field as viewed by an airborne hemispheric sensor under the center of a cloud.

A similar situation is realized in a broken cloud field when there are patches of shadow and clear in the field of view. The measured readings should all be lower than the expected minimum. The observed value for $H\uparrow$ will approach zero as sky conditions approach the overcast, black cloud situation. This same reasoning must also be applied to viewing cloud fields overhead ($H\uparrow$) and viewing cloud fields, as opposed to shadows, below.

The effect on albedo from the above situations can be quite anomalous. For example, consider an aircraft flying at cloud base in a partly cloudy situation. The $H\uparrow$ observation should be a reasonable average of the total reflected irradiance in the region, lower than the clear case but higher than the overcast. On the other hand, the $H\downarrow$ average, depending on the duration of the leg, could be representative of a clear area, a cloudy area or a reasonable combination of the two. If it is a clear area ρ would be too low; if cloud, ρ would be too high. So it is apparent that the data can sometimes be misleading.

APPENDIX C

Data Analysis Techniques

C.1 Geometry correction

After the initial selection of irradiance data it was necessary to apply a geometric correction factor to the measured $H\downarrow$ because the aircraft flew in a plane which was not parallel with the horizontal plane of the earth below (Rockwood and Cox, 1976). Since the pyranometer was mounted parallel to the longitudinal and lateral axes of the Sabreliner (Section 3.1) this corrective factor is a function of the aircraft true heading, roll and angle of attack and the sun-earth geometry. The correction procedure and the possible errors associated with its use are explored further in this section.

C.1.1 Corrective equation

The symbols used in Figure C.1 and in the derivation are explained here for future reference.

- p - pressure
- β - angle between the normal to a plane and the solar beam
- ϕ - geographical latitude
- t - hour angle of the sun (0° = 00 Local Solar Time)
- JD - Julian day number
- A_s - solar azimuth
- A_p - aircraft true heating or azimuth
- ς - tilt angle of plane to horizon
- AA - aircraft angle of attack
- R - aircraft roll angle
- H_{OB} - measured irradiance on the plane of the pyranometer

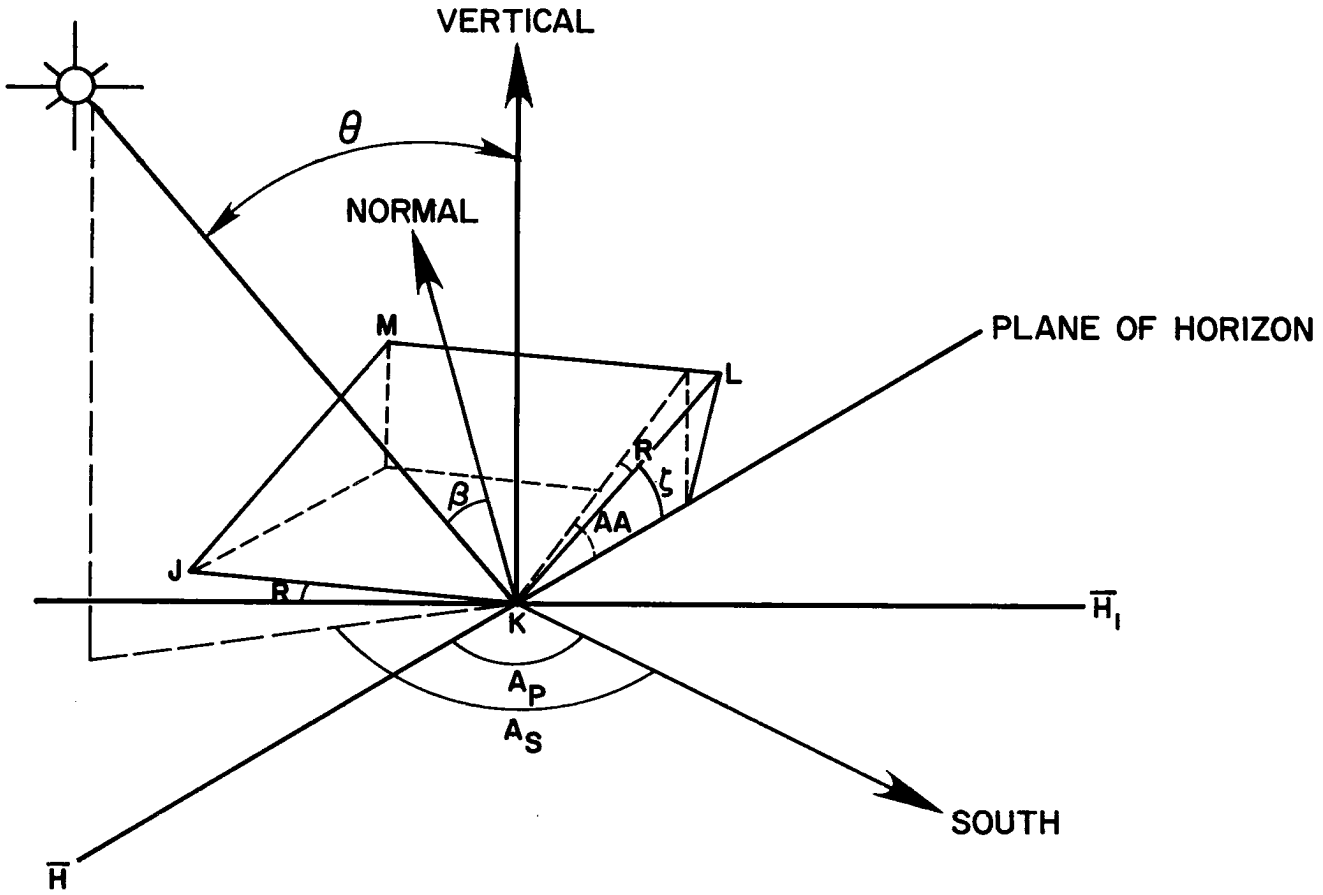

Figure C.1. Diagram of the angles and planes used in the correction of the solar irradiance on a tilted plane. (An adaptation from Sellers, 1965).

H_{TR} - actual irradiance on a horizontal plane

H_{DR} - irradiance on a plane perpendicular to the direct solar beam

H_{DF} - diffuse irradiance

x - direct to total ratio

δ - $23.5 \cos \left[\frac{360}{365} (JD + 10)\right]$ = solar declination. (1)

Now consider an upward facing pyranometer on a plane parallel with JKLM in Figure C.1. When there is no diffuse radiation

$$H_{OB} = H_{DR} \cos \beta. \tag{2}$$

However, when diffuse radiation is present

$$H_{OB} = H_{DF} + H_{DR} \cos \beta \tag{3}$$

where β is related to the other angles in Figure C.1 by

$$\cos \beta = \cos \zeta + \sin \zeta \cos \theta \cos (A_s - A_p) \tag{4}$$

as given by Robinson (1966) and where

$$\cos \theta = \sin \phi \sin \delta - \cos \phi \cos \delta \cos t. \tag{5}$$

Setting

$$\cos A_s = \frac{\sin \phi \cos \theta - \sin \delta}{\cos \phi \sin \theta} \quad \text{(Sellers, 1965)} \qquad (6)$$

and expanding (4) according to Robinson (1966) and using the angles in Figure C.1,

$$\cos \beta = \cos AA \cos R \cos \theta + \sin AA \{\cos A_p \qquad (7)$$

$$[\tan \phi \cos \theta - \sin \delta \sec \phi] + \sin A_p$$

$$\cos \delta \sin t\} + \cos AA \sin R \{\cos \delta \sin t$$

$$\cos A_p + \sin A_p [\cos \theta \tan \phi - \sin \delta \sec \phi]\}.$$

For radiation incident on a horizontal plane, H_{TR}, a correction of the direct component must be made for the solar zenith angle as follows:

$$H_{TR} = H_{DF} + H_{DR} \cos \theta. \qquad (8)$$

For a direct to total ratio, x,

$$x = \frac{H_{DR}}{H_{TR}} \text{ or} \qquad (9a)$$

$$H_{DR} = x\, H_{TR}. \tag{9b}$$

Substituting (9b) into (8) and rearranging gives

$$H_{DF} = H_{TR} - H_{TR}\, x \cos\theta\ . \tag{10}$$

Now H_{OB} may be converted to H_{TR} by returning to (3) and substituting (9b) and (10) to yield

$$H_{OB} = H_{TR}\,[1 - x\,(\cos\theta + \cos\beta)]. \tag{11}$$

Rearranging (11) results in the final corrective equation

$$H_{TR} = \frac{H_{OB}}{[1 - x\,(\cos\theta + \cos\beta)]}\ . \tag{12}$$

C.1.2 Estimation of ratio of direct to total shortwave irradiance

In order to use equation 12 it is necessary to estimate the size of the direct component, H_{DR}, or the direct to total ratio, x. Values of x at the surface are given in Rockwood and Cox (1976). These were derived from measurements by Carlson (1975) and calculations from Robinson (1966) for turbid atmospheres. Up to this time measurements of H_{DF} or H_{DR} have not been taken except at the surface. However, calculations

may be made to estimate H_{DF} due to Rayleigh scattering (H_{DFR}) so that clear case values of x may be approximated.

To estimate H_{DFR}, equations adapted from Paltridge and Platt (1976) are applied to data from day 237. These relationships are given below.

$$H_{DFR} = (H_T - H_{OB}) \cos \theta - H_T \cos \theta \, \alpha_R (\theta), \tag{13}$$

where

$$\alpha_R (\theta) = \frac{0.28}{(1 + 6.43 \cos \theta)}. \tag{14}$$

When the surface albedo is taken into account

$$H_{DFT} = H_{DFR} + (H_{DFR} + H_{OB} \cos \theta) \quad .0685 \, \alpha, \tag{15}$$

where H_{DFT} is the total Rayleigh scattered downward flux. Utilizing H↓ data from day 237 (clear) in equations 13-15 the points shown in Figure C.2 were derived. From 550 mb to 1012 mb x versus pressure appears to be a linear relationship. For simplicity it was assumed that a linear dependence of x on p also exists between 240 and 550 mb. These two lines, ED and DC, are assumed to be representative of the clear case.

For dusty conditions it was assumed that line ED still represents x versus p above 550 mb. Below that level the linear dependence was still assumed to hold but with a new slope determined by a measured value of x at the surface. This was taken as .52, a conservative value

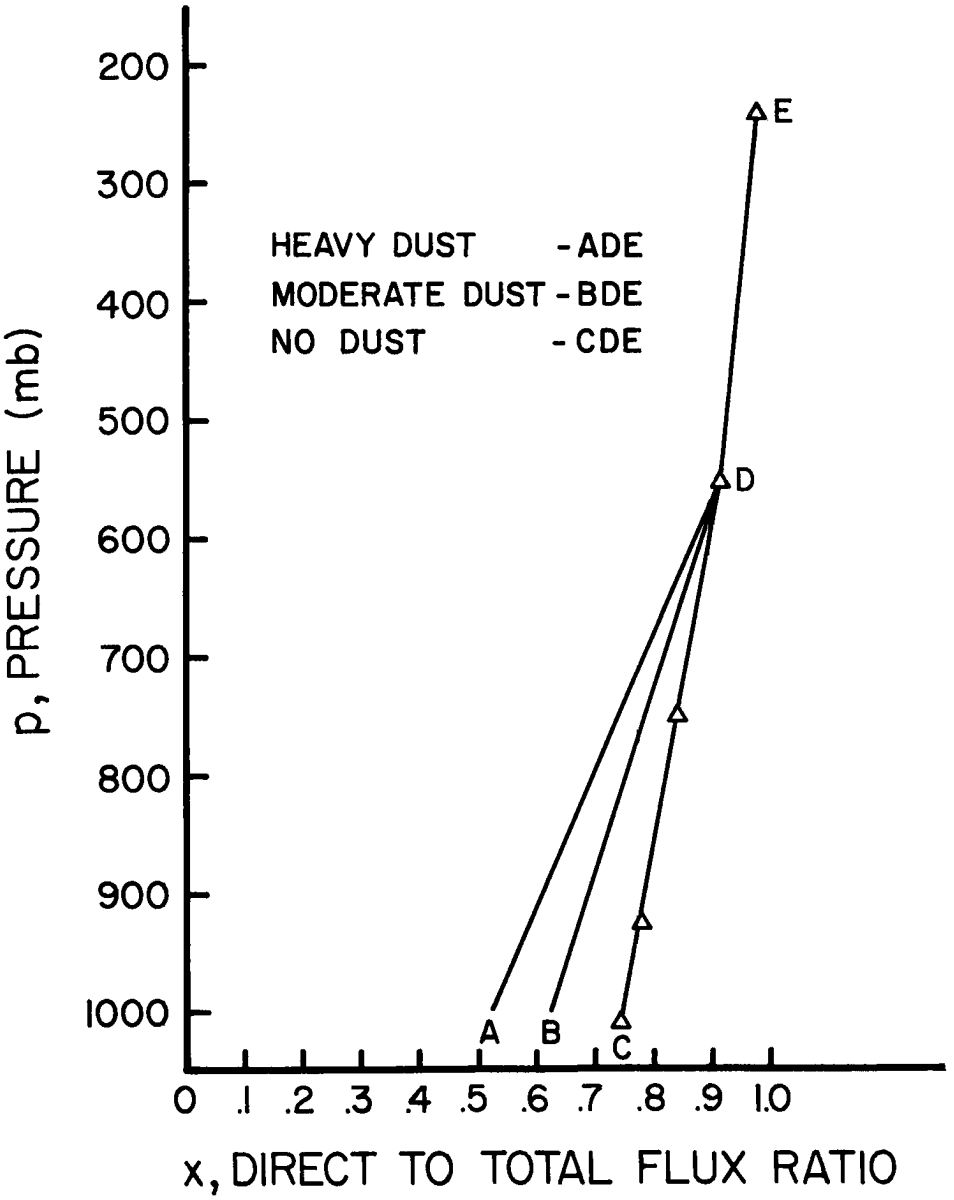

Figure C.2. Direct to total flux ratio as a function of pressure and dust classification.

which was found at local noon under suppressed visibility conditions (Rockwood and Cox, 1976). So in Figure C.2 line DA represents a dusty atmosphere below 550 mb.

To further simplify the estimation of x it was assumed that the midpoint, B , between A and C represented the surface value under light or moderately dusty conditions. Although x is a function of the solar zenith angle this dependence is neglected here since all readings used were taken within 2 hours of local noon and because no actual values of x for these flights are known. And as is shown in the following section, a rough estimate is all that is required for the purposes of this study.

C.1.3 Sensitivity of H_{TR} to x and R

With the simple estimation scheme described above it is obvious that some error will be introduced into the calculation of H_{TR}. Thus, it is necessary to determine how sensitive H_{TR} may be to an error in x. By using varying values of x in the correction of the same H_{OB} data it should be possible to ascertain the response of H_{TR} to a change in x, Δx.

Employing data from a moderately dusty day and Δx values as high as .3, it was found that H_{TR} is not strongly affected by errors in x. At $\Delta x = .3$, H_{TR} was only of the order of .5% or 6 Wm^{-2} in 1150 Wm^{-2}. Using a more reasonable error of $\Delta x = .2$, the maximum ΔH_{TR} found was 4 Wm^{-2}. But generally the value of ΔH_{TR} at $\Delta x = .2$ was only between .5 $Wm^{-2}$and 1.5 Wm^{-2}. Therefore, it appears that the estimation technique used is reasonable for the purposes of this study.

Occasionally the INS system failed to function so that roll data were unavailable on a number of days. Thus, it is also important to

know the sensitivity of H_{TR} to errors in R. Using the H_{OB} data H_{TR} was calculated at each flight level using R values of 0, 4, and 8° as well as the actual roll averages derived from the INS data.

The results of these tests are shown in Table CI where it may be seen that $H_{TR_{max}} \simeq 2.7\ Wm^{-2}$ at a $\Delta R \simeq 3°$. However, at $\Delta R \simeq 1.2°$, $\Delta H_{TR_{max}} = .6\ Wm^{-2}$. Since no average roll values exceeded $\pm$ 1.5° during any flight considered, it was assumed that the effect of setting R = 0° in equation 7 was negligible.

R FL° (mb)	0° ΔR (°)	0° ΔH_{TR} (Wm^{-2})	0° $\%H_{OB}$	4° ΔR (°)	4° ΔH_{TR} (Wm^{-2})	4° $\%H_{OB}$	8° ΔR (°)	8° ΔH_{TR} (Wm^{-2})	8° $\%H_{OB}$
318.5	-1.22	.6	.05	2.78	2.7	.2	6.78	9.5	.8
575.3	-.92	.03	.003	3.08	1.2	.1	7.08	5.8	.6
700.5	0.0	0	0	4.0	1.9	.2	8.0	7.1	.7
846.4	-.65	.11	.01	3.35	2.0	.2	7.35	7.4	.7
945.8	-1.18	.02	.002	2.82	1.1	.1	6.82	5.6	.6
981.7	-1.06	.32	.03	2.94	2.1	.2	6.94	7.9	.8
1012.5	-1.09	.53	.05	2.91	2.6	.3	6.91	9.1	.9

Table CI. The change in H_{TR} versus the change in roll (R) with respect to the INS measured values of R.

C.2 Adjustment and analysis of shortwave data

Because of the changing solar zenith angle between flight legs it is necessary to normalize data from one flight level to the time of the next, in order to calculate accurate heating rates and layer absorptivities. The simplest technique is one which accounts for and minimizes

the change in the sun angle. This method, adapted from Cox (1975), is described below.

C.2.1. Level to level normalization

On a horizontal plane at a given level the incident intensity, $H\downarrow_1$, of a solar flux, $H\downarrow_0$, at time t_1, and solar zenith angle, θ_1, is

$$H\downarrow_1 = H\downarrow_0 \cos \theta_1 \quad \text{(Robinson, 1966).} \tag{16}$$

Similarly, at time t_2 on the same plane the incident flux, $H\downarrow_2$, is

$$H\downarrow_2 = H\downarrow_0 \cos \theta_2. \tag{17}$$

Dividing (16) by (17) and rearranging yields

$$H\downarrow_1 = H\downarrow_2 \frac{\cos \theta_1}{\cos \theta_2}. \tag{18}$$

Assuming a reflectivity at that level, ρ_L,

$$\rho_L = \frac{H\uparrow_1}{H\downarrow_1} \tag{19}$$

which is constant in time for the same plane,

$$\frac{H\uparrow_1}{H\downarrow_1} = \frac{H\uparrow_2}{H\downarrow_2}, \tag{20}$$

where $H\uparrow_1$ and $H\uparrow_2$ refer to the upward fluxes at t_1 and t_2 respectively. Substituting (18) for $H\downarrow_1$ and solving for $H\uparrow_1$ results in

$$H\uparrow_1 = H\uparrow_2 \frac{\cos \theta_1}{\cos \theta_2}. \tag{21}$$

However, since the reflectivity at an atmospheric level or at the surface may be a function of the zenith angle and because the solar flux, $H\downarrow_0$, consists of both a direct and diffuse component it is essential that the difference between θ_1 and θ_2 is as small as possible. For a set of averaged data with more than two levels and times this minimization may be accomplished by correcting the data for each level to the average time of the previous level and then calculating the radiative parameter for the layer.

Consider $\overline{H}\downarrow_i$ and $\overline{H}\uparrow_i$ data at n flight levels, where $\overline{H}\downarrow_i = \overline{H}\downarrow_{TRi}$, and where the bar indicates the average value over the time interval at level i. Utilizing equations 18 and 20 normalized flux values $\overline{H}\downarrow'_{i+1}$ and $\overline{H}\uparrow'_{i+1}$ may be generated as follows:

$$\overline{H}\downarrow'_{i+1} = \overline{H}\downarrow_{i+1} \frac{\cos \overline{\theta}_i}{\cos \overline{\theta}_{i+1}}, \quad i = 1, n \tag{22}$$

and

$$\overline{H}\uparrow'_{i+1} = \overline{H}\uparrow_{i+1} \frac{\cos \overline{\theta}_i}{\cos \overline{\theta}_{i+1}}, \quad i = 1, n. \tag{23}$$

The fractional absorption, for a layer between pressure levels i and i+1 is defined as

$$F_{a_{i,i+1}} = \frac{\bar{H}_{NET_i} - \bar{H}'_{NET_{i+1}}}{H\downarrow_T} , \quad i = 1, n. \tag{24}$$

For the same atmospheric layers the average instantaneous heating rates due to the absorbed radiation, $\Delta\bar{H}$, are

$$\left(\frac{\overline{\Delta T}}{\Delta t}\right)_{i,i+1} = - \frac{g}{cp} \frac{\Delta H_{i,i+1}}{\Delta_{p_{i,i+1}}} , \tag{25}$$

where $$\Delta\bar{H}_{i,i+1} = \bar{H}_{NET_i} - \bar{H}'_{NET_{i+1}}, \tag{26}$$

and level i is above level i+1.

C.2.2 Single time normalization

Although the correction procedure outlined above is assumed to be relatively accurate, a data set corresponding to a single time is required if a direct comparison to the model results is to be made. This type of data set may be derived by normalizing the shortwave fluxes for all of the flight legs to a single reference zenith angle.

To minimize errors arising from a changing sun angle the solar zenith angle, θ_R, from the approximate middle leg of the flight was

chosen as the reference angle. The averaged data from the remainder of the flight were then adjusted to this angle using variant forms of (22) and (23) as follows:

$$\overline{H\downarrow}_i^R = \overline{H\downarrow}_i \frac{\cos \overline{\theta}_R}{\cos \overline{\theta}_i}, \quad i = 1, n; \tag{27}$$

and

$$\overline{H\uparrow}_i^R = \overline{H\uparrow}_i \frac{\cos \overline{\theta}_R}{\cos \overline{\theta}_i}, \quad i = 1, n. \tag{28}$$

To determine how valid this type of normalization may be for this analysis a comparison between the procedures from this section and C.2.1 is performed. Values for F_a and $\frac{\Delta T}{\Delta t}$ are calculated for each layer in the worst case, i.e. the flight with the largest difference in $\overline{\theta}$ for the first and last legs used in this study. This was found to be day 237 with $\Delta\overline{\theta}_{1,n} = 17.2°$. The results of both methods for this day are listed in Table CII. The reference level is 754.4 mb with a zenith angle, $\overline{\theta}_R = 17.51°$.

It is obvious that there is little difference in the two techniques especially for absorptivity values. The differences in heating found from the two methods are also negligible. For layer 1 a heating rate difference of .004°C hr^{-1} is actually insignificant although it is a relative error of approximately 8%. Since an approximate visual comparison of heating rates, as mentioned in 4.1.3, is all that is desired here, this type of normalization should suffice.

FL(mb) / Layer #	$F_{a_{LL}}$ (%)	$(\Delta T/\Delta t)_{LL}$ (°C hr^{-1})	$F_{a_{SL}}$ (%)	$(\Delta T/\Delta t)_{SL}$ (°C hr^{-1})	ΔF_a (%)	$\Delta(\Delta T/\Delta t)_{LL,SL}$ (°C hr^{-1})
238.7						
1	.0337	.046	.0337	.050	0	.004
550.1						
2	.0282	.062	.0282	.063	0	.001
754.4						
3	.0401	.106	.0401	.106	0	0.0
927.3						
4	.0133	.075	.0133	.074	0	.001
1010.7						

Table CII. Fractional absorption and heating rate values for day 237 using the level to level (LL) and single level (SL) normalization methods.

C.3 Measurement and correction errors

In order to determine how significant an effect attributed to the dust may be, it is essential to establish the magnitude of the errors which may be introduced into the data. There are four main sources for possible error in the collection and analysis of the flux data and these are investigated below.

Measurement system errors are generally eliminated or minimized with the data reduction and correction procedures mentioned in 3.1, although no improvement may be made on the absolute resolution of the system of $\pm$ 2 Wm^{-2}. There also may be some bias in the flux measurements which may result in an absolute error of several watts per square meter. However, it is assumed that this offset is constant for a given flight and all readings from an instrument are affected uniformly. Since the parameters of interest are derived from differences in the fluxes any effect due to an instrument offset is non-existent or negligible.

Inaccurate specification of input parameters for the geometric correction for $H\downarrow$ may also lead to some errors in the true value, H_{TR}, of the downward shortwave flux. The effects of inaccuracies in two of these parameters, aircraft roll angle and the ratio of direct to total irradiance, have been discussed in section C.1.3. Some error may also result from incorrect values of the aircraft angle of attack. These will be of the same order as the errors in the roll angle, $\leq$ 1 Wm^{-2} for an error of approximately one degree. Other variables such as time, latitude, and zenith angle are assumed to be correct. Since the corrective factor is such a small number, slight errors in these parameters would have only negligible effect anyway.

The sources for the largest possible errors arise from the use of the cloud screening technique and the linear interpolation between measurements. In order to filter inhomogeneities in sky conditions it was necessary at times to apply subjective judgements during the selection of limiting criteria. Although the method tends to smooth the data considerably and to reduce the standard deviation from the mean, its use still depends on some degree of subjectivity. Therefore, it becomes difficult to assess the size of the possible error in an absolute sense.

Although the linear approximation for H↓ and H↑ appears to be valid for clear cases (see Chapter 5) below 550 mb, it does not necessarily hold true for dusty conditions. However, for a layer such as the SDL the interpolated flux values should be quite close to the actual values, neglecting other errors, at 550 and 950 mb since observations were taken within 50 mb of these levels on most flights.

To obtain an estimate of the size of the effects of the two uncertainties mentioned above, it was decided to perturb the solar flux measurements with normally distributed random numbers having a standard deviation equal to the value of the typically largest standard deviation for each case. For H↓ this value generally remained less than 5.2 Wm^{-2}, while the largest standard deviation for H↑ was less than 2.5 Wm^{-2} for most cases. These values were then added to the measured fluxes which in turn were plotted with respect to pressure. Values for H↓ and H↑ at both 550 and 950 mb were determined and the radiative parameters were calculated. These numbers were then subtracted from the initial parameters to obtain the size of the possible errors.

The results of this procedure for day 229L are given in Table CIII. From these ten trials it may be seen that the random errors in flux

Trial	ΔF_a	% F_a	ΔF_r	% F_r
1	-.0022	2.5	.0013	2.2
2	-.0043	5.0	.0004	0.6
3	+.0011	1.3	-.0030	5.3
4	-.0031	3.6	.0010	1.6
5	-.0019	2.3	.0010	1.6
6	.0047	5.5	-.0011	1.8
7	.0009	1.1	-.0014	2.2
8	-.0051	5.9	.0005	0.9
9	.0084	9.7	-.0033	5.4
10	.0050	5.8	-.0016	2.6
Avg.	$\pm$.0037	4.3	$\pm$.0015	1.6

Table CIII. Differences in fractional absorption and fractional reflection in the 550 - 950 mb layer due to random errors in measured shortwave flux values.

measurements based on the standard deviation yield uncertainties in the fractional absorption which rarely exceed 6% or .005. The average of $\pm$ .004 may be more representative. These same perturbations have even less effect on the reflectivity values as would be expected from the smaller standard deviation in the upward direction.

Determination of the errors in heating rates due to these random perturbations is not as straightforward. Since the heating rates are inversely proportional to the difference in pressure between two given levels, the size of the heating rate error depends not only on the uncertainties in flux measurements, but also on the magnitude of the pressure differential, Δp. As Δp increases the size of the error in heating rates decreases because the irradiance errors are spread over a larger pressure interval. Conversely as Δp decreases the accuracy of the flux measurements becomes more critical. A slight error in ΔH may result in a significant error in $\frac{\Delta T}{\Delta \tau}$ for this case. The dependence of the heating rate on Δp is illustrated in Figure C.3 for several values of errors in ΔH.

Because of the reliance on Δp, heating rate errors must be estimated individually for each case. However, the heating rate errors calculated from the perturbed fluxes may be averaged for each layer. These layer averages are weighted according to pressure thickness and averaged to yield an estimate of the expected error. For the perturbed shortwave data the average heating rate error for a 139 mb layer is .012°C hr^{-1} which corresponds to an error in ΔH of 4 Wm^{-2}.

Parameters were also determined for concurrent errors to simulate a worst case situation. At a maximum error of approximately 25 Wm^{-2} ΔH_{NET} between the lowest and highest levels, a change of nearly 21% in

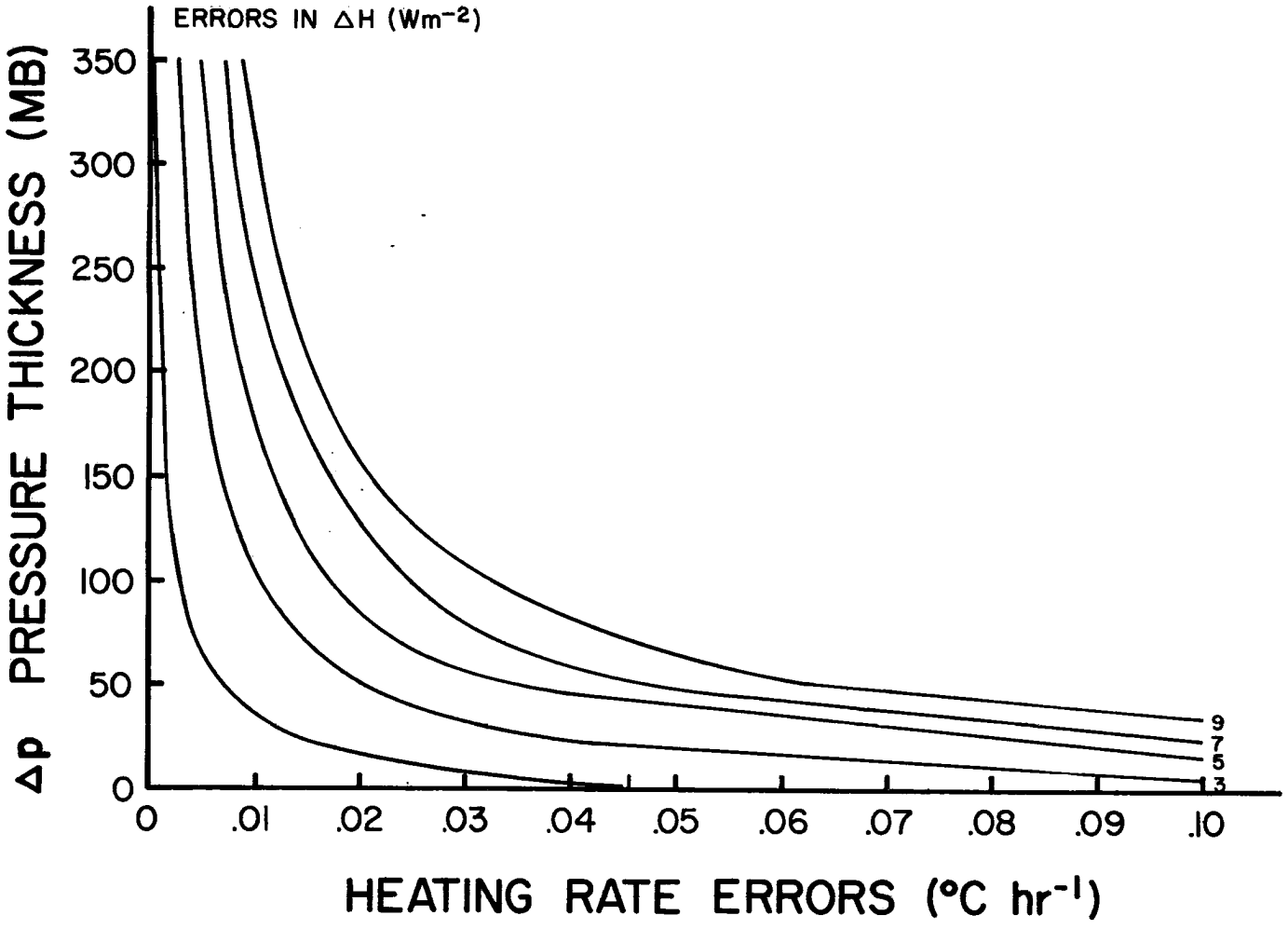

Figure C.3. Errors in layer heating rates as a function of the layer pressure thickness, Δp, and the errors in absorbed irradiance, ΔH.

fractional absorption for the 550 - 950 mb layer was found. Similarly for a 9 Wm^{-2} change in $\Delta H\uparrow$ a difference of 11% was found for the layer reflectivity. The sizes of the above errors, though not unreasonable, are unlikely for most of the measurements because the standard deviations were usually much smaller than those used in these computations. Error estimates of .005 and .002 in absorptivity and reflectivity respectively would be more probable for most of the measurements.

BIBLIOGRAPHIC DATA SHEET	1. Report No. CSU ATSP-283	2.	3. Recipient's Accession No.

4. Title and Subtitle
Magnitude of the radiative effects of the Saharan dust layer

5. Report Date
January 1978

6.

7. Author(s)
Patrick Minnis and Stepheh K. Cox

8. Performing Organization Rept. No. CSU ATSP-283

9. Performing Organization Name and Address
Department of Atmospheric Science
Colorado State University
Fort Collins
Colorado 80523

10. Project/Task/Work Unit No.

11. Contract/Grant No.
OCD 74-21678
ATM 77-15369

12. Sponsoring Organization Name and Address
National Science Foundation
1800 G Street
Washington D.C.

GATE Project Office
NOAA
Rockville
Maryland

13. Type of Report & Period Covered
M.S. Thesis

14.

15. Supplementary Notes

16. Abstracts The shortwave and longwave properties of the Saharan dust layer are studied using broadband hemispheric irradiance data and numerical radiative transfer routines. The analyzed data were collected during the GARP Atlantic Tropical Experiment (GATE) in the summer of 1974. The solar heating rates, fractional absorptions and reflectivities, as well as the longwave effective emissivities and cooling rates for the 550-950 mb layer are determined for both clear and dusty days. These parameters are compared to corresponding parameters derived with the aid of two broadband radiative transfer routines which utilize the observed temperature and moisture data. The magnitude of the dust effects are determined by differencing the measured and computed results.

It is found that the Saharan dust increases the atmospheric reflectivity in the area on the average by nearly 50% over the clear sky values. The increase in absorption, though only 9% for the average of six days may approach 20% of the total absorption for a clear atmosphere. The energy reflected by the dust is approximately twice the amount absorbed. Total extinction increases of up to 20% or 61 Wm^{-2} are found in the presence of dust. Observed heating rates are consistently higher in the dust layer than is calculated but by no more than 0.1°C hr^{-1}.

The infrared effects of the dust appear to be much less significant than the effects on the solar spectrum. Changes in effective emissivities in the presence of dust are ambiguous and rarely exceed the uncertainties of the observations. Cooling rate comparisons reveal the same type of inconsistencies.

17. Key Words and Document Analysis. 17a. Descriptors

GATE
Saharan Dust
Radiative Effects of Dust

17b. Identifiers/Open-Ended Terms

17c. COSATI Field/Group

18. Availability Statement	19. Security Class (This Report) UNCLASSIFIED	21. No. of Pages 111
	20. Security Class (This Page)	22. Price